MALAYSIAN JOURNAL OF SCIENCE

Vol. 42 ● No 2 ● June 2023

JURNAL SAINS MALAYSIA

ISSN 1394 - 3065

The Malaysian Journal of Science is indexed or cited in the following Scientific Databases: Elsevier Bibliographic Databases (ACI, Scopus, EMBASE, Compendex, GEOBASE, EMBiology, Elsevier BIOBASE, FLUIDEX and World Textiles); CAB Abstracts and Chemical Abstracts Service Database

http://www.myjurnal.my/public/browse-journal-view.php?id=194
www.mjs.um.edu.my

MALAYSIAN JOURNAL OF SCIENCE
MJS
ISSN 1394-3065

Regular Issue

Malaysian Journal of Science 42 (2): 1-6 (June 2023) https://mjs.um.edu.my

DETERMINATION OF URANIUM CONCENTRATIONS IN RICE SAMPLES AVAILABLE IN THE IRAQI MARKET USING THE CR-39 DETECTOR

Auday Tariq Al-Bayati[1a]*, Adawiya Mohsin Alwan[2b] and Hussein A. Miran[3c]

Abstract: In this study, uranium concentrations and specific activity in 10 rice samples were measured using a solid-state track detector (CR-39). Samples were collected from various local Iraqi markets with different origins (Iraq, India, USA, and Thailand). Our findings showed that the uranium concentrations in all studied samples ranged from 0.55 ± 0.28 to 1.74 ± 0.31 ppm, with a weighted average of 1.24 ± 0.99 ppm. In addition, the results demonstrated that the specific activity values of the studied samples were in the range 6.88 ± 3.52 and 21.49 ± 3.85 Bq/kg. The obtained results of the studied rice samples indicated that they are less than the acceptable limit established by many organizations such as the United Nations Scientific Committee on the Effects of Atomic Radiation (UNSCEAR), International Atomic Energy Agency (IAEA), and World Health Organization.

Keywords: *Uranium, specific activity, track density, rice, CR-39*

1. Introduction

Understanding the distribution of radionuclides and their radiation percentages in the environment is crucial in evaluating the impact of radiation levels caused by natural and synthetic sources. Naturally occurring radiation comes from radioactive nuclides that exist in diverse contents in sediments, waters, and rocks. Almost all rocks contain naturally occurring radionuclides such as ^{238}U, ^{232}Th, and ^{40}K. Some of the radionuclides from these sources are ingested with food and water or are inhaled by humans. However, the health effects on humans mainly depend on the level of these radionuclides present in rocks and sediments (Al-Bayati, 2013; El-Arabi, Abbady, & Hussein, 2006).

Quantitative analysis of radioactive pollution in the atmosphere and in food products is crucial in controlling and minimizing its harmful effects on human health. In addition to natural radionuclides, reactor-made radionuclides are introduced to the atmosphere by nuclear weapon testing and numerous nuclear reactor accidents. Worldwide, consuming irradiated products from any area contaminated by nuclear radiation can affect people's health (Melquiades & Appoloni, 2002).

The effects of internal radiation exposure can be controlled by assessing several factors. The first factor relates to the slow development and the emergence of the radiation effect. The second factor is the relation between the absorbed radiation doses into the tissue and the required time for the radioactive material to decay, leading to the accumulation of radiation. The third factor highlights the levels of chemical toxicity of the radioactive nuclides combined with the harmful effects of radiation on organisms. Furthermore, congenital anomalies or genetic mutations occur as a consequence of exposure to high doses of radiation (Burgio, Piscitelli, & Migliore, 2018; Mettler, 2012).

Radioactivity in living organisms is ascribed to the amount of radioisotopes absorbed by the organs and/or tissues of the organisms, such as uranium, radium, and radon. It is well known that during severe exposure, radioisotopes could greatly damage the exposed organ or a living tissue. Inhaled radon gas is one of the key sources that cause lung cancer (La Verde et al., 2020; Vogiannis & Nikolopoulos, 2015).

Several studies have been conducted to study uranium concentrations and specific activities in food items, most notably rice. For example, a study by Najam et al. measured the radioactivity in different types of rice consumed in Nineveh Governorate (Iraq) using the NaI (Tl) detector. The results of this study showed that the specific activity of uranium-238 and its decay series ranged from 51.15 to 109.26 Bq/kg, with an average of 84.12 Bq/kg (Najam, Tawfiq, & Kitha, 2015). Also, Hameed et al. determined the specific activity and uranium concentrations of different types of rice and table salt consumed in Baghdad (Iraq) using the NaI (Tl) detector. They found that the specific activity of

Authors information:
[a]University of Baghdad, Department of Physics, College of Education for Pure Sciences - Ibn Al-Haitham, Baghdad, IRAQ. E-Mail: uday.t.s@ihcoedu.uobaghdad.edu.iq[1]
[b]Ministry of Education, Directorate General of Vocational Education, IRAQ. E-mail: Adawiyamohsin@gmail.com[2]
[c]University of Baghdad, IRAQ. E-mail: hussein.a.j@ihcoedu.uobaghdad.edu.iq[3]
*Corresponding Author: uday.t.s@ihcoedu.uobaghdad.edu.iq

Received: July 7, 2022
Accepted: December 19, 2023
Published: June 30, 2023

DOI:https//doi.org/10.22452/mjs.vol42no2.1

uranium-238 in rice samples ranged from 5.548 to 27.142 Bq/kg and that in salt samples ranged from Below Detection Limit (BDL) to 7.657 Bq/kg. The average in all samples was 5.548 Bq/kg (Hameed, Rejah, & Muter, 2016). In addition, Asmaa Ahmed Aziz studied and estimated the radioactivity in cereals (including rice) and legumes available in the Iraqi markets using the CN-85 nuclear trace detector. In the study, the concentrations of uranium-238 and radon-222 were calculated, and the results suggested that the maximum levels of uranium and radon were, respectively, 2.63 ppm and 137.17 × 10^2 Bq/m^3 (Aziz, 2018).

Soil contamination with radioactive nuclides could lead to an increase in radioactive concentrations in agricultural crops, including rice. Therefore, the present work aims to evaluate the level of uranium-238 in different types of rice available in the Iraqi market using the nuclear track detector CR-39.

2. Materials and Methods

2.1 Sample Preparation

In the current work, 10 types of widely used rice samples that are available in the Iraqi market from different origins (Iraq, India, USA, and Thailand) were analyzed. After sampling, the samples were dried, and then, they were grounded using an electric grinder, which is made of porcelain, and subsequently sifted using a standard sieve to attain a fine powder form with an equal size. A sensitive scale was used to weigh the rice samples and the sodium hydroxide crystals used in preparing the etching solution. Measured and standard samples weighing 0.5 g were pressed to form round tablets with a diameter of 2 cm and a thickness of 1 mm.

Five different standard concentrations of uranium were prepared with rice namely, 2,8,12,16,20 ppm using acetate powder chemical formula of $UO_2(CH_3COO)_2.2H_2O$ and its molecular weight of 424, which contains 56.13% uranium-238, where the required concentrations were prepared using the following equation (Al-Bayati, 2017):

$$C_1 \times W_1 = C_2 \times W_2, \ldots\ldots\ldots\ldots\ldots(1)$$

where C_1 and C_2 denote the concentrations of uranium of standard and studied rice samples, respectively, and W_1 and W_2 denote the weights of standard and studied rice samples, respectively.

2.2 Measurement Method

One of the most important techniques that can be employed to detect the levels of radioactive radium and uranium in rice samples is the use of solid-state nuclear track detectors (e.g., a CR-39 detector).

Solid-state nuclear track detectors (SSNTDs) are classified as insulating solid materials, which contain narrow trajectories to be occurring radiation damage when heavy ionizing particles pass through such as the proton, α-particle, heavy-ion, and fission fragments. The damaged region is called the radiation damage track or latent track (IAEA, U.S.A, 1987). On the basis of several parameters such as sensitivity, resolution, and variability of response, the most interesting SSNTD materials, and are optically clear amorphous, thermoset plastics (polymers) because of their good homogeneity and isotropy, excellent optical transparency, and uniformity. A plastic material that has all of the aforementioned properties was manufactured by Cartwright and his group. This new device was called CR-39 (Columbia Resin) (Pentreath, 1980; Sabbarese, Ambrosino, & Roca, 2020).

2.3 Irradiation and Chemical Etching

The irradiation of both the standard and studied samples was carried out simultaneously. The CR-39 detector was cut with an approximate area of 1 × 2 cm^2, and the detectors were placed on the samples of unknown concentration and the standard samples in a contiguous manner with the detector. Figure 1 shows the method of placing samples inside the irradiation system. An isotopic neutron source americium–beryllium (^{241}Am–Be) was used for irradiation with an activity of 5.92 × 10^{11} Bq and neutron flux of 5 × 10^3 n·cm^{-2}·s^{-1}.

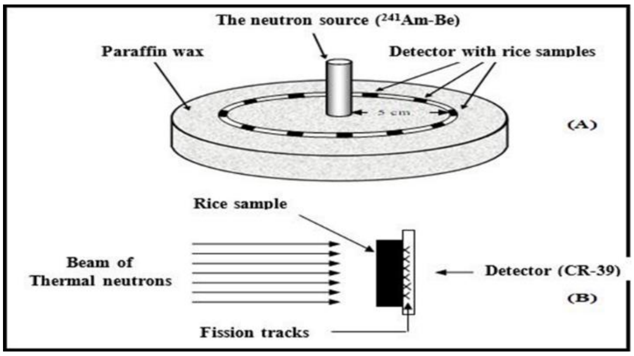

Figure 1. (A) The method of placing the studied and standard samples in paraffin wax in front of the neutron source. (B) The method of placing rice samples with the detector and recording the effects of fission tracks on the detector (Al-Bayati, 2019).

Chemical etching was performed after irradiation using a sodium hydroxide (NaOH) solution (6.25 N), which was prepared by dissolving 62.5 g of NaOH (with a molecular weight of 40 g/mole) in 250 mL of distilled water. After that, the abrasive solution was heated using a water bath at a temperature of 60°C for 5 h to show the effects in the standard and other samples. Then, the samples were washed and dried to move to the measurement process.

Figure 2 displays the method of placing the detectors inside the chemical etching solution.

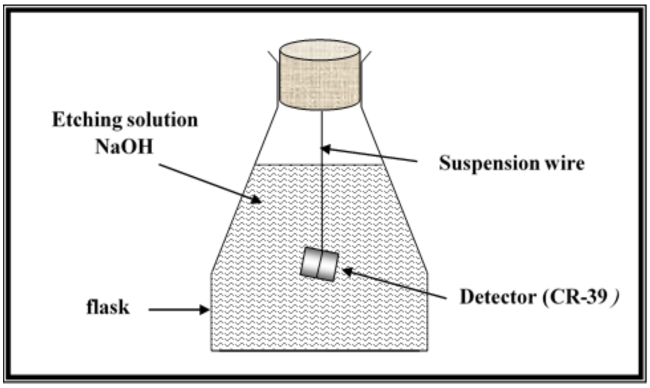

Figure 2. Chemical etching of the CR-39 track detector.

3. Results and Discussion

After the chemical etching phase ended, the stage of microscopic viewing began to detect tracks. This was conducted by selecting the suitable magnification and then by counting the tracks per unit area using a special lens divided into several squares. Ten readings were taken for each sample, and the area of the square was calculated and then divided by the average number of tracks (Nave) per unit area (A) to get the density of tracks (ρ_x) according to the following equation (Shahid, 2007):

$$\rho_x = \frac{N_{ave}}{A} \ldots\ldots\ldots\ldots\ldots\ldots (2)$$

Figure 3 shows the tracks of fission fragments recorded on the nuclear track detector of one of the samples.

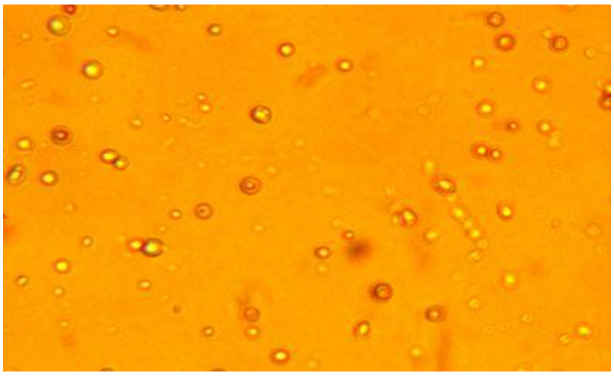

Figure 3. Tracks recorded on the CR-39 detector.

The calibration was carried out by irradiating standard samples containing known concentrations of uranium (C_s) with the samples to be studied using the neutron source (^{241}Am–Be). After irradiation, chemical etching of the detectors was carried out under the same conditions, and the track density (ρ_s) was calculated using a light microscope. The graphical relationship between uranium concentrations (C_s) and track density (ρ_s) was drawn for standard samples, and the relationship was linear, as shown in Figure 4.

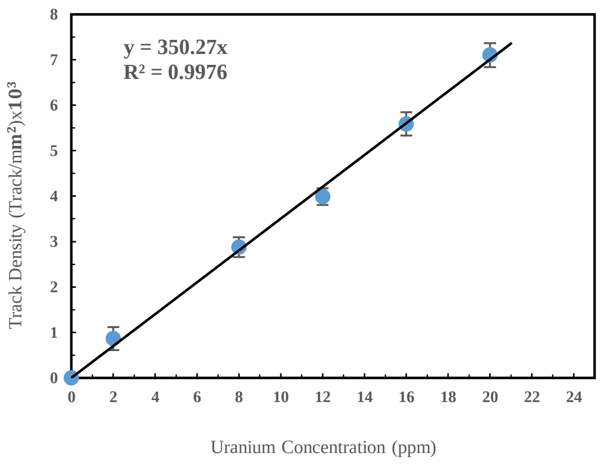

Figure 4. Calibration curves for standard samples.

The concentrations of uranium (C_x) in rice samples were calculated using the following equation (Al-Bayati, 2019);

$$\frac{\rho_x}{\rho_s} = \frac{C_x}{C_s} \rightarrow C_x = C_s\frac{\rho_x}{\rho_s} \rightarrow C_x = \frac{\rho_x}{slope}, \ldots\ldots\ldots\ldots\ldots\ldots (3)$$

where C_s is the concentration of uranium in the standard sample, ρ_s denotes the density of tracks in the standard sample, C_x corresponds to the concentration of uranium in the unknown sample, and ρ_x is the density of tracks in the unknown sample.

The specific activity of the rice samples was also computed using the following equation (Al-Bayati, 2017):

1 ppm =12.35 Bq/kg …………….(4)

Table (1) shows the track density, uranium concentrations, and specific activity in rice samples measured using the CR-39 detector. The results indicated that the highest concentration of uranium was 1.74 ± 0.31 ppm and the highest specific activity was 21.49 ± 3.85 Bq/kg in AL-Eman gold rice and the lowest concentration of uranium was 0.55 ± 0.28 ppm and lowest specific activity was 6.88 ± 3.52 Bq/kg in Abu Araba gold rice. The weighted average for the concentration of uranium and that for specific activity were 1.24 ± 0.99 ppm and 15.31 ± 12.22 Bq/kg respectively.

The levels of uranium concentration and specific activity of the studied rice samples are shown in Figures 5 and 6. In summary, our results are approximately located in the same range of specific activity, which has been reported in the literature (Hameed et al., 2016).

Table 1. Track density, Concentration of uranium, and Specific activity of rice samples.

No.	Rice Type	Origin	Track Density (Track/mm^2)	Uranium Concentration (ppm)	Specific Activity (Bq/kg)
1	Eagle Star (Fakher)	Thailand	488.16 ± 159.97	1.39 ± 0.45	17.21 ± 5.64
2	Jasmine	Thailand	224.85 ± 76.40	0.64 ± 0.21	7.93 ± 2.69
3	Amber	Iraq	463.01 ± 57.41	1.32 ± 0.16	16.33 ± 2.02
4	ADM	USA	602.07 ± 101.48	1.72 ± 0.28	21.23 ± 3.57
5	Cihan	India	507.39 ± 78.83	1.45 ± 0.22	17.89 ± 2.77
6	King Crown	India	451.18 ± 92.51	1.29 ± 0.26	15.91 ± 3.26
7	Abu Araba gold	India	195.26 ± 99.85	0.55 ± 0.28	6.88 ± 3.52
8	AL-Eman gold	India	609.46 ± 109.38	1.74 ± 0.31	21.49 ± 3.85
9	Mahmoud	India	451.18 ± 111.79	1.29 ± 0.31	15.91 ± 3.94
10	Joker	India	544.38 ± 174.20	1.55 ± 0.49	19.19 ± 6.14
	Weighted average			1.24 ± 0.99	15.31 ± 12.22

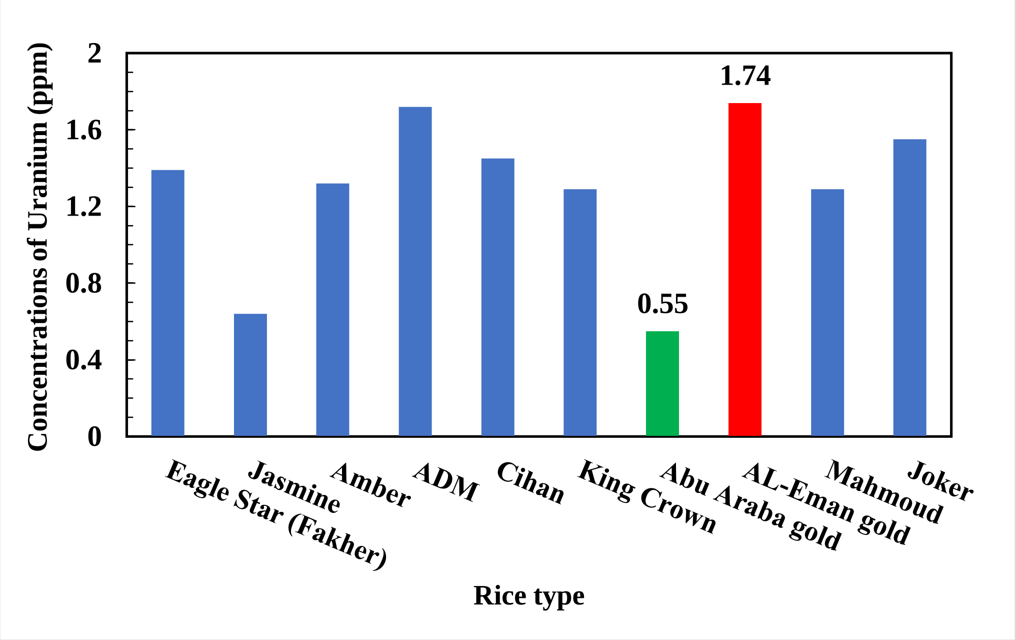

Figure 5. Concentrations of uranium in rice samples.

DOI:https//doi.org/10.22452/mjs.vol42no2.1

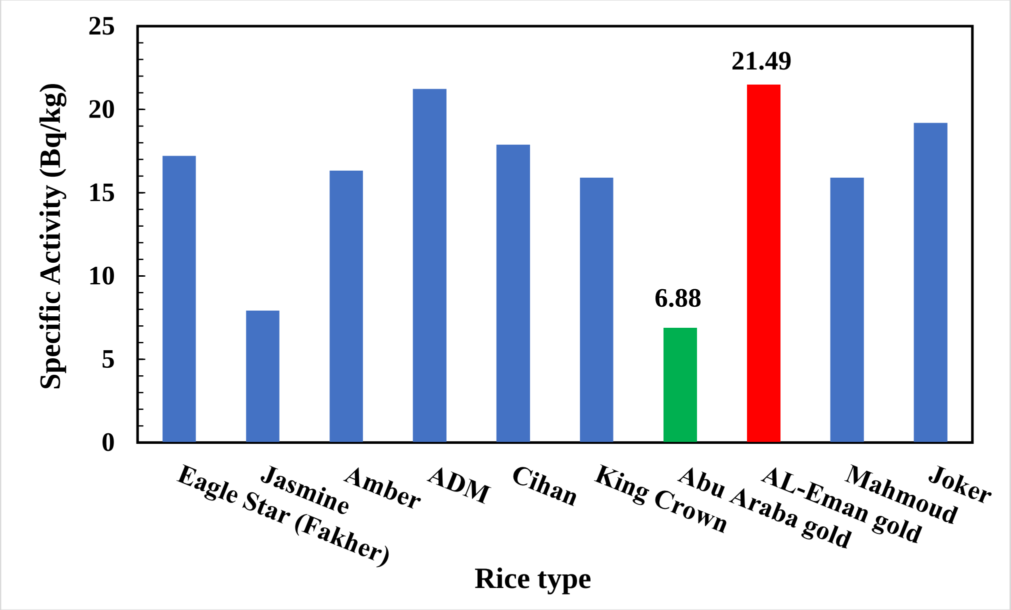

Figure 6. Specific activity in rice samples.

5. Conclusion

The current findings showed that the concentration of uranium-238 ranged from 0.55 ± 0.28 to 1.74 ± 0.31 ppm, with a weighted average of 1.24 ± 0.99 ppm. The highest concentration of uranium of 1.74 ± 0.31 ppm was reported for sample No. 8 (AL-Eman gold rice), and the second highest of 1.72 ± 0.28 ppm was recorded for sample No. 4 (ADM rice). The lowest concentration of uranium of 0.55 ± 0.28 ppm was observed in sample No. 7 (Abu Araba gold rice), and the second lowest of 0.64 ± 0.21 ppm was detected in sample No. 2 (Jasmine rice). On the basis of these concentrations, the specific activity was determined, and its value ranged from 6.88 ± 3.52 to 21.49 ± 3.85 Bq/kg, with an average of 15.31 ± 12.22 Bq/kg. The reason for the difference in values is the different agricultural soils and their geological nature. Moreover, the outcomes display that the concentrations of uranium-238 in the studied rice samples are less than the acceptable limit approved by the UNSCEAR, which amounts to 32 Bq/kg (S. A. Onjefu, 2019; UNSCEAR, 2000). Therefore, on the basis of our analysis, we found that rice consumption by humans would not bring any radioactive hazard.

6. References

Al-Bayati, A. T. (2013). Calculation of the Concentrations of Depleted Uranium in The Diyala River Sediment Samples Using The Nuclear Track Detector CR-39 *Ibn Al-Haitham Journal For Pure and Applied Sciences 26*(3), 122-131.

Al-Bayati, A. T. (2017). Determination of the concentrations for radioactive elements around AL-Tuwaitha center using gamma-ray spectroscopy and CR-39 detectors. *Ph. D. Thesis, College of Education for Pure Science Ibn Al-Haitham, University of Baghdad*.

Al-Bayati, A. T. (2019). Measurement of uranium concentration in the water samples collected from the areas surrounding in Al-Tuwaitha nuclear site using the CR-39 detector. *Paper presented at the Journal of Physics: Conference Series*, IOP Publishing, V.(1234)

Aziz, A. A. (2018). Evaluation of radioactivity of cereals and legumes using a nuclear impact detector CN-85. *Iraqi Journal of Physics, 16*(38), 139-146.

Burgio, E., Piscitelli, P., & Migliore, L. (2018). Ionizing radiation and human health: Reviewing models of exposure and mechanisms of cellular damage. An epigenetic perspective. *International journal of environmental research and public health, 15*(9), 1971.

El-Arabi, A., Abbady, A. G., & Hussein, A. (2006). Gamma-ray measurements of natural radioactivity in sedimentary rocks from Egypt. *Nuclear Science and Techniques, 17*(2), 123-128.

Hameed, B. S., Rejah, B. K., & Muter, S. S. (2016). Study the Concentration of Naturally Occurring Radioactive Materials in the Samples of Rice and Salt in Baghdad Governorate. *Al-Nahrain Journal of Science, 19*(1), 104-109.

IAEA. (U.S.A, 1987). "Principles, Techniques and Applications of Solid State Nuclear Track Detectors."

La Verde, G., D'Avino, V., Sabbarese, C., Ambrosino, F., Roca, V., Raulo, A., & Pugliese, M. (2020). Radiation Protection Legislation and Sustainable Development of a Rural Green Tuff Village of Ischia Island. *Sustainability, 12*(20), 8374.

Melquiades, F., & Appoloni, C. (2002). 40K, 137Cs and 232Th activities in brazilian milk samples measured by gamma ray spectrometry. *Journal of Pure and Applied Physics, 40*, 5-11.

Mettler, F. A. (2012). Medical effects and risks of exposure to ionising radiation. *Journal of Radiological Protection, 32*(1), N9.

Najam, L. A., Tawfiq, N. F., & Kitha, F. H. (2015). Measuring radioactivity level in various types of rice using NaI (Tl) detector. *Am J Eng Res, 4*(3), 126-132.

Pentreath, R. (1980). Nuclear Power, Man and the Environment (1st ed.)., Routledge. https://doi.org/10.4324/9780429278549.

S. A. Onjefu, M. H., H. Katangolo, M. Zivuku, J. Abah and M.K. Mutorwa. (2019). "Measuring Natural Radioactivity Concentration in Various Types of Rice Consumed in Windhoek, NAMIBIA. *Nigerian Journal of Physics., 28*(2), 124.

Sabbarese, C., Ambrosino, F., & Roca, V. (2020). Analysis by Scanner of Tracks Produced by Radon Alpha Particles in CR-39 Detectors. *Radiation Protection Dosimetry, 191*(2), 154-159. doi: 10.1093/rpd/ncaa140

Shahid, M. (2007). Improvements and Calibration of Nuclear Track Detectors of Rare Particle Searches and Fragmentation Studies. *Ph.D. Thesis, University of Bologna, Italy, 12*.

UNSCEAR. (2000). Sources and effects of ionizing radiation, 2008. *Report to the General Assembly with Annex B: Exposures from Natural Sources of Radiation*.

Vogiannis, E. G., & Nikolopoulos, D. (2015). Radon sources and associated risk in terms of exposure and dose. *Frontiers in public health, 2*, 207.

MALAYSIAN JOURNAL OF SCIENCE
MJS
ISSN 1394-3065

Regular Issue

Malaysian Journal of Science 42 (2): 7-15 (June 2023)
https://mjs.um.edu.my

THE EFFECTIVENESS OF APPLICATIONS OF BETEL (Piper Betel Linn.) LEAF EXTRACT AND BACTERIOCIN FOR TEAT DIPPING DURING MILKING HANDLING IN INDONESIAN DAIRY FARMING

Iyep Komala[1a], Irma Isnafia Arief[2a]*, Afton Atabany[3a], Lucia Cyrilla ENSD[4a]

Abstract: This study aims to investigate the effectiveness of teat dipping using sirih leaf extract (Piper betle) and bacteria in dairy farms located in Cijeruk Subdistrict, Bogor Regency, West Java. The research employs an experimental design utilizing a Completely Randomized Design (CRD) with four treatments: (1) teat dipping with masofilm (2% iodine) as the positive control, (2) teat dipping with bacteriocin (protein content = 11.17 g mL-1) (P1), (3) teat dipping with betel leaf extract (25% concentration-based) (P2), and (4) teat dipping without any additional treatment, serving as the negative control. Each treatment is replicated three times. The observed parameters include the reduction in somatic cell count (SCC) and total plate count (TPC) in cow's milk. Data were collected through sampling from 12 cows and analyzed using milk quality analysis to assess the conditions of dairy farms in Cijeruk Subdistrict.

Keywords: *Somatic cell count, teat dipping, total plate count*

1. Introduction

Milk, a food source of livestock origin, contains high nutritional value and serves as an essential source of animal protein needed to improve people's quality of life. In 2021, the population of dairy cows in Indonesia was approximately 600,000 heads, with milk production reaching almost 997,000 tons (Statistical Data on Livestock and Animal Health, 2021). However, the population and productivity of dairy cows do not match the level of milk consumption of the Indonesian population, which consists of 268 million people. According to data from the Central Statistics Agency (2021), Indonesia's milk protein needs reached 4.3 million tons, but only 997 thousand tons of fresh milk were produced domestically. Consequently, fresh milk in Indonesia meets only 22% of the national demand, and 78% comes from imports, resulting in a high level of milk consumption. One of the factors that most often causes low milk production is inflammation of the udder in dairy cows, commonly known as mastitis (Wahyuni et al., 2021). Milk consumption in Indonesia remains relatively low compared to other countries, despite milk's numerous benefits for growth. Milk is crucial for cell regeneration, strengthening bones and teeth, supporting physical growth, increasing intelligence, preventing stunting in children, and enhancing body immunity (Belitz et al., 2009; Muehlhoff et al., 2013). Therefore, minimizing the potential for infection and disease in dairy farming is of urgent importance.

Mastitis, an inflammatory disease of the udder caused by microorganisms such as Streptococcus bacteria, often infects dairy cattle in Indonesia and results in significant losses for dairy farms, including the cost of care and treatment, decreased milk production, and decreased milk quality (Surjowardojo, 2011). Livestock productivity declines due to the udder becoming inflamed, hardened, and even bleeding from infections caused by pathogenic microorganisms (Riyanto et al., 2016). Consequently, it is essential to implement disease prevention management through hygienic milking procedures, including teat dipping, at every milking activity.

Teat dipping is a preventive measure aimed at improving hygiene by immersing the nipples in an antiseptic solution to prevent bacteria from entering the nipple canal before and after milking. Mastitis remains the most prevalent bacterial disease on dairy farms, and adult dairy cows require treatment with antimicrobials to prevent it (Pereyra et al., 2015). Povidone-iodine, a chemical antiseptic capable of killing bacteria within 3-5 minutes, is a commonly used antimicrobial in Indonesia for teat dipping. However, this chemical compound has a disadvantage: it can leave chemical residues in milk, leading to contamination (Aprilia et al., 2016). To address bacterial contamination and the incidence of mastitis in dairy cow's milk, alternative solutions such as betel leaf extract and bacteriocin can be employed as substitutes for povidone-iodine in teat dipping to determine milk quality in dairy cows.

As awareness of the adverse effects of chemical products grows, the importance of natural products in health and medicine also increases due to their perceived safety, affordability, and fewer side effects. One such medicinal plant is the betel leaf (Piper betel Linn.), which has essential oil and extract that function as a fungicide and bactericide, exhibiting activity against

Authors information:
[a]Jl. Raya Dramaga, Babakan, Departement of Animal Production and Technology, Faculty of Animal Science, IPB University, Bogor, INDONESIA. E-mail: iyepko@apps.ipb.ac.id[1]; isnafia@apps.ipb.ac.id[2]; aftonat@apps.ipb.ac.id[3]; luciacyrilla@apps.ipb.ac.id[4]
*Corresponding Author: isnafia@apps.ipb.ac.id

Received: June 6, 2022
Accepted: September 2, 2022
Published: June 28, 2023

DOI:https//doi.org/10.22452/mjs.vol42no2.2

various Gram-positive and Gram-negative bacteria. According to Komala (2003), betel leaf extract, using an absolute methanol solvent at concentrations of 50% and 25%, has superior antibacterial power compared to bacitracin 10 U, chloramphenicol 30g, streptomycin 10g, sulfonamides 300 g, and vancomycin 30 g. Based on the antibacterial potency of betel leaf, this study investigates the benefits of betel leaf as a natural antimicrobial, with the expectation that it can be used as an aseptic agent during milking to reduce pathogenic bacterial contamination in cow's milk.

Bacteriocins are peptide compounds produced by lactic acid bacteria that have antimicrobial activity. This antimicrobial compound is non-toxic to humans, easily degraded by proteolytic enzymes, does not harm the intestinal microflora because it is easily digested by digestive enzymes, and is stable to changes in pH and temperature (Hata et al., 2010). Consequently, bacteriocins can be used as biopreservatives in both fresh and processed food products. The use of bacteriocins, such as plantaricin IIA-1A5, as a natural biopreservative containing antimicrobial compounds can damage and kill pathogenic bacteria like S. aureus and E. coli, which often contaminate cow's milk during the process (Arief et al., 2015a). Plantaricin IIA-1A5, isolated from Lactobacillus plantarum IIA-1A5, inhibits the growth of pathogenic bacteria by damaging cell membranes (Arief et al., 2015a; Fatmarani et al., 2018). Therefore, it is necessary to analyze the improvement of milk quality through the application of bacteriocin biopreservatives during the handling of milking in smallholder dairy farms. This study aims to determine the effectiveness of teat dipping with betel leaf extract (Piper betel) and bacteriocin compared to iodine on the quality of dairy cow's milk in Cijeruk farm, Bogor, West Java.

2. Methodology

2.1 Extraction of Betel Leaves

The extraction of betel leaf was performed according to the method proposed by Poeloengan et al. (2006) using ethanol extraction, since this is the extract that has the best effectiveness in killing bacteria that cause mastitis in dairy cows (Poeloengan et al. 2006).

2.2 Bacteriocin Production (Arief et al 2015a)

This study utilizes bacteriocins produced by the Animal Product Technology Laboratory. These bacteriocins are isolated from lactic acid bacteria Lactobacillus plantarum IIA-1A5, which were grown in cheese-whey media. The bacteriocins are in liquid form and constitute antimicrobial peptide compounds (Arief et al., 2015a; Arifin et al., 2020).

2.3 Bioaseptic intervention treatment of betel leaf extract and bacteriocin

The study was conducted on 12 cows during their normal lactation period, specifically from the 3rd to the 5th month. Each cow had two quarters sampled, resulting in a total of 24 quarters used in the research. The dipping treatment stage of the study spanned 22 days. Farmers whose cows were selected as research samples received instructions and were provided with a teat dipper, as well as solutions of iodine, betel leaf extract, and bacteriocin. Teat dipping was carried out by the farmer, who immersed each nipple into a teat dipper containing a liquid of iodine, betel leaf extract, or bacteriocin for 5 seconds per nipple.

The treatments were as follows:

Positive control = teat dipping with masofilm (2% iodine)

Treatment 1 = teat dipping with bacteriocin (protein content = 11.17 g mL-1 based on Soenarno (2019))

Treatment 2 = teat dipping with betel leaf extract (25% concentration based on Komala (2013))

Negative control = teat dipping without any additional treatment

2.4 Sampling

Milk sampling occurred on days 0, 7, 14, and 21. Collection took place in the morning after the cows had been bathed, using an aseptic method that involved cleaning the cow's nipples with 70% alcohol. Pre-labeled test tubes were prepared to prevent errors. The first and second jets of milk were discarded, and the third and subsequent jets were collected in sterile sample tubes, labeled with a code, containing 10-15 ml of milk. The samples were placed in a cool box with an ice pack, maintaining a temperature between 4-7°C. Samples were then transported to the laboratory for immediate analysis.

DOI:https//doi.org/10.22452/mjs.vol42no2.2

2.5 Total Microbial Analysis

The microbiological quality of fresh cow's milk includes an analysis of Total Plate Count (TPC). TPC measurement is performed by taking 25 mL of fresh cow's milk and placing it in 225 mL of Buffered Peptone Water (BPW, Oxoid) solution. Dilutions of 10-4, 10-5, and 10-6 are prepared. Plate Count Agar (PCA, Oxoid) media is poured into a petri dish containing 20 mL of the solution and homogenized, forming a figure-eight pattern. The petri dish is then incubated upside down for approximately 24 hours at 37°C. Aerobic bacterial colonies will appear white. Colony counts are calculated based on the number of eligible colonies (25-250 colonies). Microbial colonies are quantified using the Standard Plate Count (SPC) method (BAM, 2001), applying the following formula.

$$\mathrm{cfu/m} = \frac{\mathrm{N\ cup}}{(\mathrm{n1} + (0.1 \times \mathrm{n2})) \times \mathrm{d}}$$

Explanation:

N : Number of different colonies in the counting range (25-250 colonies)

n1 : Number of fit plates whose colonies can be counted

n2 :Number of second plates whose colonies be counted

d : First dilution that counts

2.6 Total of Somatic Cell (object-glass Count)

Somatic Cell Count (SCC) testing employs the method outlined by Lukman et al. (2012). The object-glass is cleaned with a 70% alcohol solution and placed on printed paper or a square pattern measuring 1 x 1 cm². The milk sample is first homogenized, and then 0.01 ml of milk is pipetted using a Breed pipette and dripped directly above the 1 cm² box. The milk samples are spread within the 1 cm² square on the object-glass. Breed staining is performed once the milk sample on the glass object is dry. The object-glass is immersed in an alcohol-ether solution for 2 minutes, and subsequently stained by placing it in a methylene blue Löffler solution for 1-2 minutes. The object-glass is then immersed in a 96% alcohol solution for approximately 1 minute to remove any remaining adhering dye. The number of somatic cells is calculated by examining 30 fields of view, totaling the somatic cells, and dividing by the number of fields of view to determine the average number of somatic cells. Once the average number of somatic cells is known, calculations are conducted using the following formula:

Number of Somatic Cells
= microscope factor (400 000) x average number of somatic cells

2.7 Physicochemical Characteristics of Fresh Milk

Chemical characteristics, including fat content, lean dry matter (BKTL), specific gravity, lactose, and protein content, were analyzed using a Milkoester (Milkotester LTD; model Eco; serial 35674). A 25 mL fresh milk sample was taken and poured into a cuvette (25 mL). The cuvette was then inserted into the designated slot in the Milkoester. After selecting the desired analysis parameters, the start button was pressed. The Milkoester produced results within 10 minutes and printed them automatically. pH measurements were conducted according to AOAC (2005). A 10 mL milk sample was prepared, and a calibrated pH meter (Hanna) was used, with calibration points at pH 4 and 7. The pH value of the milk was read and recorded.

2.8 Experiments

The study used a Randomized Block Design. The data were processed by analysis of variance (ANOVA). For microbial population analysis, before the analysis of variance, the microbial population data was transformed into a log value of 10. In the case the analysis showed that the treatment had a significant impact on the observed variables, a comparative test was carried out using the Tukey test (Steel et al., 1997).

3. Results & Discussion

3.1 Total of Microbial Contamination in Milk

The microbiological quality of dairy cow's milk serves as a fundamental reference in determining the number of microbes from the bacterial group present. The maximum number of bacteria is a standard requirement for dairy cow's milk. Consequently, environmental factors play a crucial role in the physiological processes of the livestock body, ultimately affecting production capacity and milk quality (Mutaqin et al., 2021). The results of the bacterial counts from each treatment are presented in Table 1.

Table 1. Total microbial milk samples from dairy farms in Cijeruk

Treatment	Day of Test – (Log cfu/mL) D0	D7	D14	D21	Average
Positive Control (teat dipping iodine)	3.84± 0.09a	4.14 ± 0.09b	4.01 ± 0.02a	3.77 ± 0.27a	3.94 ± 0.31a
Teat dipping bacteriocin	4.00 ± 0.02a	4.14 ± 0.07b	4.29 ± 0.06b	4.27 ± 0.04b	4.01 ± 0.07a
Teat dipping of betel leaf extract	3.98 ± 0.01a	3.28 ± 0.05a	4.44 ± 0.05c	4.40 ± 0.02c	4.02 ± 0.03a
Negative Control	4.0 ± 0.08a	4.41 ± 0.03c	4.52 ± 0.42d	4.37 ± 0.04d	4.22 ± 0.07b

Note: SNI (Indonesian standard) is 5 log cfu/ml or 10^5 cfu/ml(100,000 cfu/ml) Different letters in the same column show a significant difference.

The bacteriocin treatment was effective in maintaining bacterial contamination in fresh milk at the same level as iodine until the 7th day of treatment and was better than the betel leaf extract on the 7th, 14th, and 21st days. The treatment with bacteriocin and betel leaf extract for teat dipping was not significantly different from the treatment using iodine and was even able to reduce the level of bacterial contamination compared to the control (without immersion). Natural compounds such as betel leaf extract and bacteriocin can replace iodine, a chemical for teat dipping in dairy cows in the tropics. An optimal concentration of 25% for betel leaf extract and 1% for bacteriocin (with a protein content of 11.17 gmL-1) can be used as a natural ingredient for teat dipping in dairy farms in the long term.

Iodine functions as an antimicrobial substance that can kill microorganisms, including bacteria, fungi, viruses, protozoa, and spores. The ability of iodine to reduce inflammation is due to its ability to coat the udder with the active substance in the solution, preventing the entry and development of bacteria that cause udder infection (Priono et al., 2016). Iodine's antimicrobial mechanism is caused by its strong oxidizing effect on amino acid groups, nucleotides, and double bonds of unsaturated fatty acids of microorganisms (Noor and Apriasari, 2014). Teat dipping with iodine can reduce inflammation levels because it coats the udder with the active substance in the solution, preventing the entry and development of bacteria that cause udder infection (Priono et al., 2016).

The antibacterial mechanism of bacteriocins and betel leaf extract differs. Bacteriocins are antimicrobial peptides that have bactericidal ability against Gram-positive and Gram-negative bacteria. Bacteriocin plantaricin IIA-1A5 used in this experiment plays a bactericidal role against another bacterial cell, as reported by Arief et al. (2015a). Plantaricin IIA-1A5 displayed a pore-like structure on the surface cells, promoting the release of genetic and proteinaceous materials from the cell, resulting in cell rupture and cell membrane disruption (Arief et al., 2015a). On the other hand, betel leaf extract contains antimicrobial substances such as volatile oils and phenolic components that show antibacterial mechanisms by disrupting cell permeability and causing an effect on unbalanced materials within and outside the cell (Tyagi et al., 2015). Betel leaf extract contains a carboxyl group in the aromatic hydrocarbons of the phenolic compounds that form complexes with extracellular and soluble proteins of bacteria, changing the protein composition that causes bacteria to die (Lubis et al., 2020).

Bacteriocins exhibit antimicrobial activity against foodborne pathogens. Lactic acid bacteria (LAB) are known to produce bacteriocins that display antimicrobial properties against several gram-positive and negative bacteria (Sapatnekar et al., 2010). Lactobacillus plantarum is a bacteriocin-producing strain of LAB known as Plantaricin (Diep et al., 1996; Holo et al., 2001; Maldonado et al., 2003). Bacteriocins generally function by killing bacteria through the formation of pores in the cell membrane, causing the cells to leak and ultimately die (Arief et al., 2015a). Optimal antimicrobial activation of plantaricin PASM1 from Lactobacillus plantarum A-1 ranged from 90% to 100% at a pH range of 5.5 to pH 7 (Gillor et al., 2008). Plantaricin IIA-1A5, belonging to class IIa bacteriocins (Arief et al., 2015a; Mutmainna et al., 2021), can be used as a natural preservative in meat to reduce microbial contamination. Plantaricin IIA-1A5 is also effective as a natural preservative in meat stored at room temperature by inhibiting Escherichia coli and Staphylococcus aureus (Sihombing et al., 2015). Plantarisin IIA-1A5 was found to decrease the total microbe count in fresh milk, and its effective dose for application in dairy smallholder farms is at a concentration of 11.17 g mL^-1 (Soenarno, 2019; Arifin et al., 2020).

Betel leaf contains various elements, such as Si, Cl, Zn, Mg, Ca, and K, which can be used to neutralize acid-base metabolic imbalances in the human body (Periyanayagam et al., 2014). Betel leaf is also rich in metabolites such as volatile oils (safrol, eugenol, eugenol methyl ester, isoeugenol), phenolic components (chavicol, hydroxyl chavicol), hydroxyl

DOI:https//doi.org/10.22452/mjs.vol42no2.2

fatty acids (stearate, palmitic, myristic), and fatty acids (stearic and palmitic), which exhibit antibacterial effects and can be used to treat microbial infections (Bangash et al., 2012). The strong antimicrobial effect of betel leaf is due to the presence of esters, flavonoids, alkaloids, and benzoic acid (Foo et al., 2015). Tannin compounds are also found in betel leaf extract. Tannins are astringents and polyphenols in plants that taste bitter and can bind and precipitate proteins (Subroto, 2006). Tannins can interfere with cell permeability by shrinking their cell walls, which can cause bacterial cells to experience growth disorders or even die (Ajizah, 2004). Extracts of Piper betle Linn exhibit a wide zone of inhibition with minimal inhibitory concentrations against Staphylococcus aureus, Streptococcus pyogenes, Candida albicans, and Trichophyton mentagrophyte (Caburian & Osi, 2010).

The average value of TPC is below the standard set by the National Standards Agency 2009 for the Maximum Limit of Microbial Contamination in Food, which is 1.0 × 106 CFU/mL for TPC. The low number of bacteria in fresh milk is attributed to the practice of cleaning the milking area at least twice a day, before milking in the morning and evening, and washing the nipples before milking. Various microorganisms, with Staphylococcus aureus being the dominant one, including Streptococcus agalactiae, Streptococcus dysgalactiae, and Streptococcus uber, cause 90 to 95% of mastitis infections in the dairy industry, with Staph. aureus being the primary mastitis-causing pathogen (Son et al., 2016). Microorganism contamination in milk cannot be separated from sanitation management practices. (Firman, 2010). Additionally, the possibility of contamination due to the nipple opening being open after the milking process is a period that is highly susceptible to infection as bacteria can enter the udder. The process of subclinical mastitis infection starts when microorganisms enter the gland through the nipple opening, which remains open after the milking process. Microorganisms thrive and spread to the alveoli, causing damage to the milk produced. The invasion of microorganisms in the udder and the resulting inflammatory reactions can damage the udder's cells, leading to impaired milk production and decreased quality (Aprilia et al., 2016). In this study, the application of hygiene and sanitation practices on cijeruk farms has been maximized, resulting in no farms exceeding the SNI threshold for TPC number.

3.2 Total Somatic Count Cells (SCC)

A total of 24 quarter samples were used for the total somatic count directly (Breed method). The parameters used in determining subclinical mastitis based on direct SCC calculations are 400,000 cells/ml (Sudarwanto, 1999). The number of somatic cells is related to the mastitis infection (Son et al., 2016). The results of the SCC test are shown in Table 2.

Table 2. Determination of subclinical mastitis based on SCC (n=24)

Treatment	Total Average of SCC day- (cell/ml)			
	H0	H7	H14	H21
Positive Control (teat dipping iodine)	1.375×10^5 a	8.889×10^4 a	1.524×10^5 a	3.098×10^5 a
Teat dipping bacteriocin	8.727×10^4 a	1.429×10^5 a	1.552×10^5 a	1.322×10^5 a
Teat dipping of betel leaf extract	1.377×10^5 a	1.782×10^5 a	5.778×10^4 a	1.277×10^5 a
Negative control	3.556×10^5 a	3.615×10^5 a	7.133×10^5 b	8.502×10^5 b

Note: a = small amount of SCC (< 4 x 105 cells/ml; no subclinical mastitis); b= high number of SCC (more than 400,000 cells/ml; meaning subclinical mastitis.

Based on Table 2, it is evident that teat dipping treatment is much more effective than no treatment. Iodine, bacteriocin, and betel leaf extract were able to keep the total somatic cell count lower and did not exceed the standard, thereby preventing the occurrence of subclinical mastitis. In contrast, without teat dipping, udders of dairy cows experienced subclinical mastitis on days H14 and H21. The effects of mastitis on productivity, reproductive performance, and product quality have been quantified, and diagnostic tools such as SCC testing are used to identify subclinically infected cows (Ruegg, 2017). Somatic cell count (SCC) concentration is a well-established direct indicator of mammary gland infection, i.e., mastitis (Rainard et al., 2008). No cells/mL or (-) indicates that a farm has implemented good management practices but has not implemented a proper mastitis control program.

SCC of 500,000 cells/mL (1+: mild mastitis; 2+: moderate mastitis; 3+: severe mastitis) indicates that one-third of the quarter of cows on the farm suffer from subclinical mastitis (Sudarwanto & Sudarwika, 2008). Based on Table 2, it was found that 87.5% of the total sample of 24 showed SCC values below the standard mastitis incidence, while 12.5% had subclinical mastitis, which occurred in dairy cows without treatment on the 14th and 21st days of the milking period. Fatmawati et al. (2019) state that if the SCC reaches >500,000 cells/mL, it indicates that one-third of a quarter of dairy cows on a farm suffer from subclinical mastitis. According to Sudarwanto and Sudarnika (2006), a somatic cell count of <400,000 cells/mL of milk is an indication that a farm has implemented good livestock management practices but has not implemented a comprehensive mastitis control program. Management strategies should be recommended to reduce the spread of contagious pathogens (Ruegg, 2017). The FAO and IDF (2011) provide guidelines on milking practices, stating that the application of teat disinfectant to each teat after milking should be a treatment according to national regulations (Ahmed et al., 2021).

A similar study was conducted by Twomey et al. (2000), who used lactacin 3147, a bacteriocin from Latococcus lactis, as a teat dipping treatment in dairy cows. Teat dipping using lacticin 3147 was found to reduce S. aureus contamination in lactating cows, significantly reducing the risk of mastitis. Consistent with the results of the microbial count in milk, teat dipping treatment using iodine, betel leaf extract, and bacteriocin was proven to prevent the incidence of subclinical mastitis in the udders of dairy cows. The limitations of antimicrobial therapy have been recognized, but the use of antibiotics to treat cows affected with some pathogens remains an important tool for mastitis control (Ruegg, 2017). This is related to the antimicrobial compounds contained in each ingredient of the teat dipping solution, i.e., iodine, betel leaf extract, and bacteriocin, as described in the previous section. Betel leaf extract and bacteriocin were found to be effective and no different from iodine as teat dipping ingredients for dairy cows on smallholder farms.

3.3 Physicochemical Properties of Milk

Fresh milk is a liquid that comes from the udders of healthy and clean cows obtained through proper milking, whose natural content has not been reduced or added to, and has not received any treatment except for cooling. Fresh milk must meet certain requirements to be safe for consumption and use in further processing. Therefore, testing the quality of fresh milk must be continuously carried out for a certain period on dairy farms. The results of testing the quality or physiochemical properties of fresh milk produced from the research are shown in Table 3.

Table 3. Physicochemical properties/quality of fresh milk

Parameters	Observation Day					Indonesian Standard
	D0	D7	D14	D21	Average	
pH Value						
Positive Control (teat dipping iodine)	6.75 ± 0.05	6.66 ± 0,08	6.72 ± 0.02	6.63 ± 0.03	6.69 ± 0.06	
Teat dipping bacteriocin	6.62 ± 0.03	6.65 ± 0,05	6.62 ± 0.03	6.68 ± 0.03	6.64 ± 0.03	
Teat dipping of betel leaf extract	6.63 ± 0.02	6.70 ± 0.05	6.62 ± 0.02	6.73 ± 0.08	6.67 ± 0.12	
Negative Control	6.67 ± 0.06	6.67 ± 0.06	6.67 ± 0.06	6.65 ± 0.09	6.66 ± 0.06	
Average	6,65 ± 0.04	6.67 ± 0.06	6.66 ± 0.03	6.67 ± 0.06	6.66 ± 0.06	
Protein Level (%)						≥ 2.80
Positive control (teat dipping iodine)	3.10 ± 0.10	3.08 ± 0.08	3.05 ± 0.13	3.03 ± 0.07	3.06 ± 0.09	
Teat dipping bacteriocin	3.11 ± 0.15	3.13 ± 0.24	3.11 ± 0.15	3.21 ± 0.05	3.14 ± 0.15	
Teat dipping of betel leaf extract	3.20 ± 0.07	3.13 ± 0.05	3.21 ± 0.07	3.25 ± 0.25	3.20 ± 0.11	
Negative control	3.10 ± 0.10	3.10 ± 0.10	3.10 ± 0.10	3.15 ± 0.10	3.11 ± 0.10	
Average	3.13 ± 0.11	3.11 ± 0.12	3.12 ± 0.11	3.16 ± 0.12	3.13 ± 0.11	
Fat Level (%)						≥3.0
Positive control (teat dipping iodine)	2.00 ± 0.30	2.5 ± 0.40	2.61 ± 0.65	3.70 ± 0.22	2.70 ± 0.39 a	
Teat dipping bacteriocin	2.60 ± 0.40	2.1 ± 0.40	2.66 ± 0.45	3.80 ± 0.21	2.85 ± 0.37 a	
Teat dipping of betel leaf extract	2.40 ± 0.90	3.5 ± 0.25	2.40 ± 0.90	2.70 ± 0.11	2.77 ± 0.14 a	
Negative control	1.61 ± 0.24	1.5 ± 0.20	1.60 ± 0.20	0.90 ± 0.40	1.42 ± 0.28 b	
Average	2.15 ± 0.46	2.4 ± 0.31	2.32 ± 0.55	2.78 ± 0.24	2.44 ± 0.30	
Lactose Level (%)						≥4.0
Positive control (teat dipping iodine)	4.60 ± 0.10	4.60 ± 0.10	4.50 ± 0.10	4.50 ± 0.10	4.61 ± 0.14 b	
Teat dipping bacteriocin	4.70 ± 0.20	4.70 ± 0.30	4.70 ± 0.20	4.80 ± 0.10	4.75 ± 0.23 ab	
Teat dipping of betel leaf extract	4.80 ± 0.10	4.75 ± 0.08	4.80 ± 0.10	5.20 ± 0.05	4.93 ± 0.20 a	
Negative control	4.60 ± 0.10	4.60 ± 0.20	4.60 ± 0.10	4.70 ± 0.05	4.68 ± 0.15 ab	
Average	4.68 ± 0.13	4.66 ± 0.17	4.65 ± 0.13	4.80 ± 0.75	4.74 ± 0.18	
Solid Non Fat (%)						≥7.8
Positive control (teat dipping iodine)	8.40 ± 0.2	8.4 ± 0.3	8.3 ± 0.3	8.3 ± 0.1	8.41 ± 0.28	
Teat dipping bacteriocin	8.60 ± 0.4	8.6 ± 0.6	8.6 ± 0.4	8.8 ± 0.2	8.7 ± 0.4	
Teat dipping of betel leaf extract	8.80 ± 0.2	8.7 ± 0.1	8.8 ± 0.2	8.9 ± 0.6	8.85 ± 0.30	
Negative control	8.60 ± 0.2	8.5 ± 0.3	8.6 ± 0.2	8.65 ± 0.05	8.6 ± 0.2	
Average	8.60 ± 0.3	8.6 ± 0.3	8.6 ± 0.3	8.66 ± 0.23	8.64 ± 0.3	

Note: different letters for the same column in each parameter indicate a significant difference ($p<0.05$)

Based on the results of the statistical analysis, it was found that teat dipping treatment and milking time had no significant effect on the pH value, protein content, and solid non-fat content of the fresh milk produced. There was no interaction between the factors of teat dipping treatment and milking time. However, the teat dipping treatment had a P-value < 5%, which indicates that the treatment affected the fat content. In Tukey's test, the control treatment without teat dipping had a lower effect than the other treatments on fat at a significant level of 5%.

Teat dipping treatment and milking time had a significant effect on lactose content (P-value < 5%). In Tukey's test, fresh milk treated with teat dipping iodine had lower lactose content than fresh milk treated with teat dipping betel leaf

DOI:https//doi.org/10.22452/mjs.vol42no2.2

extract. This may be due to the fat content in the betel leaf extract that is included during the milking process.

The requirements for fresh milk include a minimum fat content of 3.0%, solid non-fat (SNF) of at least 7.8%, and protein content of at least 2.8% (National Standardization Agency, 2011). The composition of milk varies depending on several factors. For FH cows, the percentages of water, protein, fat, lactose, ash, and BK are 88.01%, 3.15%, 3.45%, 4.65%, 0.68%, and 11.57%, respectively (Sudono et al., 2003).

The results showed that the pH value, protein content, lactose content, and solid non-fat value of freshly milked milk had values according to Indonesian national standards. However, the fat content of fresh milk in all treatments was lower than the Indonesian national standard due to the feed used, which was mostly forage and less concentrated, resulting in a low fat content. Moreover, consumers also prefer low-fat milk. Dairy farmers provided forage at an average of 47.32 kg head-1 day-1, with an average milk production of 11.29 L head-1 day-1. The feeding of forage based on body weight is estimated only based on the body shape and experience of the dairy farmer. Farmers give concentrate, which has a crude protein content of 14%, with an average of 9.99 kg head-1 day-1. However, the crude protein content of the concentrate fed to cows is lower than the standard, which should contain 19.04% crude protein. Improving the quality of concentrate feed can improve the milk productivity of lactating cows, by feeding forage and concentrate that are adjusted to the live weight of lactating cows. Therefore, the fat content of milk sourced from concentrates is lower than 3.00%.

The effectiveness of various treatments on fresh milk has been studied extensively, with researchers exploring different approaches. For example, a study by Wahyuningtyas et al (2021) found that teat dipping before milking reduced the number of Escherichia coli bacteria and total microbes in milk without compromising its quality (as measured by Indonesian standards). Additionally, researchers have investigated the use of a bio preservative called Plantaricin IIA-1A5, which has been shown to preserve milk quality according to SNI standards and reduce the presence of pathogenic bacteria during storage at room temperature and in cold temperatures (Soenarno et al 2020; Arief et al 2021). These findings demonstrate that Plantaricin IIA-1A5 can be an effective bio preservative or bio aseptic for fresh milk.

4. Conclusion

The teat dipping treatment applied during the milking process for 21 days at a dairy farm in Cijeruk village, Bogor-West Java-Indonesia was successful in improving the microbiological quality of fresh cow's milk and reducing the incidence of subclinical mastitis in cow udders. Teat dipping using natural ingredients such as betel leaf extract and bacteriocin can replace chemical iodine. The physicochemical quality of freshly milked cow's milk was not affected by the teat dipping treatment. Therefore, teat dipping using betel leaf extract and bacteriocin is highly recommended for the management of milking in dairy farms. The recommended concentration for bacteriocin is a liquid with a protein content of 11.17 g/mL, while for betel leaf extract, a 25% concentration is recommended. The practical application of teat dipping is conducted after the milking process for five seconds on each nipple

5. Acknowledgement

This research was funded by Basic Research 2020/2021 Number: 1/E1/KP.PTNBH/2021 and Number: 1930/IT.3L1/PN/2021), continued Research Funding on 2022 from the Directorate of Higher Education, Ministry of Education and Culture, Republic of Indonesia.

6. References

Ahmed R N., Bamigboye M O., Ajijolakewu K A., Idris S O., Bamigboye N T A. (2021). Isolation, characterization and antibacterial screening of antibiotics produced from streptomyces isolated from dumpsite soils in Ilorin, North Central Nigeria. *Malaysian Journal of Science*. 40(3):1-17.

Ajizah A. (2004). Sensitivitas *Salmonella typhimurium* terhadap ekstrak daun *Psidium guajava L*. *Bioscientiae*. 1(1): 31-38.

Aprilia P R., Santoso S A B., Harjanti D W. (2016). Jumlah Staphylococcus aureus dan kandungan nutrien susu akibat dipping puting menggunakan ekstrak daun belimbing wuluh (*Averrhoa bilimbi Linn*) pada sapi perah penderita mastitis subklinis. *Jurnal Ilmu-Ilmu Peternakan*. 26(1): 43-51.

Arifin M., Budiman C., Fujiyama K., Arief, I I. (2020). Kinetic and thermodynamic study of plantaricin IIa-1a5, a bacteriocin produced by Indonesian probiotic *Lactobacillus plantarum* IIa-1a5. *Protein and Peptide Letters*. 28(6): 680-686.

Arief, I I., Budiman C., Jenie, B S L., Andreas E., Yuneni, A. (2015a). Plantaricin IIA-1A5 from *Lactobacillus plantarum* IIA-1A5 displays bactericidal activity against *Staphylococcus aureus*. *Beneficial Microbes*. 6(4): 603-613.

Arief, I I., Jenie B S L., Astawan M., Fujiyama K., Witarto A B. (2015b). Identification and probiotic characteristics of lactic acid bacteria isolated from Indonesian local beef. *Asian Journal Animal Science*. 9(1): 25-36.

Arief, I I., Nandika A., Wulandari Z. (2021). Milk quality preservation through the application of plantaricin IIa-1a5 as biopreservatives on fresh milk at dairy cow farm. *Agricultural Mechanization in Asia, Africa, and Latin America*. 51(3): 1-12.

DOI:https//doi.org/10.22452/mjs.vol42no2.2

Bangash M N., Kong M L., Pearse R M. (2012). Use of inotropes and vasopressor agents in critically ill patients. *Br J Pharmacol*. 165(7): 2015-2033.

Belitz HD., Grosch W., Schieberle P. 2009. Milk and Dairy Products in Food Chemistry. Springer. Berlin.

Caburian, A B., Osi M O. (2010). Characterization and evaluation of antimicrobial activity of the essential oil from the leaves of *Piper betle L. E-int. Sci. Res. Journal*. 2(2): 1-13.

Fatmarani R., Arief I I., Budiman C. (2018). Purification of bacteriocin from *Lactobacillus plantarum* IIa-1a5 grown in various whey cheese media under freeze dried condition. *Tropical Animal Science Journal*. 41(1): 53-59.

Hata E., Katsuda K., Kobayashi H., Uchida I., Tanaka K., Eguchi M. (2010). Genetic variation among *Staphylococcus aureus* strains from bovine milk and their relevance to methicillin-resistant isolates from humans. *Journal of Clinical Microbiology*. 48(6): 2130-2139.

Komala I. (2003). Pengaruh ekstrak daun sirih (*Piper betle Linn*) terhadap bakteri penyebab mastitis. [Skripsi]. Fakultas Peternakan, Institut Pertanian Bogor.

Lubis RR. , Marlisa, Wahyuni DD. 2020. Antibacterial activity of betle leaf (Piper betle l.) extract on inhibiting *Staphylococcus aureus* in conjunctivitis patient. *Am J Clin Exp Immunol* 9(1):1-5

Lukman D W., Sudarwanto M., Sanjaya A W., Purnawarman T., Latif H., Soejoedono R R. (2012). Pemeriksaan Mastitis Subklinis. Higiene Pangan Asal Hewan. Bogor: Kesmavet FKH IPB. 35-38.

Muehlhoff E., Bennett A., McMahon D., 2013. Milk and Dairy Products in Human Nutrition. FAO- Rome.

Mutmainna A., Arief I I., Budiman C. (2021). The growth and production of antimicrobial compounds from *Lactobacillus plantarum* IIA-1A5 on cheese whey medium. *J. Indonesian Trop. Anim. Agric*. 46(2): 173-184.

Mutaqin B K., Tasripin D S., Adriani L., Tanuwiria U H. (2021). Microbial biomass testing and degree of acidity of milk dairy cows provided complete feed supplementation protein, fat, minerals (pfm) and direct fed microbial. *Jurnal Sumber Daya Hewan*. 2(1): 1-4.

Noor M A., Apriasari M L. (2014). Antibacterial effectivity of methanol extract from mauli banana stem (*Musa acuminata*) and 10% povidone iodine against *Streptococcus* mutans. *Jurnal PDGI*. 63(2): 12-24.

Pereyra L C., Montana J R G., Benech A., Dibarrat J A., Martin M J., Perini S., Abreu M C., Silva D A., Rodriguez P. (2015). Evaluation of three therapeutic alternatives for the early treatment of ovine pregnancy toxaemia. *Irish Veterinary Journal*. 68(25): 1-7.

Periyanayagam K., Mubeen M., Basha S S. (2014). Anatomical investigation on the leaves of piper betle (L) var. sirugamani 1 (sgm1) links an ethnomedical important. *International Journal of Pharmtech Research.* 6(1): 244-251.

Poeloengan M., Komala I., Noor S M., Andriani., Rianti S R P. (2006). Activity water extract of essential oil and ethanol extraction op piper bittle leaves against bacteria isolated from sub clinical mastitis cattle. *Seminar Nasional Teknologi Peternakan dan Veteriner*.

Priono D., Kusumanti E., Harjanti D W. (2016). Jumlah bakteri *Staphylococcus aureus* dan skor california mastitis test (cmt) pada susu kambing peranakan etawa akibat dipping ekstrak daun babadotan (*Ageratum Conyzoides L.*). *Jurnal Ilmu-Ilmu Peternakan*. 26(1): 52-57.

Riyanto J., Sunarto., Hertanto B S., Cahyadi M., Hidayah R., Sejati W. (2016). Milk quality and production of dairy cow mastitis patients who get treatment of antibiotics. *Jurnal Penelitian Ilmu Peternakan*. 14(2): 30-41.

Sihombing D E., Arief I I., Budiarti S. (2015). Application of antimicrobial agents produced by *Lactobacillus plantarum* IIA-1A5 as natural preservative on beef during room temperature storage. *Advance Journal Food Sci.Technol*. 8(3): 251-255.

Sudono A., Fina., Budi. (2003). Beternak Sapi Perah Secara Intensif. Depok: Penerbit Agromedia Pustaka.

Surjowardojo P. (2011). Incidence level of mastitis with whiteside test on milk yield of dairy cows.

Jurnal Ternak Tropika. 12(1): 46-55.

Steel R G D., Torrie J H., Dicky D A. (1997). Principle and procedure of statistic. A Biometrical Approach. 7.

Tyagi B., Dubey A., Verma AK., Tiwari S. 2015. Antibacterial activity of phenolics compounds against pathogenic bacteria. *Int. J. Pharm. Sci. Rev. Res*. 35(1) 04: 16-18

Wahyuni S., Kentjonowaty I., Humaidah N. (2021). The effectiveness of herbal dipping teats as a subclinical mastitic prevention. *Jurnal Dinamika Rekasatwa*. 4(1): 231-249.

MALAYSIAN JOURNAL OF SCIENCE
MJS
ISSN 1394-3065

Regular Issue

Malaysian Journal of Science 42 (2): 16-21 (June 2023)
https://mjs.um.edu.my

THE BENEFITS OF FERMENTED GOAT'S MILK WHEY MASK WITH HONEY AND RED FRUIT (Pandanus conoideus) AS ANTIOXIDANT AGENT

Yulia Yasmin Pratiwi[1a], Irma Isnafia Arief[2a]*, M.Sriduresta Soenarno[3a]

Abstract: Fermented goat's milk whey, combined with honey and red fruit extract, can be used to produce face masks to enhance their effectiveness. This study aimed to ascertain the optimal formulation of the fermented whey mask and its physical characteristics and antioxidant properties. The physical characteristics tested for the fermented whey masks included pH, water activity, spreading ability, drying time, and antioxidant properties to identify the formulation that yielded the most favorable results. The study employed a completely randomized factorial design for testing. The results indicated that masks with an addition of 10% honey were more effective in enhancing the quality of the masks, as they yielded superior values in terms of pH, water activity (aw), spreading ability, drying time, and antioxidant activity. This is substantiated by the pH value of the fermented whey mask with the addition of 10% honey, which was closest to the natural skin pH, specifically between 6.71 and 7.48. The water activity value of the fermented whey mask with the addition of 10% honey also fell within a range of 0.670 to 0.751, which is lower than that of the mask with 5% honey. The spreading ability test results of fermented whey masks with the addition of 10% honey demonstrated higher diameter values, ranging from 4.47 to 5.20 cm. Furthermore, the antioxidant inhibition capacity values of masks with the addition of 10% honey were higher than those with 5% honey, ranging from 33% to 47%. Organoleptic tests on masks with the addition of 5% and 10% honey did not yield different results, and the panelists' acceptance of the mask preparations was relatively high. The findings from this study could be further developed into shelf-life stability and dermatological testing, as they hold potential for commercial development.

Keywords: *Fermented whey, honey, mask, red fruit*

1. Introduction

The use of masks is a facial skin treatment method that falls under deep cleansing (Tyas, 2018). This process works intensively to remove dirt, germs, and dead skin cells from the face's surface. Whey, a liquid product produced during the creation of cheese, casein, and similar products, is obtained by separating the curd from the liquid throuhe coagulatiss (Codex, 1995). Edwards and Jameson (2020) suggest that the immunoglobulins and lactoferrin content in whey can serve as effective raw materials for face masks. Whey derived from goat's milk enhances the efficacy of the raw ingredients in face masks. This is because goat's milk has smaller fat globules than cow's milk, making the mask's nutrients more readily absorbed into the skin.

Honey is rich in vitamins B1, B2, B3, B5, C, A, E, and flavonoids. Flavonoids are known to have antibacterial mechanisms due to osmotic pressure, acidity, and the presence of inhibin chemicals, which collectively inhibit the growth of contaminating microbes (Rio *et al.*, 2012). The phenol concentration in honey can also influence viscosity and pH, making bacterial growth challenging (Nadhila, 2014). Honey possesses various skin benefits, including acting as a natural antioxidant that eliminates bacteria and germs causing acne, a natural antiseptic that cleans acne wounds, and an anti-inflammatory that reduces wound inflammation (Vallianou *et al.*, 2014). Honey also serves as an osmotic wound cleanser, absorbs water, moisturizes the skin, and contains natural probiotic substances (Sabry, 2009).

Red fruit extract contains tannins, vitamin C, flavonoids, and natural antioxidant components such as alpha and beta carotene, tocopherols, and minerals (Murtiningrum *et al.*, 2012). These are beneficial for reducing reactive oxygen species (ROS) and free radicals formed during cell metabolism (Ichihsai *et al.*, 2009). Tannins and flavonoids are known to act as tyrosinase inhibitors, suppressing the process of melanogenesis. Additionally, flavonoids can prevent skin pigmentation caused by ultraviolet (UV) radiation exposure (Chang, 2009).

Lactic acid bacteria are expected to enhance the mask's ability to inhibit pathogenic bacteria (Dewi and Rahmiati, 2019), produce antibacterial compounds (Desniar *et al.*, 2012), and act as a natural stabilizer and thickener of dairy products. They produce exopolysaccharides (EPS) that benefit human health due to their anticancer, antiulcer, anti-inflammatory, anti-infective, and immune-stimulant properties (Halim and Zubaidah, 2013). Given these beneficial functions of whey, honey, and red fruit extract,

Authors information:
[a]Jl. Raya Dramaga, Babakan, Departement of Animal Production and Technology, Faculty of Animal Science, IPB University, Bogor, INDONESIA. E-mail: yasminpratiwi04@gmail.com[1]; isnafia@apps.ipb.ac.id[2]; msriduresta@apps.ipb.ac.id[3]
*Corresponding Author: isnafia@apps.ipb.ac.id

Received: September 8, 2022
Accepted: January 25, 2023
Published: June 30, 2023

DOI:https//doi.org/10.22452/mjs.vol42no2.3

the experiment was designed. The research aimed to determine the optimal formulation of the fermented whey mask with added honey and red fruit extracts, focusing on its physical characteristics and antioxidant properties.

2. Materials and Methods

2.1 Time and Location

This research was carried out from August to December 2021 at the Integrated Laboratory of the Department of Animal Production Science and Technology, Faculty of Animal Science, IPB University, Indonesia.

2.2 Materials

The equipment utilized in this study included a hot plate with a magnetic stirrer, a porcelain dish, a thermometer, a UV-Vis 01601 spectrophotometer, a water bath, an analytical balance, a pH meter, an aw meter, a watch glass, and a beaker glass. The materials used in the study were categorized into three parts. For the production of fermented whey, the materials included fresh Etawa crossbreed goat's milk, vegetable rennet, citric acid, and lactic acid bacteria (*L. plantarum* IIA-1A5 and *L. bulgaricus*). The active ingredients used in the study were honey and red fruit extract. The ingredients for the mask preparations included rice flour, hydroxypropyl methylcellulose (HPMC), carbomer, polyvinyl alcohol propylene glycol, ethanol, glycerin, and triethanolamine. Other materials used for the antioxidant analysis were methanol, ascorbic acid, 2.2-*diphenyl-1-picrylhydrazyl* (DPPH), and distilled water.

2.3 Research Procedure

2.3.1 The Manufacture of Fermented Whey

The goat's milk was pasteurized at a temperature of 62°C-65°C for 30 minutes and then allowed to cool to a temperature of 30°C-35°C. Rennet was subsequently inoculated into the milk at a concentration of 0.25 g L-1, followed by 100 mL of citric acid. The milk was then left to coagulate for 60-120 minutes, forming a curd and producing a whey liquid. The whey was separated and stored at a temperature of 4°C-18°C for later inoculation with lactic acid bacteria. The whey was inoculated with a 2.5% starter culture of *L. bulgaricus* and *L. plantarum*, then homogenized and incubated at 37°C for 24 hours to produce fermented whey (Rahman *et al.*, 2014). The fermented whey was subsequently stored at a temperature of 4°C-10°C for further use in the mask formulation.

2.3.2 Mask Formulation

Fatmawati *et al.* (2020) introduced a novel method for the production of face masks. The mask is composed of a blend of whey, honey, red fruit extract, rice flour, carbomer, hydroxypropyl methylcellulose, polyvinyl alcohol, propylene glycol and ethanol, glycerin, and triethanolamine. As shown in Table 1, the mask formulation was divided into eight treatments. These included F1, which served as the control, F2 which consisted of whey and *L. plantarum*, F3 which was made up of whey and *L. bulgaricus*, and F4 which included whey, *L. plantarum*, and *L. bulgaricus*.

Table 1. Fermented whey mask formulation

Materials (%)	**Treatments (%)**							
	Honey 5%				**Honey 10%**			
	F1	**F2**	**F3**	**F4**	**F1**	**F2**	**F3**	**F4**
Fermented whey	32	32	32	32	27	27	27	27
Honey	5	5	5	5	10	10	10	10
Redfruit extract	2	2	2	2	2	2	2	2
Rice powder	35	35	35	35	35	35	35	35
PG+ethanol	6	6	6	6	6	6	6	6
Glycerin	5	5	5	5	5	5	5	5
HPMC	5	5	5	5	5	5	5	5
Karbomer	1	1	1	1	1	1	1	1
PVA	2	2	2	2	2	2	2	2
TEA	1	1	1	1	1	1	1	1
Total	100	100	100	100	100	100	100	100

2.3.3 pH value

A total of 5 grams of the sample was placed in a petri dish and measured with the digital pH meter Ionix Instruments pH5, calibrated at pH 4 and 7 according to SNI (1995) guidelines. The test was conducted three times (Trenggono and Latifah, 2013).

2.3.4 Water Activity

The determination of water activity was carried out using the Novasina LabSwift water activity tool. A 5g sample was inserted into the available container and left for approximately 2 minutes until the aw value was displayed. The test was conducted in a room with a controlled temperature of 25°C, maintained by an air conditioner, for three repetitions (Kingwatee *et al.*, 2015).

2.3.5 Dry Test Time

Approximately 1 gram of the mask sample was evenly applied to the back of the hand. The mask was then left to dry, and the time taken for the mask to dry and be ready for rinsing was observed. A suitable mask drying time of 10-20 minutes was used (Sunnah *et al.*, 2019).

2.3.6 Spreadability Test

A total of 5 grams of the sample was placed between two watch glasses and then subjected to a 100-gram load. The spreading power was calculated using the diameter of the spread after 1 minute of loading (Sunnah *et al.*, 2019).

DOI:https//doi.org/10.22452/mjs.vol42no2.3

2.3.7 Antioxidant

The free radical inhibitor technique of 1,1-diphenyl-2-picrylhydrazyl (DPPH) in methanol was used to test the antioxidant activity. A total of 1 mL of previously centrifuged sample liquid was reacted into a test solution of 0.5 mL DPPH with a concentration of 6 x 10^{-6} in a 2 mL vial. The mixture was then homogenized and incubated in a water bath for 30 minutes at 37°C. The absorbance wave length (λ) at 517 nm of the solution was then determined using spectrophotometry. The following formula was utilized to calculate the percentage of antioxidant activity:

$$\% \ inhibition = [\frac{Control - absorbance \ value}{Control}] \text{ x } 100$$

The antioxidant capacity was calculated by converting the inhibitory value to a standard curve. The antioxidant capacity was measured in milligrams of vitamin C equivalent (VCE) per 100 mL. Vitamin C standard curves were created by adjusting % antioxidant activity against DPPH inhibition for the following vitamin C concentrations: 0, 0.5, 1, 1.5, and 2 mg/100 mL distilled water (Shori and Baba, 2013).

2.4 Data Analysis Method

The statistical analysis employed in this study was a Completely Randomized Design (CRD) with one factor with Minitab as a statistical tool, namely, the concentration of honey addition with two levels: 5%, and 10%. This study comprised threedata replicationsd, namely, the pH, a_W, dispersion, dry time, and antioxidant activity values. The following mathematical model was employed (Mattjik and Sumertajaya 2002):

$$Y_{ijk} = u + A_i + B_j + ABij + \varepsilon_{ijk}$$

where:

Yijk : Observation of physical and antioxidant properties of masks observed with the ith honey level (i = F1, F2, F3, and F4)
U : General average
Ai : Effect of physical and antioxidant properties of masks at 5% level of honey
Bj : Effect of physical and antioxidant properties of masks at 10% level of honey
ABij : Interaction on the addition of 5% honey, the addition of 10% honey, and the k^{th} repetition
E_{ijk} : Error on the addition of 5% honey, the addition of 10% honey, and the k^{th} repetition

3. Results and Discussions

3.1 Fermented Whey Mask pH Value

Based on the results obtained, the fermented goat's milk mask with honey and red fruit has the pH values shown in Table 2. According to SNI 16-4399-1996, the pH value of a facial skin product ranges from 4.5 to 7.5.

Table 2. Results of pH mask test

Treatment	Treatment Level	
	5%	10%
F1	7.40 ± 0.05^a	7.48 ± 0.07^a
F2	5.73 ± 0.26^d	6.71 ± 0.24^{cd}
F3	7.05 ± 0.23^b	6.93 ± 0.02^c
F4	7.17 ± 0.02^{ab}	7.29 ± 0.02^{ab}

(F1; control, F2; fermented whey+*L. plantarum*, F3; fermented whey+*L. bulgaricus*, F4; fermented whey+*L. plantarum*+*L. bulgaricus*)

^{a} means with different superscript are significantly different (P<0.05)

According to SNI 16-4399-1996 (BSN, 1996), the acceptable pH range for a facial skin product is between 4.5 and 7.5. The pH test results in Table 3 show values ranging from 5.3 to 7.4, indicating that fermented whey masks could be safe for use on facial skin. The pH value in the test, with either the addition of 5% or 10% honey, produced significantly different values. Based on the data obtained, the control treatment (F1) had the highest pH value compared to the other treatments. This pH value is still suitable for external skin use because a pH that is too high can cause the skin to become dry and scaly, while a pH that is too low can lead to skin irritation (Rahmawanty *et al.*, 2015).

The concentration of honey added to the fermented whey mask influences the pH value because honey contains oligosaccharide carbohydrates. Lactic acid bacteria utilize carbohydratescteria during the fermentation process. The lactic acid produced from this metabolism can reduce the pH value and increase acidity. This finding aligns with research by Baguna *et al.* (2020), which suggests that using more than 5% honey will yield a product with a pH value below 6. The addition of another ingredient, carbomer, which is presumed to be a gelling agent with a neutral pH value, results in a product with a neutral pH value (Dewi and Saptarini, 2016).

3.2 Fermented Whey Mask Water Activity Value

The higher the water activity, the more microorganisms can grow, which can impact the shelf life of a product (Herawati, 2008). The minimum value of a product that has the potential to support the growth of gram-positive bacteria is 0.9 (Setyawardani and Sumarmono, 2015). The results of the water activity test on the face mask, as shown in Table 3, indicate that the control mask and the masks with varying levels of honey did not produce a water activity value that had a significant effect.

The water content in products containing honey is typically around 20-30%. Lactic acid bacteria also contribute to the production of metabolites such as organic acids, hydrogen peroxide, diacetyl, and bacteriocins. Bacteriocins have the ability to maintain the water content of the environment, making them suitable for use as natural preservatives in food products (Arifin *et al.*, 2021). Phenolic compounds in honey have a positive correlation with other compounds from lactic acid bacteria, resulting in low water activity (Angioi *et al.*, 2021).

Table 3. Water activity test results (a_w)

Treatment	Treatment Level	
	5%	10%
F1	0.757 ± 0,027^{abc}	0.751 ± 0.026^{abc}
F2	0.807 ± 0.022^{ab}	0.700 ± 0.052^{bc}
F3	0.739 ± 0.029^{bc}	0.725 ± 0.044^{bc}
F4	0.846 ± 0.011^{a}	0.670 ± 0.038^{c}

(F1; control, F2; whey+*L. plantarum*, F3; whey+*L. bulgaricus*, F4; whey+*L. plantarum*+*L. bulgaricus*)

^{a} means with different superscript are significantly different (P<0.05)

3.3 Spreading Ability Test

The mask's ability to be easily smeared and spread on the skin surface is significantly influenced by the effectiveness of the raw materials used. The diameter obtained in the spreadability test impacts the ease of mask application (Puspitasari *et al.*, 2018). As shown in Table 4, the mask formulation with 5% honey produced a smaller diameter than the mask with 10% honey. This result is directly proportional to the outcomes of the water activity test, where the mask formulation with 10% honey content produced a smaller water activity value.

Table 4. Spreadability test results of the fermented whey masks

Treatment	Treatment Level	
	5%	10%
F1	4.23 ± 0.25^{b}	4.73 ± 0.15^{ab}
F2	4.53 ± 0.25^{b}	5.20 ± 0.10^{a}
F3	4.47 ± 0.15^{b}	5.17 ± 0.21^{a}
F4	4.60 ± 0.26^{ab}	4.47 ± 0.25^{b}

(F1; control, F2; fermented whey+*L. plantarum*, F3; fermented whey+*L. bulgaricus*, F4; fermented whey+*L. plantarum*+*L. bulgaricus*)

^{a} means with different superscript are significantly different (P<0.05)

Honey is known to contain high levels of glucose and fructose, which can form a hydrogen bridge with water (Hadi *et al.*, 2016). Additionally, the polyphenols in honey contain hydroxyl groups that can enhance humectant properties. The interaction of other ingredients, such as glycerin and triethanolamine, also contributes to the hygroscopic nature of the mask. Furthermore, carbomers have gelling properties that help maintain viscosity (Sunnah *et al.*, 2019). The standard diameter for the mask spreadability test is between 5 and 7 cm (Garg *et al.*, 2002).

3.4 Dry Time Test

The dry time for mask preparation based on Budiman *et al.,* (2017) ranged from 15-30 minutes. This is following the observations of the length of time the fermented whey mask dries in Table 5.

Table 5. Drying time for fermented whey mask

Treatment	Treatment Level	
	5%	10%
F1	12.67 ± 0.83^{b}	15.40 ± 0.10^{a}
F2	15.30 ± 0.70^{a}	13.67 ± 0.76^{ab}
F3	13.23 ± 1.12^{b}	12.57 ± 0.57^{b}
F4	13.83 ± 0.40^{ab}	12.43 ± 0.71^{b}

(F1; control, F2; fermented whey+*L. plantarum*, F3; fermented whey+*L. bulgaricus*, F4; fermented whey+*L. plantarum*+*L. bulgaricus*)

^{a} means with different superscript are significantly different (P<0.05)

Fermented whey masks with 5% and 10% honey treatment levels did not show significant differences in results. Both had a drying time range from 12 to 15 minutes. This is due to the interaction of honey with other ingredients, such as polyvinyl alcohol (PVA). Polyvinyl alcohol is a semi-crystalline and biodegradable synthetic polymer that functions to form an occlusive film, adhesive, and provides resistance to oil and solvents (Beringhs *et al.*, 2013). In small amounts, polyvinyl alcohol (PVA) can be used as an emulsifier for cosmetics, especially masks (Rowe *et al.*, 2009). The use of PVA in fermented whey masks amounted to 2% of the total preparation, allowing the mask to have a longer drying time than PVA above 10% (Sunnah *et al.*, 2019). However, this is still within the effective and expected drying time range, and can provide sufficient time to moisturize the skin.

3.5 Antioxidant Activity Value

Antioxidant activity was measured to assess fermented whey's ability with honey and red fruit to ward off free radicals. In this study, natural ingredients were used in the manufacture of masks to produce antioxidant values, which are available in Table 6.

Table 6. Value of antioxidant activity

Treatment Level	Treatment	% Value of DPPH Inhibition	Antioxidant Capacity
5%	F1	28.348 ± 0.179^{f}	44.814 ± 0.005^{f}
	F2	40.094 ± 0.326^{d}	62.700 ± 0.008^{d}
	F3	45.860 ± 0.503^{b}	71.478 ± 0.013^{b}
	F4	44.157 ± 0.505^{c}	68.886 ± 0.013^{c}
10%	F1	40.295 ± 0.861^{d}	63.005 ± 0.022^{d}
	F2	33.699 ± 0.506^{e}	52.961 ± 0.013^{e}
	F3	44.731 ± 0.025^{bc}	69.760 ± 0.001^{bc}
	F4	47.783 ± 0.083^{a}	74.407 ± 0.002^{a}

(F1; control, F2; fermented whey+*L. plantarum*, F3; fermented whey+*L. bulgaricus*, F4; fermented whey+*L. plantarum*+*L. bulgaricus*)

^{a} means with different superscript are significantly different (P<0.05)

Based on statistical tests, the use of fermented whey, honey, and red fruit extract in mask preparations resulted in no significant differences. The variation in antioxidant activity in the mask is due to the differing concentrations of honey added. The addition of 5% honey to the control resulted in the lowest percentage inhibition and antioxidant capacity values. Low antioxidant concentrations indicated high antioxidant activity (Purba *et al.*, 2018). Honey contains flavonoids, amino acids, and vitamins that work synergistically to protect normal cells and neutralize free radicals (Cahyaningrum 2019).

The addition of 5% or 10%,of honey to whey fermented by lactic acid bacteria, This can occur because during the fermentation process, bacterial activity produces a higher acid value than the total amount of phenols and flavonoids (Purba *et al.*, 2018). Additionally, the inclusion of red fruit extract can also affect the rate of oxidation because it contains unsaturated fatty acids such as oleic and linoleic (Ayomi 2015), which can reduce the mask's ability to ward off free radicals.

4. Conclusion

The optimal formulation for a fermented whey mask involves the use of *Lactobacillus bulgaricus* bacteria, which has a superior ability to grow in whey as it utilizes whey as a nutrient source for its growth, and the addition of 10% honey. This conclusion is based on tests of the pH value, which aligns with the skin's natural pH, a water activity value below 0.9, high spreadability, an effective drying time, and an antioxidant inhibition percentage ranging from 33-47%.

6. References

Angioi R, Morrin A, White B. 2021. The rediscovery of honey for skin repair: recent advances in mechanisms for honey-mediated wound healing and scaffolded application techniques. *Applied Sciences* 11 (5192): 1-27.

Arifin M, Budiman C, FUJIYAMA K, Arief IIA. 2021. Kinetic and thermodynamic study of plantaricin IIA-1A5, a bacteriocin produced by Indonesian probiotic Lactobacillus plantarum IIA-1A5. *Protein and Peptide Letter* 28 (6): 680-686.

Ayomi AFM. 2015. Buah merah (*Pandanus conoideus*) terhadap penyerapan zat besi (Fe) dalam duodenum. *J Agromed Unila*. 2(2): 90-93.

[BSN] Badan Standarisasi Nasional. 1996. SNI pH Kulit 16-4399-1996. Jakarta (ID): Badan Standarisasi Nasional

Baguna R, Yelnetty A, Siswosubroto SE, Lontaan N. 2020. Pengaruh penggunaan Honey terhadap nilai pH, sineresis, dan total bakteri asam laktat yoghurt sinbiotik. *Zootec* 40(1): 214-222

Beringhs AO, Rosa JM, Stulzer HK, Budal RM, Sonaglio D. 2013. Green Clay and Aloe Vera Peel-Off Facial Masks: Response Surface Methodology Applied to the Formulation Design. *AAPS Pharmacy Science Technology 14*(1): 445–455.

Budiman A, Kusuma A, Aulifa D. 2017. *Peel-off* gel formulation from black mulberries (*Morus nigra*) extract. *National Journal of Physiology, Pharmacy and Pharmacology*, *7*(9).

Cahyaningrum PL. 2019. Aktivitas antioksidan Honey ternakan dan Honey kelengkeng sebagai pengobatan alami. *E-Jurnal Widya Kesehatan* 1(1): 1-6

Chang TS. 2009. An updated review of tyrosine inhibitors. *International Journal of Molecular Science* 10: 2440-2475

Codex. 1995. Whey powders. Codex STAN 289-1995.

Desniar, Rusmana I, Suwanto A, Mubarik NR. 2012. Senyawa antimikroba yang dihasilkan oleh bakteri asam laktat asal bekasam. *Jurnal Akuatika* 3(2): 135- 145.

Dewi CC, Saptarini NM. 2016. Review Artikel: Hidroksi Propil Metil Selulosa dan Karbomer Serta Sifat Fisikokimianya Sebagai Gelling Agent. *Jurnal Farmaka* (14): 1-10

Dewi LF, Sartini, Rahmiati. 2019. Isolasi bakteri asam laktat dari usus sapi (Bos taurus) serta kemampuannya dalam menghambat pertumbuhan bakteri Escherichia coli dan Shigella sp. *Jurnal Ilmiah Biologi UMA* 1(1): 21-27

DOI:https//doi.org/10.22452/mjs.vol42no2.3

Edwards PJB, Jameson GB. 2020. Structure and stability of whey protein. *Milk Proteins (2nd ed) Food Science and Technology*: 201-242

Fatmawati F, Santoso R, Azhar DP, Desvita NA, Fauziah R. 2020. Uji penghambatan tirosinase masker gel peel off yang mengandung rumput laut (Euchema cotonii) dan whey kefir. *Indonesia Natural Research Pharmaceutical Journal* 5(1): 94-104.

Garg A, Aggarwal D, Garg S, Sigla AK. 2002. Spreading of Semisolid Formulation. *Pharmaceutical Technology North America* 26(9): 84-105

Hadi H, Omar SSS, Awadh AI. 2016. A review: Honey, a gift from nature to health and beauty. *British Journal of Pharmacy* (1): 46-54

Halim CN, Zubaidah E. 2013. Studi kemampuan probiotik isolat bakteri asam laktat penghasil eksopolisakarida tinggi asal sawi asin (Brassica juncea). *Jurnal Pangan dan Agroindustri* 1(1): 129-137

Herawati H. 2008. Penentuan umur simpan produk pangan. Jurnal Litbang Pertanian 27(4): 124-130

Ichihashi M, Ando H, Yoshida M, Niki Y, Matsui M. 2009. Review article: photoaging of the skin. *Anti-aging Medicine* 6(6): 46-59

Kingwatee N, Apichartsrangkoon A, Chaikham P, Worametrachanon S, Techarung J, Pankasemsuk T. 2014. Spray drying Lactobacillus casei 01 in lychee juice varied carrier materials. *Food Science and Technology*: 1-7.

Mattjik AA, Sumertajaya M. 2002. *Perancangan Percobaan dengan Aplikasi Minitab.* Ed ke-2. Bogor (ID): IPB Pr.

Murtiningrum, Sarungallo ZL, Mawikere NL. 2012. The exploration and diversity of red fruit (*Pandanus conoideus L.*) from Papua based on its physical characteristics and chemical composition. *Biodiversitas* 13(3): 124-129

Nadhilla NF. 2014. The activity of antibacterial agent of honey against Staphylococcus aureus. *Journal Majority* 3(7): 94-101

Purba AP, Dwiloka B, Rizqiati H. 2018. Pengaruh lama fermentasi terhadap bakteri asam laktat (BAL), viskositas, aktivitas antioksidan, dan organoleptik *water kefir* anggur merah (*Vitis vinifera L.*). *Jurnal Teknologi Pangan* 2(1): 49-51.

Puspitasari AD, Mulangsri DAK, Herlina. 2018. Formulasi krim tabir surya ekstrak etanol daun kersen (*Muntingia calabura L.*) untuk kesehatan kulit. *Media Litbangkes* 28(4): 263-270.

Rahman A, Taufik E, Purwantiningasih S, Purwanto BP. 2014. Kajian potensi whey yoghurt sebagai bahan alami pencegah jerawat. *Jurnal Ilmu Produksi dan Teknologi Hasil Peternakan* 2(1): 238-242

Rahmawanty D, Yulianti N, Fitriana M. 2015. Konsentrasi Gelatin Dan Gliserin Formulation and Evaluation Peel-Off Facial Mask Containing Quercetin with Variation Concentration of Gelatin and Gliserin. *Media Farmasi*, *12*(1), 17–32.

Rio YPB, Djamal A, Asterina. 2012. Perbandingan efek antibakteri madu asli Sikabu dengan madu Lubuk Minturun terhadap Escherichia coli dan Staphylococcus aureus secara in vitro. *Jurnal Kesehatan Andalas* 1(2): 59- 62

Rowe RC, Sheskey PJ, Quinn ME. 2009. *Handbook of Pharmaceutical Exipients* (Sixth). London (UK): Pharmaceutical Pr.

Sabry EY. 2009. A three-stage strategy in treating acne vulgaris in patients with atopic dermatitis: a pilot study. *Journal of Pakistan Association of Dermatologist* (19): 95-105

Setyawardani T, Sumarmono J. 2015. Chemical and microbiological characteristics of goat milk kefir during Storage under different temperatures. Journal of the Indonesian Tropical Animal Agriculture 40(3): 183-188

Shori AB, Baba AS. 2013. Antioxidant activity and inhibition of key enzymes linked to type-2 diabetes and hypertension by *Azadirachta indica*-yogurt. *Journal of Saudi Chemical Society* (17): 295-301.

Sinulingga EH, Budiastuti A, Widodo A. 2018. Efektivitas Honey dalam formulasi pelembab pada kulit kering. Jurnal Kedokteran Diponegoro 7(1): 146-157

Sunnah I, Erwiyanti AR, Pratama NM, Yunisa KO. 2019. Efektivitas komposisi polivynil alkohol, propilenglikol, dan karbomer terhadap optimasi masker gel peel-off nano ekstrak daging buah labu kuning (*Cucurbita maxima D*). *Journal of Pharmaceutical Science and Clinical Research* (2): 82-94.

Trenggono RI, Latifah F. 2013. Buku Pegangan Ilmu Pengetahuan Kosmetik. Jakarta (ID): Gramedia.

Tyas DR, 2018. Pengaruh penambahan tepung kulit buah naga merah (Hylocereus polyrhiud) terhadap sifat fisik masker wajah berbahan dasar tepung kefir susu sapi untuk anti-aging. *Jurnal Tata Rias* 7(3): 32-40

Vallianou NG, Gounari P, Skourtis A, Panagos J, Kazazis C. 2014. Honey and its anti-inflammatory, antibacterial, and antioxidant properties. *General Medicine Journal* 2(2): 1-5

DOI:https//doi.org/10.22452/mjs.vol42no2.3

MALAYSIAN JOURNAL OF SCIENCE
MJS
ISSN 1394-3065

Regular Issue

Malaysian Journal of Science 42 (2): 22-32 (June 2023) https://mjs.um.edu.my

SLOW AND FAST SUBSYSTEMS FOR COMPLEX UNCOMPETITIVE INHIBITOR MECHANISMS

Honar J. Hamad[1a], Sarbaz H. A. Khoshnaw[2b]*, Muhammad Shahzad[3c]

Abstract: To fully understand intricate enzyme reaction models, one must explore beyond the confines of chemical and biological tools and look toward mathematical modeling and model reduction techniques. Mathematical modeling and model reduction techniques have the potential to provide a vast array of analysis tools for such models. This piece of work entails a review and discussion of a complex noncompetitive inhibitor model. This model is composed of seven non-linear differential equations with constant rates. We propose two efficient model reduction techniques: quasi- steady-state approximation (QSSA) and quasi-equilibrium approximation (QEA). By utilizing the suggested methods, the model equations are segregated into slow and fast subsystems, leading to the attainment of reduced models and slow manifolds with fewer variables and parameters. The outcomes manifest some analytical approximate solutions for the proposed model and establish a profound agreement between model dynamics for both the original and the reduced models. Observing that the reduced models can accurately identify certain critical model parameters is intriguing.

Keywords: *Mathematical modeling, enzymatic reactions, slow and fast sub- systems, model reductions*

1. Introduction

A molecule that hinders the activity of an enzyme is referred to as an enzyme inhibitor. An enzyme is a protein molecule that catalyzes biological reactions. These molecules can function as activators or inhibitors, regulating numerous biological processes. Enzymes interact with substrates to produce products. Enzyme inhibition can be categorized into two types: reversible and irreversible inhibitors. The three types of reversible enzyme inhibition are competitive, noncompetitive, and uncompetitive [1].

Mathematical modeling is an essential tool in the scientific method, where mathematical statements (or models) are used to create hypotheses and predictions. Several classical works have investigated models of biochemistry differential equation systems. Authors have sought models for biochemical reaction networks, such as model reductions, quasi-equilibrium manifold approximations, total quasi-steady- state approximations, model reductions in chemical dynamics, slow invariant manifolds, singular perturbations, thermodynamic estimates, and reaction graph analysis. Additionally, mathematical modeling techniques have been applied to enzyme inhibitors with slow and fast subsystems [2–7].

Various mathematical models exist, including dynamical systems, statistical models, and differential equations. The conversion of a concept to a theoretical model and then a quantitative model can be achieved in multiple ways. A theoretical model is a visual representation of the concept using boxes and arrows in a model diagram. The concept of chemical kinetics modeling is utilized to convert physical reality into a mathematical description. Real-world problems can also be expressed using mathematical equations [8–18].

In systems biology, a mathematical model is an intellectual tool used to describe and analyze models. Chemical reactions are often complex, and the fundamental characteristics of the reaction mechanism must be known to simplify the complexity of a complex reaction. Model reduction techniques are necessary to create such models. The first theories of complex chemical reactions coincided with the development of model reduction approaches. Model reduction involves transforming one system into another with fewer variables and parameters. Quasi-steady-state approximation (QSSA) and quasi-equilibrium approximation (QEA) are two useful approximation tools in the study of biochemical kinetics. These methods are focused on nonlinear differential equation systems, where one or more dependent variables can be considered in a steady state with respect to the instantaneous values of the other dependent variables following an initial fast transient [9, 20].

Authors information:
[a]Department of Mathematics, Soran University, Soran, Kurdistan Region of IRAQ. E-mail: honar.Hamad@soran.edu.iq[1];
[b]Department of Mathematics, University of Raparin Ranya, Kurdistan Region of IRAQ. Email: sarbaz.hamza@uor.edu.krd[2]
[c]Department of Mathematics and Statistics, The University of Haripur, Haripur, PAKISTAN. Email: shahzadmaths@uoh.edu.pk[3]
*Corresponding Author: sarbaz.hamza@uor.edu.krd

Received: February 23, 2022
Accepted: November 8, 2022
Published: June 30, 2023

DOI:https//doi.org/10.22452/mjs.vol42no2.4

The written work comprises several valuable contributions. Firstly, we delve into and examine a multifaceted model of uncompetitive inhibitor reactions, which is comprised of seven nonlinear differential equations featuring constant rates. We then proceed to employ two efficacious techniques for model reduction, namely the quasi- steady-state approximation (QSSA) and quasi-equilibrium approximation (QEA). Furthermore, we have made another significant contribution by dividing the model equations into slow and fast subsystems. Additionally, the original model equations can be suitably abridged, leading to the acquisition of slow manifolds with a fewer number of variables and parameters. Ultimately, we identify certain critical parameters of the model based on the reduced models that can help facilitate further research and enhancements.

2. Chemical Reaction Kinetics

One of the most significant technique theories for modeling is the concept of chemical kinetic theory. Model states, parameters, and equations are significant assumptions for building such models. This is because it helps to examine mathematical modeling effectively and conveniently. The generally reversible chemical reaction equations can be expressed as follow:

$$\sum_{i=1}^{n} a_i A_i \underset{k_j^b}{\overset{k_j^f}{\rightleftharpoons}} \sum_{i=1}^{n} b_i B_i , \qquad (1)$$

where k_j^f and k_j^b are chemical reaction constants, the real numbers a_i and b_i stand for the stoichiometric coefficients of the corresponding species (reactants and products), species A_i and B_i are the i^{th} reactant or product. Let R^b and R^f are denoted for backward and forward rates respectively then the reaction speed of each elementary step R_j for $j = 1, 2, \dots, m$ can be expressed as follows:

$$W_j = R_j^f - R_j^b \, . \qquad (2)$$

Using mass action law, the reaction rates for equation 1 are given below:

$$R_j^f = k_j^f \prod C_{Ai}^{ai}$$

$$R_j^b = k_j^b \prod C_{Bi}^{bi},$$

where A_i and B_i are the reactants and products species and their concentration are C_{Ai}, C_{Bi}. Finally, the model of kinetic differential equations with constant rates are expressed below:

$$\frac{dc}{dt} = \sum_{j=1}^{m} \gamma_j \, W_j(C), \qquad (3)$$

where $\gamma_j = b_{ij} - a_{ij}$ for $i = 1, 2, \dots, n$ and $j = 1, 2, \dots, m$ are stoichiometric vectors.

3. Model Reduction Techniques

Model reduction techniques in systems of complex chemical reactions are employed to simplify the mathematical representation of the reaction network while preserving the essential behavior of the system. These techniques aim to reduce computational complexity and facilitate analysis and simulation of the chemical kinetics. Here are some commonly used models' reduction techniques in systems of complex chemical reactions:

Quasi-Steady-State Approximation (QSSA): This technique assumes that certain species in the reaction network reach a quasi-steady state, meaning their concentrations change relatively slowly compared to other species. By applying the QSSA, the rate equations for these quasi-steady-state species can be simplified or eliminated, reducing the dimensionality of the system.

Partial Equilibrium Approximation: In systems with fast and slow reactions, the partial equilibrium approximation assumes that some reactions reach equilibrium much faster than others. By assuming rapid equilibration for these reactions, the equilibrium concentrations of the involved species can be calculated independently of the rest of the system, allowing for further simplification.

Species Lumping's: Species lumping involves grouping together similar or unimportant species into lumped species, reducing the total number of species in the system. This is often done based on chemical similarities or through the use of empirical grouping rules. Lumping reduces the dimensionality of the system and simplifies the reaction network.

Reaction Lumping's: Similarly, to species lumping, reaction lumping involves combining multiple elementary reactions into lumped reactions. This is typically done by identifying reactions with similar rate-controlling steps or by lumping re- actions that have negligible contributions to the overall system behavior. Reaction lumping reduces the number of reactions in the system and simplifies the kinetics.

Time-Scale Separation: If the reaction network exhibits distinct time scales, it may be possible to simplify the system by assuming that some reactions are much faster or slower compared to others. This allows for approximations such as assuming steady-state or equilibrium conditions for certain species or reactions, leading to a reduced model.

Principal Component Analysis (PCA): PCA is a statistical technique used to identify dominant modes of variation in a high-dimensional dataset. In the context of chemical kinetics, PCA can be employed to identify the most important reaction pathways or species in the system. By focusing on the dominant modes, a reduced model can be constructed that captures the essential behavior of the system.

These model reduction techniques are often combined or adapted based on the specific characteristics of the chemical system and the objectives of the analysis. The goal is to strike a balance between computational efficiency and accuracy, enabling the study and understanding of complex chemical kinetics in a more tractable manner. The art of reducing models in intricate chemical reaction systems is a widely recognized technique to decrease the quantity of constituents such as variables and parameters. Although simplified, the dynamics of these models should still exhibit a resemblance to their original counterparts. The categorization of model equations into their slow and rapid subsystems plays a pivotal role in elucidating the model dynamics [2, 21].

The objective of this endeavor is to partition the structure of intricate uncompetitive inhibitor mechanisms into sluggish and speedy subsystems through the implementation of the quasi-steady-state approximation (QSSA) and quasi-equilibrium approximation (QEA) techniques. Subsequently, the reduced models and slow manifolds are generated with a reduced number of parameters and variables. The approximated analytical solutions for the proposed model demonstrate an excellent correspondence between the model dynamics for both the original and the reduced models. The quasi-steady-state approximation technique has undergone numerous revisions over the course of the previous century. In the analysis of biochemical kinetics, the quasi-steady-state approximation technique is a vital approximation method that can be employed to categorize nonlinear models into slow and fast subsystems, as well as to derive some analytical approximation solutions [7, 9, 22]. Following this method, the variable set $C(t)$ is divided into two groups: the group of slow variables $C^S\ (t)$ and the group of fast variables $C^f\ (t)$. Then kinetic equation 3 can be split into slow and fast subsystems:

$$\frac{dC^s}{dt} = W^s(C^s(t), C^f(t), \kappa), \tag{4}$$

$$\frac{dC^f}{dt} = \frac{1}{\epsilon} W^f(C^s(t), C^f(t), \kappa), \tag{5}$$

where equations 4 and 5 are slow and fast subsystems respectively, C^s, C^f are groups of slow and fast variables (basics). Based on the Tikhonov theorem, the standard singular perturbation can be applied on the fast subsystem and we can analyze fast subsystem 5. The slow manifold occurs if we have a stable dynamic of fast variables under given values of slow concentrations [23, 26]. The attractive slow manifold of the system can be calculated from algebraic equation

$$W^f(C^s(t), C^f(t), \kappa) = 0,$$

when $\epsilon \rightarrow 0$. As a result, the new system has fewer variables (species concentration) and parameters (chemical reaction constants). The concept of quasi-equilibrium approximation (QEA) is an effective technique of model reduction to reduce the number of variables and parameters. According to this concept, fast reactions reach equilibrium very quickly compared to a set of slow reactions. We can write the initial system 3 as follows:

$$\frac{dc}{dt} = \sum_{s,slow} \gamma^s\, W^s(C,\kappa,t) + \frac{1}{\epsilon} \sum_{f,fast} \gamma^f\, W^f(C,\kappa,t), \tag{6}$$

where W^s and W^f are reaction rate functions, whereas γ^s and γ^f are stoichiometric vectors and ϵ is a small parameter. Then, the fast subsystem can be stated as:

$$\frac{dc}{dt} = \frac{1}{\epsilon} \sum_{f,fast} \gamma^f\, W^f(C,\kappa,t), \tag{7}$$

By using the algebraic equations $\sum_{f,fast} \gamma^f\, W^f(C,\kappa,t) = 0$, when $\epsilon \rightarrow 0$ we can calculate the quasi-equilibrium manifold μ_0. For further information about the approaches described and their use in biological and chemical models see [9, 24–26].

4. Reversible Uncompetitive Reaction Mechanisms

Uncompetitive inhibition occurs when an enzyme inhibitor binds only to the complex generated between the enzyme and the substrate. We can now derive a substrate inhibition equation. For substrate S, enzyme E has two binding sites which are a catalytic site that generates the product P and a non-catalytic site that produces the product at a slower rate. We can write the reaction scheme as follows [27]

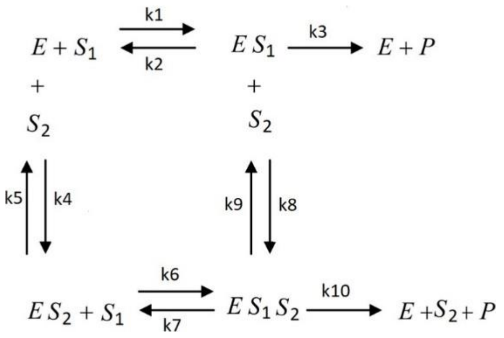

Figure 1. Chemical Reaction Networks for Uncompetitive Inhibitor Mechanisms.

The substrates bound to the catalytic and non-catalytic sites are denoted by ES1 and ES2, respectively, and two substrate molecules attached to both the catalytic and non-catalytic sites are denoted by ES1S2, and k_i for $i = 1, 2, \ldots, 10$ are model parameters. By taking the above assumptions, the mathematical model reactions and their reaction rates are shown below:

$$\begin{aligned}
&\boldsymbol{E + S_1 \underset{k_2}{\overset{k_1}{\rightleftharpoons}} ES_1 \overset{k_3}{\rightarrow} E + P},\\
&\boldsymbol{E + S_2 \underset{k_5}{\overset{k_4}{\rightleftharpoons}} ES_2},\\
&\boldsymbol{ES_2 + S_1 \underset{k_7}{\overset{k_6}{\rightleftharpoons}} ES_1S_2},\\
&\boldsymbol{ES_1 + S_2 \underset{k_9}{\overset{k_8}{\rightleftharpoons}} ES_1S_2},\\
&\boldsymbol{ES_1S_2 \overset{k_{10}}{\longrightarrow} E + S_2 + P}.
\end{aligned} \qquad (\mathbf{8})$$

Let concentrations of the reactants in 8 denoted by lowercase letters as:

$$s_1 = [S_1],\ s_2 = [S_2],\ e = [E],\quad c_1 = [ES_1],\quad c_2 = [ES_2],\quad c_3 = [ES_1S_2] \text{ and } p = [P],$$

where $[\,]$ denotes concentration and $k_i,\ i = 1, 2, \cdots, 10$ are called the rate constants.

Then the Law of Mass Action applied to 8 leads to one equation for each reactant and hence the system of nonlinear reaction equations,

$$\begin{aligned}
\frac{de}{dt} &= -k_1 e s_1 + (k_2 + k_3)c_1 - k_4 e s_2 + k_5 c_2 + k_{10} c_3\\
\frac{ds_1}{dt} &= -k_1 e s_1 + k_2 c_1 - k_6 s_1 c_2 + k_7 c_3\\
\frac{ds_2}{dt} &= -k_4 e s_2 + k_5 c_2 - k_8 c_1 s_2 + k_9 c_3 + k_{10} c_3\\
\frac{dc_1}{dt} &= k_1 e s_1 - k_2 c_1 - k_3 c_1 - k_8 s_2 c_1 + k_9 c_3\\
\frac{dc_2}{dt} &= k_1 e s_2 - k_5 c_2 - k_6 c_2 s_1 + k_7 c_3\\
\frac{dc_3}{dt} &= k_1 s_1 s_2 - k_7 c_3 + k_8 c_1 s_2 - k_9 c_3 - k_{10} c_3\\
\frac{dp}{dt} &= k_3 c_1 + k_{10} c_3
\end{aligned} \qquad (1)$$

The model initial conditions are $e(0) = e_0,\ s_1(0) = s_1^0,\ s_2(0) = s_2^0$ and

$c_1(0) = c_2(0) = c_3(0) = p\,(0) = 0$. Based on the proposed simple enzymatic reactions, there were a very important assumption that the total amount of enzyme is much smaller than the amount of substrate, $[E] \ll [S1]$. Therefore, we can define a very small parameter based on the given condition, $\epsilon = \frac{e_0}{s_1^0}$.

5. Quasi Steady State Approximation

The system 9 has the following conservation laws:

$$e + c_1 + c_2 + c_3 = e_0, \;\; s_2 + c_2 + c_3 = s_2^0, \;\; s_1 + c_1 + c_3 \;\; + p = s_1^0. \qquad (10)$$

By substituting the conservation laws 10 into the system 9, and we can eliminate the variables s_2, c_2 and p from the system 9, and then by introducing the following new variables:

$$\tau = k_1 e_0, \;\; u_1 = \frac{e}{e_0}, \;\; u_2 = \frac{s_1}{s_1^0}, \;\; w_1 = \frac{c_1}{e_0}, \;\;\; w_2 = \frac{c_3}{e_0}.$$

The system (9) takes the following form:

$$\frac{du_1}{d\tau}\epsilon = -u_1 u_2 + (\alpha_1 + \alpha_2)w_1 - \alpha_3 u_1\big(\alpha_4 - \epsilon(1 - u_1 - w_1)\big) + \alpha_5(1 - u_1 - w_1 - w_2) + \alpha_6 w_2, \qquad (11a)$$

$$\frac{du_2}{d\tau} = -u_1 u_2 + \alpha_1 w_1 - \alpha_7 u_2(1 - u_1 - w_1 - w_2) \; + \alpha_8 w_2\,, \qquad (11b)$$

$$\frac{dw_1}{d\tau}\epsilon_1 = u_1 u_2 + \alpha_1 w_1 - \alpha_2 w_1 - \alpha_9 w_1\,(\alpha_4 - \epsilon_1 + \epsilon_1 u_1 + \epsilon_1 w_1) + \alpha_{10} w_2, \qquad (11c)$$

$$\frac{dw_2}{d\tau}\epsilon_1 = \alpha_7 u_2(1 - u_1 - w_1 - w_2) - \alpha_8 w_2 + \alpha_9 w_1(\alpha_4 - \epsilon_1 + \epsilon_1 u_1 + \epsilon_1 w_1) - \alpha_{10} w_2 - \alpha_6 w_2, \qquad (11d)$$

where

$$\alpha_1 = \frac{k_2}{k_1 s_1^0}, \;\; \alpha_2 = \frac{k_3}{k_1 s_1^0}, \;\; \alpha_3 = \frac{k_4}{k_1}, \;\; \alpha_4 = \frac{s_2^0}{s_1^0}, \;\; \alpha_5 = \frac{k_5}{k_1 s_1^0}, \;\; \alpha_6 = \frac{k_{10}}{k_1 s_1^0}, \;\; \alpha_7 = \frac{k_6}{k_1}, \;\; \alpha_8 = \frac{k_7}{k_1 s_1^0}, \;\; \alpha_9 = \frac{k_8}{k_1}, \;\; \alpha_{10} = \frac{k_9}{k_1 s_1^0},$$

with initial conditions $u_1(0) = 1, u_2(0) \; = 1$ and $w_1(0) = w_2(0) = 0.$ Equation $11b$ is the slow form while equations $11a, 11c$ and $11d$ are fast. Now by using quasi steady-state approximation (QSSA) when $\epsilon_1 \; \rightarrow \; 0$, then sub-equations $11a,\; 11b, 11c$ and $11d$ take the form:

$$0 = -u_1 u_2 + (\alpha_1 + \alpha_2)w_1 - \alpha_3 u_1 \alpha_4 + \alpha_5(1 - u_1 - w_1 - w_2) + \alpha_6 w_2, \qquad (12a)$$

$$0 = u_1 u_2 + \alpha_1 w_1 - \alpha_2 w_1 - \alpha_9 \alpha_4 w_1 \; + \alpha_{10} w_2, \qquad (12b)$$

$$0 = \alpha_7 u_2(1 - u_1 - w_1 - w_2) - \alpha_8 w_2 + \alpha_9 \alpha_4 w_1 - \alpha_{10} w_2 - \alpha_6 w_2, \qquad (12c)$$

$$\frac{du_2}{d\tau} = -u_1 u_2 + \alpha_1 w_1 - \alpha_7 u_2(1 - u_1 - w_1 - w_2) \; + \alpha_8. \qquad (12d)$$

After solving equations $12a$,$12b$ and $12c$ for u_1, w1 and w_2 in terms of u_2:

$$u_1 = \frac{\beta_1 + \beta_2 + \beta_3 u_2}{\beta_1 + \beta_6 + (\beta_3 + \beta_4 + \beta_8 + \beta_{10})u_2 + (\beta_5 + \beta_9)u_2^2}$$

$$w_1 = \frac{u2(\beta 4 \;+\; \beta 5 u2)}{\beta_1 + \beta_6 + (\beta_3 + \beta_4 + \beta_8 + \beta_{10})u_2 + (\beta_5 + \beta_9)u_2^2} \qquad (13)$$

$$w_2 = \frac{u2(\beta 8 \;+\; \beta 9 u2)}{\beta_1 + \beta_6 + (\beta_3 + \beta_4 + \beta_8 + \beta_{10})u_2 + (\beta_5 + \beta_9)u_2^2}$$

DOI:https//doi.org/10.22452/mjs.vol42no2.4

where

$\beta_1 = \alpha_5(\alpha_1\alpha_6 + \alpha_2\alpha_6 + \alpha_1\alpha_8 + \alpha_2\alpha_8 + \alpha_1\alpha_{10} + \alpha_2\alpha_{10}),$

$\beta_2 = \alpha_4\alpha_5(\alpha_6 + \alpha_8),$

$\beta_3 = \alpha_7\big(\alpha_6(\alpha_1 + \alpha_2 + \alpha_4\alpha_9) + \alpha_{10}(\alpha_1 + \alpha_2)\big),$

$\beta_4 = \alpha_5(\alpha_6 + \alpha_8 + \alpha_{10}) + \alpha_3\alpha_4\alpha_7\alpha_{10},$

$\beta_5 = \alpha_7(\alpha_6 + \alpha_{10}),$

$\beta_6 = \alpha_3\alpha_2\alpha_9(\alpha_6 + \alpha_9),$

$\beta_7 = \alpha_3\alpha_4\big(\alpha_6(\alpha_1 + \alpha_2)\alpha_8(\alpha_1 + \alpha_2)\alpha_{10}(\alpha_1 + \alpha_2) + \alpha_4\alpha_5\alpha_9(\alpha_6 + \alpha_8)\big),$

$\beta_8 = \alpha_4\alpha_9(\alpha_5 + \alpha_3\alpha_4\alpha_7) + \alpha_3\alpha_4\alpha_7(\alpha_1 + \alpha_2),$

$\beta_9 = \alpha_4\alpha_7\alpha_9,$

$\beta_{10} = \alpha_4\alpha_8\alpha_9.$

As a result, the approximate solution of the system 11 comes close enough to the manifold μ_0, which is defined as follows:

$$\mu_0 = \{(u_1, u_2, w_1, w_2): u_2 \in [0,1]\},$$

where

$$\begin{aligned} u_1 &= \frac{\beta_1 + \beta_2 + \beta_3 u_2}{\beta_1 + \beta_6 + (\beta_3 + \beta_4 + \beta_8 + \beta_{10})u_2 + (\beta_5 + \beta_9)u_2^2}, \\ w_1 &= \frac{u2(\beta_4 + \beta_5 u_2)}{\beta_1 + \beta_6 + (\beta_3 + \beta_4 + \beta_8 + \beta_{10})u_2 + (\beta_5 + \beta_9)u_2^2}, \\ w_2 &= \frac{u2(\beta_8 + \beta_9 u_2)}{\beta_1 + \beta_6 + (\beta_3 + \beta_4 + \beta_8 + \beta_{10})u_2 + (\beta_5 + \beta_9)u_2^2}, \end{aligned} \tag{14}$$

By substituting 13 into $12d$, we get the reduced differential equation below, which is close to the manifold μ_0.

$$\frac{du_2}{d\tau} = \frac{\rho_1 u_2 - \rho_2 u_2^2}{\rho_3 + \rho_4 u_2 + \rho_5 u_2^2},$$

where

$\rho_1 = \beta_2 - \beta_1 + \alpha_1\beta_4 + \alpha_7\beta_6 - \alpha_8\beta_8,$

$\rho_2 = \beta_3 - \alpha_1\beta_5 - \alpha_8\beta_9 + \alpha_7\beta_{10},$

$\rho_3 = \beta_1 + \beta_6,$

$\rho_4 = \beta_3 + \beta_4 + \beta_8 + \beta_{10}$

$\rho_5 = \beta_5 + \beta_9.$

6. Quasi Equilibrium Approximation

In order to simplify model equations and obtain some analytical solutions, we can use the second method defined as quasi-equilibrium approximation (QEA) for chemical reaction 8. We can take two separate assumptions for fast reactions, as shown below. For first assumption we suppose that the first reaction

$$E + S_1 \underset{k_2}{\overset{k_1}{\rightleftharpoons}} ES_1$$

becomes quasi-equilibrium when the equilibrium is fast i.e. the parameters can be taken as $k_1 = \frac{1}{\epsilon}k_1'$ and $k_2 = \frac{1}{\epsilon}k_2'$ where $\epsilon = \frac{e_0}{s_0}$ this means that $k_1' = \epsilon k_1$ and $k_2' = \epsilon k_2$. Then, the system 9 takes the following form:

$$\begin{gathered}
\frac{de}{dt} = -\frac{1}{\epsilon}H^f(e, s_1, c_1, t) + H_1^s(c_1, t) + H_2^s(e, s_2, c_2, t) + H_3^s(c_3, t), \\
\frac{ds_1}{dt} = -\frac{1}{\epsilon}H^f(e, s_1, c_1, t) + H_4^s(s_1, c_2, c_3, t), \\
\frac{ds_2}{dt} = H_2^s(e, s_2, c_2, t) + H_3^s(c_3, t) + H_5^s(s_2, c_1, , c_3, t), \\
\frac{dc_1}{dt} = \frac{1}{\epsilon}H^f(e, s_1, c_1, t) - H_1^s(c_1, t) + H_5^s(s_2, c_1, , c_3, t) \\
\frac{dc_2}{dt} = -H_2^s(e, s_2, c_2, t) + H_4^s(s_1, c_2, c_3, t), \\
\frac{dc_3}{dt} = - H_4^s(s_1, c_2, c_3, t) - H_5^s(s_2, c_1, , c_3, t) - H_3^s(c_3, t), \\
\frac{dp}{dt} = H_1^s(c_1, t) + H_3^s(c_3, t),
\end{gathered} \tag{15}$$

where

$H^f(e, s_1, c_1, t) = k_1' e s_1 - k_1' c_1$, $H_1^s(c_1, t) = k_3 c_1$,

$H_2^s(e, s_2, c_2, t) = -k_4 e s_2 + k_5 c_2$, $H_3^s(c_3, t) = -k_4 e s_2 + k_5 c_2$,

$H_4^s(s_1, c_2, c_3, t) = -k_6 s_1 c_2 + k_7 c_3$,

$H_5^s(s_2, c_1, c_3, t) = -k_8 c_1 s_2 + k_9 c_3$.

Now, we can apply the quasi-equilibrium approximation (QEA) when $\epsilon \to 0$. It's clear that the fast reaction involves three species, S, E, and ES, while other chemical reaction components are not considered in the quasi-equilibrium manifold (QEM) analysis. According to conservation laws of fast reactions, we obtain two slow variable which defined as:

$$\eta_1(e, c_1) = e + c_1, \quad \eta_2(s_1, c_1) = s_1 + c_1. \tag{16}$$

The slow variable η_1 is the total amount of enzyme and η_2 is the sum of the free substrate and the complex of enzyme–substrate. After solving the algebraic equation $H^f\,(e, s_1, c_1, t) = 0$ we can compute the slow manifold μ_0 for as follows:

$$\mu_0 = \left\{(e, s_1, c_1) \in \mathbb{R}^3 : s_1 = \frac{k_2' c_1}{k_1' e}\right\}. \tag{17}$$

After finding e and s1 from 16 then substituting into algebraic equation $H^f\,(e, s_1, c_1, t) = 0$, we get the following quadratic equation:

$$k_1' c_1^2 - (k_1'\eta_1 + k_1'\eta_2 + k_2')c_1 + k_1'\eta_1\eta_2 = 0. \tag{18}$$

Now, equation 18 can be solved for c_1 as follows:

$$\mathrm{c}_1(\eta_1, \eta_2) = \frac{1}{2}\left[(\eta_1 + \eta_2 + \frac{k_1'}{k_2'}) \pm \left(\left(\eta_1 + \eta_2 + \frac{k_1'}{k_2'}\right)^2 - 4\eta_1\eta_2\right)^{\frac{1}{2}}\right]. \tag{19}$$

The solution for *s* and *e* are

$$\mathrm{s}_1(\eta_1, \eta_2) = \eta_2 - \frac{1}{2}\left[\left(\eta_1 + \eta_2 + \frac{k_1'}{k_2'}\right) \pm \left(\left(\eta_1 + \eta_2 + \frac{k_1'}{k_2'}\right)^2 - 4\eta_1\eta_2\right)^{\frac{1}{2}}\right], \tag{20}$$

$$e(\eta_1, \eta_2) = \eta_1 - \frac{1}{2}\left[\left(\eta_1 + \eta_2 + \frac{k_1'}{k_2'}\right) \pm \left(\left(\eta_1 + \eta_2 + \frac{k_1'}{k_2'}\right)^2 - 4\eta_1\eta_2\right)^{\frac{1}{2}}\right]. \tag{21}$$

For the second assumption, we suppose that $E + S_1 \underset{k_2}{\overset{k_1}{\rightleftharpoons}} ES_1$ and $ES_2 + S_1 \underset{k_7}{\overset{k_6}{\rightleftharpoons}} ES_1S_2$ are only two fast reversible reactions in the model network become quasi-equilibrium when the equilibrium is fast. Let $k_1 = \frac{1}{\epsilon}k_1',\ k_2 = \frac{1}{\epsilon}k_2',\ k_6 = \frac{1}{\epsilon}k_6'$ and $k_7 = \frac{1}{\epsilon}k_7'$ where $\epsilon = \frac{e_0}{s_0}$ this means that $k_1' = \epsilon k_1, k_2' = \epsilon k_2, k_6' = \epsilon k_6$ and $k_7' = \epsilon k_7$.

Then, the system 9 takes the following form:

$$\begin{aligned}
\frac{de}{dt} &= -\frac{1}{\epsilon}H_1{}^f\,(e, s_1, c_1, t) + H_1^s(c_1, t) - \frac{1}{\epsilon}H_2^f(e, s_2, c_2, t) + H_2^s(c_3, t),\\
\frac{ds_1}{dt} &= -\frac{1}{\epsilon}H_2^f(e, s_2, c_2, t) - H_4^s(s_2, c_1, c_3, t) + H_2^s(c_3, t),\\
\frac{ds_2}{dt} &= -\frac{1}{\epsilon}H_2^f(e, s_2, c_2, t) + H_3^s(c_3, t) + H_5^s(\,s_2, c_1, , c_3, t),\\
\frac{dc_1}{dt} &= \frac{1}{\epsilon}H_1{}^f\,(e, s_1, c_1, t) - H_1^s(c_1, t) + H_4^s(\,s_2, c_1, , c_3, t),\\
\frac{dc_2}{dt} &= \frac{1}{\epsilon}H_2^f(e, s_2, c_2, t) - H_3^s(s_1, c_2, c_3, t),\\
\frac{dc_3}{dt} &= H_3^s(s_1, c_2, c_3, t) - H_4^s(\,s_2, c_1, , c_3, t) - H_1^s(c_1, t),\\
\frac{dp}{dt} &= H_1^s(c_1, t) + H_2^s(c_3, t),
\end{aligned} \tag{22}$$

where $H_1{}^f\,(e, s_1, c_1, t) = k_1' e s_1 - k_2' c_1,\ H_2^f(e, s_2, c_2, t) = k_4' e s_2 - k_5' c_2,$
$H_1^s(c_1, t) = k_3 c_1,\ H_2^s(c_3, t) = k_{10} c_3, H_3^s(s_1, c_2, c_3, t) = k_6 c_2 - k_7 c_3$ and
$H_4^s(\,s_2, c_1, , c_3, t) = k_8 s_2 c_1 - k_9 c_3.$

Now, we can apply the quasi-equilibrium approximation (QEA) when $\epsilon \to 0$. The fast reaction involves four species, E, S_1, S_2, ES_1, and ES_2, while other chemical reaction components are not considered in the quasi-equilibrium manifold (QEM) analysis. Hence, we obtain three slow variables $\eta_1(e, c_1, c_2) = e + c_1 + c_2$, $\eta_2(s_1, c_1) = s_1 + c_1$ and $\eta_3(s_2, c_2) = s_2 + c_2$. The slow manifold is determined after solving the algebraic equation $H_1^f(e, s_1, c_1, t) = 0$ and $H_2^f(e, s_2, c_2, t) = 0$:

$$\mu_0 = \left\{(e, s_1, c_1, c_2) \in \mathbb{R}^3 : s_1 = \frac{k_2' c_1}{k_1' e}, \quad s_2 = \frac{k_5' c_2}{k_4' e}\right\}. \tag{23}$$

By using an assumption that $[S_1] \gg [C_1]$ this means that $\eta_2 \gg C_1$, we get the following equation:

$$\begin{aligned} \left(1 + \frac{\eta_1}{\eta_2} + \frac{k_2'}{k_1'\eta_2}\right) c_1 + c_2 &= \eta_1 + O\left(\frac{c_1 c_2}{\eta_2}\right), \\ \left(\frac{\eta_3}{\eta_2} + \frac{\eta_1}{\eta_2} + \frac{k_5'}{k_4'\eta_2}\right) c_2 &= \frac{\eta_1\eta_3}{\eta_2} + O\left(\frac{c_1 c_2}{\eta_2}\right). \end{aligned} \tag{25}$$

The approximation solution of c_1 and c_2 become:

$$\begin{aligned} c_1(\eta_1, \eta_2) &\approx \frac{\eta_1\eta_2(\eta_1 + k_6')}{(\eta_1 + \eta_3 + k_6')(\eta_1 + \eta_2 + k_7')}, \\ c_{21}(\eta_1, \eta_3) &\approx \frac{\eta_1\eta_3}{(\eta_1 + \eta_3 + k_6')}. \end{aligned} \tag{26}$$

Where $k_6' = \frac{k_5'}{k_4'}$ and $k_7' = \frac{k_2'}{k_1'}$. Furthermore, other variables $e, s_1 and\ s_2$ are obtained as follows:

$$\begin{aligned} e(\eta_1, \eta_2, \eta_3) &= \frac{\eta_1(\eta_1 + k_6')(\eta_1 + k_7')}{(\eta_1 + \eta_3 + k_6')(\eta_1 + \eta_2 + k_7')}, \\ s_1(\eta_1, \eta_2, \eta_3) &= \eta_2 - \frac{\eta_1\eta_2(\eta_1 + k_6')}{(\eta_1 + \eta_3 + k_6')(\eta_1 + \eta_2 + k_7')}, \\ s_2(\eta_1, \eta_2, \eta_3) &= \frac{\eta_1(\eta_3 + k_6')}{(\eta_1 + \eta_3 + k_6')}. \end{aligned} \tag{27}$$

7. Conclusions

For intricate kinetic systems, reductions in modeling can play a significant role in obtaining analytical approximations. In this manuscript, we have implemented two model reduction techniques on the intricate model of uncompetitive inhibitor mechanisms. Both methodologies are instrumental in reducing the model into a more concise form in terms of parameters and variables. Firstly, we utilized the quasi-steady-state approximation (QSSA), which allowed us to calculate slow manifolds by partitioning the original model equations into slow and fast subsystems. The fast subsystems can be efficiently analyzed. Secondly, we employed the quasi- equilibrium approximation (QEA) to classify the reaction rates into slow and fast reactions, which enabled us to investigate the concentrations of species involved in fast reactions. Then, the fast reactions were studied and simplified. Therefore, the proposed model reduction techniques in this study can be further improved and applied to a wide range of complex mechanisms in systems biology.

DOI:https//doi.org/10.22452/mjs.vol42no2.4

6. References

Akgu¨l, A., 2019. Reproducing kernel Hilbert space method based on reproducing kernel functions for investigating boundary layer flow of a Powell–Eyring non-Newtonian fluid. Journal of Taibah University for Science, 13(1), pp.858- 863.

Akgu¨l, A., Khoshnaw, S.H. and Abdalrahman, A.S., 2020. Mathematical mod- eling for enzyme inhibitors with slow and fast subsystems. Arab Journal of Basic and Applied Sciences, 27(1), pp.442-449.

Ali, R., Akgu¨l, A. and Asjad, M.I., 2020. Power law memory of natural con- vection flow of hybrid nanofluids with constant proportional Caputo fractional derivative due to pressure gradient. Pramana, 94(1), pp.1-11.

Asjad, M.I., Ikram, M.D. and Akgu¨l, A., 2020. Analysis of MHD viscous fluid flow through porous medium with novel power law fractional differential oper- ator. Physica Scripta, 95(11), p.115209.

Bilal, S., Shah, I.A., Akgu¨l, A., Tekin, M.T., Botmart, T. and Yahia, I.S., 2022. A comprehensive mathematical structuring of magnetically effected Sutterby fluid flow immersed in dually stratified medium under boundary layer approximations over a linearly stretched surface. Alexandria Engineering Journal, 61(12), pp.11889-11898.

Bowen, J.R., Acrivos, A. and Oppenheim, A.K., 1963. Singular perturbation refinement to quasi-steady state approximation in chemical kinetics. Chemical Engineering Science, 18(3), pp.177-188.

Dangelmayr, G. and Kirby, M., 2003. Mathematical modeling: a comprehensive introduction.

Frenzen, C.L. and Maini, P.K., 1988. Enzyme kinetics for a two-step enzymic reaction with comparable initial enzyme-substrate ratios. Journal of mathematical biology, 26(6), pp.689-703.

Gorban, A.N. and Shahzad, M., 2011. The michaelis-menten-stueckelberg theorem. Entropy, 13(5), pp.966-1019.

Gorban, A.N., 2018. Model reduction in chemical dynamics: slow invariant manifolds, singular perturbations, thermodynamic estimates, and analysis of reaction graph. Current Opinion in Chemical Engineering, 21, pp.48-59.

Hashemi, M.S., Inc, M., Kilic, B. and Akgu¨l, A., 2016. On solitons and invariant solutions of the Magneto-electro-elastic circular rod. Waves in Random and Complex Media, 26(3), pp.259-271.

Heineken, F.G., Tsuchiya, H.M. and Aris, R., 1967. On the mathematical status of the pseudo-steady state hypothesis of biochemical kinetics. Mathematical biosciences, 1(1), pp.95-113.

Khoshnaw, S.H., 2015. Reduction of a kinetic model of active export of importins. In Conference Publications (Vol. 2015, No. special, p. 705). American Institute of Mathematical Sciences.

Khoshnaw, S. H. A. (2015). Model reductions in biochemical reaction networks [PhD thesis] UK: University of Leicester.

Khoshnaw, S.H. and Rasool, H.M., 2019, April. Mathematical Modelling for complex biochemical networks and identification of fast and slow reactions. In The international conference on mathematical and related sciences (pp. 55-69). Springer, Cham.

Murray, J.D., 2002. Mathematical biology: I. An introduction.

Qureshi, Z.A., Bilal, S., Khan, U., Akgu¨l, A., Sultana, M., Botmart, T., Zahran, H.Y. and Yahia, I.S., 2022. Mathematical analysis about influence of Lorentz force and interfacial nano layers on nanofluids flow through orthogonal porous surfaces with injection of SWCNTs. Alexandria Engineering Journal, 61(12), pp.12925-12941.

Shahzad, M., Arif, H., Gulistan, M., and Sajid, M. (2015). Initially Approximated Quasi Equilibrium Manifold. Journal of the Chemical Society of Pakistan, 37(2).

Shahzad, M., Sultan, F., Wahab, A., Faizullah, F., and Ur Rahman, G. (2016). Slow Manifolds in Chemical Kinetics. Journal of the Chemical Society of Pak- istan, 38(5).

Shahzad, M. and Sultan, F., 2018. Complex reactions and dynamics: advanced chemical kinetics. InTech, Rijeka.

Shahzad, M., Sultan, F., Haq, I., Ali, M. and Khan, W.A., 2019. C-matrix and invariants in chemical kinetics: a mathematical concept. Pramana, 92(4), pp.1-8.

Shahzad, A., Imran, M., Tahir, M., Khan, S.A., Akgu¨l, A., Abdullaev, S., Park, C., Zahran, H.Y. and Yahia, I.S., 2023. Brownian motion and ther- mophoretic diffusion impact on Darcy-Forchheimer flow of bioconvective mi cropolar nanofluid between double disks with Cattaneo-Christov heat flux. Alexandria Engineering Journal, 62, pp.1-15

Schnell, S. and Maini, P.K., 2002. Enzyme kinetics far from the standard quasi-steady-state and equilibrium approximations. Mathematical and Computer Modelling, 35(1-2), pp.137-144.

Segel, L.A. and Slemrod, M., 1989. The quasi-steady-state assumption: a case study in perturbation. SIAM review, 31(3), pp.446-477.

Tzafriri, A.R. and Edelman, E.R., 2004. The total quasi-steady-state approximation is valid for reversible enzyme kinetics. Journal of theoretical biology, 226(3), pp.303-313.

Whiteley, C.G., 2000. Enzyme kinetics: partial and complete uncompetitive inhibition. Biochemical Education, 28(3), pp.144-147.

Yoshino, M. and Murakami, K., 2015. Analysis of the substrate inhibition of complete and partial types. Springerplus, 4(1), pp.1-8.

MALAYSIAN JOURNAL OF SCIENCE
MJS
ISSN 1394-3065

Regular Issue

Malaysian Journal of Science 42 (2): 33-40(June 2023)
https://mjs.um.edu.my

SOLUTION OF ORDINARY DIFFERENTIAL EQUATION v^{vi} (u)=f(u,v,v',v'',v''') USING EIGHTH AND NINTH ORDER RUNGE-KUTTA TYPE METHOD

Manpreet Kaur[1a], Sangeet Kumar[2b], Jasdev Bhatti[3a]*

Abstract: The present paper presents the numerical conclusion to solve sixth order initial value ordinary differential equation (ODE). The concept of order conditions for three stage eighth order (RKSD8) & four stage ninth order Runge-Kutta methods (RKSD9) has been derived for finding global truncation error of differential equation v^{vi} = f(u,v,v', v'',v '''). The global and local truncated errors norms, zero stability of extended Runge-Kutta method (RK) is well defined and demonstrated with the help of an example.

Keywords: *Ordinary differential equations (ODE), runge-kutta type methods, local and global truncation error, zero stability*

1. Introduction

The present article works upon use of Runge-Kutta type method for solving the sixth order ordinary differential equations (ODE). According to literature review, differential equations are extensively utilized in science and engineering for mathematical modeling. Many mathematical physics issues can be stated with the aid of differential equations [13]. Hatun M et al [6] initiated ODE solver simulator for RK method. Khalid et al. [9], Pandey et al. [11] applied finite difference approach and neural network concept for examining ODE problems. The diagonally implicit fifth and sixth order RK method been initiated by Abbas F et al. [1] in 2017. Various properties such as stability of second order differential equations have also been worked upon by Mohamed et al [10]. Sohaib, et al. [12] applied Legendre wavelet collocation technique for 6th order problems. In 2021,Huang, B. et al [7] had also evaluated error analysis with implicit–explicit RK-Rosenbrock method. Islam et al [8] had done effective comparison on numerical solutions of initial value problems for ODE with Euler and RK methods. In 2021, Abdi et al [2] had analyzed global error estimation for explicit problems. The present research proposed the comprehensive approach for solving sixth order $v^{vi} = f(u, v, v' \; v'', v''')$to achieve more accuracy and stability using RKSD.

2. Runge-Kutta Type Sixth Order Ode

The initial value problem of sixth order ODE examined in the present paper are:

$$v^{vi}(u) = f(u, v, v^{'}, v^{''}, v^{'''}) \qquad [1]$$

possessing initial conditions as

$$\begin{gathered} v(u_0) = \alpha_0, v^{'}(u_0) = \alpha_0^{'}, v^{''}(u_0) = \alpha_0^{''}, \\ v^{'''}(u_0) = \alpha_0^{'''}, v^{iv}(u_0) = \alpha_0^{iv}, v^{v}(u_0) = \alpha_0^{v} \end{gathered} \qquad [2]$$

in which derivatives of fourth and fifth order do not appear explicitly. In this section, we present the general form of initial value problem Equation (1) as follows:

Authors information:
[a]Chitkara University Institute of Engineering and Technology, Punjab, INDIA, 140401.
Email: manpreet.kaur@chitkara.edu.in[1]; jasdev.bhatti@chitkara.edu.in[3]
[b]SGTB Khalsa College, Sri Anandpur Sahib, Punjab, INDIA, 140118. Email: sp7maths@gmail.com[2]
*Corresponding Author: jasdev.bhatti@chitkara.edu.in

Received: November 12, 2022
Accepted: January 5, 2023
Published: June 30, 2023

DOI:https//doi.org/10.22452/mjs.vol42no2.5

$$v_{n+1} = v_n + hv_n' + \frac{h^2}{2} v_n'' + \frac{h^3}{3!} v_n''' + \frac{h^4}{4!} v_n^{iv} + \frac{h^5}{5!} v_n^{v} + h^6 \sum_{i=1}^{s} b_i k_i \qquad [3]$$

$$v_{n+1}' = v_n' + hv_n'' + \frac{h^2}{2} v_n''' + \frac{h^3}{3!} v_n^{iv} + \frac{h^4}{4!} v_n^{v} + h^5 \sum_{i=1}^{s} b_i' k_i \qquad [4]$$

$$v_{n+1}'' = v_n'' + hv_n''' + \frac{h^2}{2} v_n^{iv} + \frac{h^3}{3!} v_n^{v} + h^4 \sum_{i=1}^{s} b_i'' k_i \qquad [5]$$

$$v_{n+1}''' = v_n''' + hv_n^{iv} + \frac{h^2}{2} v_n^{v} + h^3 \sum_{i=1}^{s} b_i''' k_i \qquad [6]$$

$$v_{n+1}^{iv} = v_n^{iv} + hv_n^{iv} + h^2 \sum_{i=1}^{s} b_i^{iv} k_i \qquad [7]$$

$$v_{n+1}^{v} = v_n^{v} + h \sum_{i=1}^{s} b_i^{v} k_i \qquad [8]$$

where

$$k_1 = f\left(u_n, v_n, v_n' , v_n'', v_n'''\right)$$

$$\begin{aligned} k_i = f\Bigg(& u_n + c_i h, v_n + hc_i v_n' + \frac{h^2 c_i^2}{2} v_n'' + \frac{h^3 c_i^3}{3!} v_n''' + \frac{h^4 c_i^4}{4!} v_n^{iv} + \frac{h^5 c_i^5}{5!} v_n^{v} + h^6 \sum_{j=1}^{s} a_{ij} k_j , v_n' + hc_i v_n'' + \frac{h^2 c_i^2}{2} v_n''' + \frac{h^3 c_i^3}{3!} v_n^{iv} \\ & + \frac{h^4 c_i^4}{4!} v_n^{v} + h^5 \sum_{j=1}^{s} \overline{a_{ij}} k_j , v_n'' + hc_i v_n''' + \frac{h^2 c_i^2}{2} v_n^{iv} + \frac{h^3 c_i^3}{3!} v_n^{v} + h^4 \sum_{j=1}^{s} \overline{\overline{a_{ij}}} k_j , v_n''' + hc_i v_n^{iv} + \frac{h^2 c_i^2}{2} v_n^{v} \\ & + h^3 \sum_{j=1}^{s} \overline{\overline{\overline{a_{ij}}}} k_j \Bigg) \quad for \quad i = 1,2,3,\ldots\ldots, s. \end{aligned}$$

The pivotal condition for RK method for sixth order differential equation is that the parameters $a_{ij}, b_i,\ b_i',\ b_i'', b_i''',\ b_i^{iv},\ b_i^{v}$ and c_i should be real for all $i,\ j = 1, 2, 3, \ldots, s$. The method will be treated explicit one if $a_{ij} = 0$ at $i > j$ however if $a_{ij} \neq 0$ at $i < j$ the method change its behavior to implicit one.

The Taylor's series concept been applied for finding relations to various parameters associated with RK method in equations (3)-(8). The main objective of research is constructing an embedded pair of the explicit RKSD methods for evaluating low value local truncated error as done by [3]–[5], [14-18] which will be useful in step-size algorithm. Method will calculate the value to the parameter $v_{n+1}, v_{n+1}', v_{n+1}'', v_{n+1}''', v_{n+1}^{iv}, v_{n+1}^{v}$ for obtaining approximate value to $v(u_{n+1}), v'(u_{n+1}), v''(u_{n+1}), v'''(u_{n+1})$, $v^{iv}(u_{n+1}), v^{v}(u_{n+1})$ where v_{n+1} is the calculated solution and $v(u_{n+1})$is the original solution. Equations (3)-(8) can be represented as:

$$v_{n+1} = v_n + h\psi \qquad [10]$$

$$v_{n+1}' = v_n' + h\psi' \qquad [11]$$

$$v_{n+1}'' = v_n'' + h\psi'' \qquad [12]$$

$$v_{n+1}''' = v_n''' + h\psi''' \qquad [13]$$

$$v_{n+1}^{iv} = v_n^{iv} + h\psi^{iv} \qquad [14]$$

$$v_{n+1}^{v} = v_n^{v} + h\psi^{v} \qquad [15]$$

The differentials for the scalar equation are:

$$F_1^{(6)} = v^{(vi)} = f(u, v, v_n', v_n'', v_n''', v_n^{iv}), \tag{16}$$

$$F_1^{(7)} = g\left(u, v, v_n', v_n'', v_n''', v_n^{iv}\right) = f_u + f_v v' + f_{v'}\, v_{uu} + f_{v''} v_{uuu} + f_{v'''} v_{uuuu} + f_{v^{iv}} v_{uuuuu} \tag{17}$$

$$F_1^{(8)} = g_u + g_v\ v' + g_{v'} v_{uu} + g_{v''} v_{uuu} + g_{v'''} v_{uuuu} + g_{v^{iv}} v_{uuuuu} \tag{18}$$

Δ is assumed to be a Taylor series increment function for which the local truncation error of $v(u), v'(u), v''(u), v'''(u),\ v^{iv}(u),\ v^{v}(u)$ is calculated from [9-15].

$$\tau_{n+1}^{p} = h[\psi^{p} - \Delta^{\mathrm{p}}], \qquad where\ p = (0), (i), (ii), \ldots\ldots, (v) \tag{19}$$

Using equations [16-18], the Taylor series increments functions of $v(u), v'(u), v''(u), v'''(u), v^{iv}(u), v^{v}(u)$ can be expressed as:

$$\Delta = v_n{}' + \frac{1}{2} h v_n{}'' + \frac{1}{3!} h^2 v_n{}''' + \frac{1}{4!} h^3 v_n{}^{iv} + \frac{1}{5!} h^4 v_n{}^{v} + \frac{1}{6!} h^5 F_1^{(6)} + O(h^6) \tag{20}$$

Similarly, solving the same for other Δ function as $\Delta', \Delta'', \Delta''', \Delta^{\mathrm{iv}}, \Delta^{\mathrm{v}}$. Using Equations (11)-(15) and Equations (16), the local truncation errors, Equation (19) will be represented as:

$$\tau_{n+1} = h^6 \left[\sum b_i k_i - \left(\frac{1}{6!} F_1^{(6)} + \frac{1}{7!} h F_1^{(7)} + \frac{1}{8!} h^{\ 2} F_1^{(8)} + \frac{1}{9!} h^{\ 3} F_1^{(9)} \ldots\ldots\ldots\right)\right] \tag{21}$$

$$\tau_{n+1}' = h^5 \left[\sum b_i' k_i - \left(\frac{1}{5!} F_1^{(6)} + \frac{1}{6!} h F_1^{(7)} + \frac{1}{7!} h^{\ 2} F_1^{(8)} + \frac{1}{8!} h^{\ 3} F_1^{(9)} \ldots\ldots\ldots\right)\right] \tag{22}$$

$$\tau_{n+1}'' = h^4 \left[\sum b_i'' k_i - \left(\frac{1}{4!} F_1^{(6)} + \frac{1}{5!} h F_1^{(7)} + \frac{1}{6!} h^{\ 2} F_1^{(8)} + \frac{1}{7!} h^{\ 3} F_1^{(9)} \ldots\ldots\ldots\right)\right] \tag{23}$$

$$\tau_{n+1}''' = h^3 \left[\sum b_i''' k_i - \left(\frac{1}{3!} F_1^{(6)} + \frac{1}{4!} h F_1^{(7)} + \frac{1}{5!} h^{\ 2} F_1^{(8)} + \frac{1}{6!} h^{\ 3} F_1^{(9)} \ldots\ldots\ldots\right)\right] \tag{24}$$

$$\tau_{n+1}^{iv} = h^2 \left[\sum b_i^{iv} k_i - \left(\frac{1}{2!} F_1^{(6)} + \frac{1}{3!} h F_1^{(7)} + \frac{1}{4!} h^{\ 2} F_1^{(8)} + \frac{1}{5!} h^{\ 3} F_1^{(9)} \ldots\ldots\ldots\right)\right] \tag{25}$$

$$\tau_{n+1}^{v} = h\ \left[\sum b_i^{v} k_i - \left(F_1^{(6)} + \frac{1}{2!} h F_1^{(7)} + \frac{1}{3!} h^{\ 2} F_1^{(8)} + \frac{1}{4!} h^{\ 3} F_1^{(9)} \ldots\ldots\ldots\right)\right] \tag{26}$$

The most important precondition for obtaining the convergence of numerical problem is evaluating zero-stability of the system, as explained by Dormand et al. [3]. The method used in current paper be written in an array form as:

$$\begin{bmatrix} 1 & 0 & 0 & 0 & 0 & 0 \\ 0 & 1 & 0 & 0 & 0 & 0 \\ 0 & 0 & 1 & 0 & 0 & 0 \\ 0 & 0 & 0 & 1 & 0 & 0 \\ 0 & 0 & 0 & 0 & 1 & 0 \\ 0 & 0 & 0 & 0 & 0 & 1 \end{bmatrix} \begin{bmatrix} v_{n+1} \\ h v_{n+1}' \\ h^2 v_{n+1}'' \\ h^3 v_{n+1}''' \\ h^4 v_{n+1}^{iv} \\ h^5 v_{n+1}^{v} \end{bmatrix} = \begin{bmatrix} 1 & 1 & \frac{1}{2} & \frac{1}{6} & \frac{1}{24} & \frac{1}{120} \\ 0 & 1 & 1 & \frac{1}{2} & \frac{1}{6} & \frac{1}{24} \\ 0 & 0 & 1 & 1 & \frac{1}{2} & \frac{1}{6} \\ 0 & 0 & 0 & 1 & 1 & \frac{1}{2} \\ 0 & 0 & 0 & 0 & 1 & 1 \\ 0 & 0 & 0 & 0 & 0 & 1 \end{bmatrix} \begin{bmatrix} v_n \\ h v_n' \\ h^2 v_n'' \\ h^3 v_n''' \\ h^4 v_n^{iv} \\ h^5 v_n^{v} \end{bmatrix}$$

DOI:https//doi.org/10.22452/mjs.vol42no2.5

The characteristic equation will be expressed as:

$$\rho(\varepsilon) = |I\varepsilon - A|$$

Hence, $\rho(\varepsilon) = (\varepsilon - 1)^6$ we get the roots to be $\varepsilon = 1,1,1,1,1,1$ which proves the desired zero stability of the proposed method as no root is found to be greater than 1 and also the multiplicity of the roots is at most 6.

2.2 RKSD8 and RKSD9 Method Order Conditions:

The order conditions derived for the three and four stage RKSD8 and RKSD9 are obtained as:

The order terms for v are:

$$\text{Sixth order:} \sum b_i = \frac{1}{6!} = \frac{1}{720}, \quad \text{Seventh order:} \sum b_i c_i = \frac{1}{7!} = \frac{1}{5040},$$

$$\text{Eighth order: } \sum b_i c_i^2 = \frac{1}{20160}, \text{ Ninth order: } \sum b_i c_i^3 = \frac{1}{60480} \qquad [27\text{-}30]$$

The order terms for v' are:

$$\text{Fifth order:} \sum b_i' = \frac{1}{5!} = \frac{1}{120}, \quad \text{Sixth order:} \sum b_i' c_i = \frac{1}{6!} = \frac{1}{720},$$

$$\text{Seventh order:} \sum b_i' c_i^2 = \frac{1}{2520}, \qquad \text{Eighth order:} \sum b_i' c_i^3 = \frac{1}{6720}, \sum b_i' c_j \overline{\overline{\overline{\overline{a_{\imath\jmath}}}}} = \frac{1}{40320}$$

$$\text{Ninth Order:} \sum b_i' c_i^4 = \frac{1}{15120} \qquad [31\text{-}35]$$

The order terms for v'' are:

$$\text{Fourth order:} \sum b_i'' = \frac{1}{4!} = \frac{1}{24}, \text{ Fifth order:} \sum b_i'' c_i = \frac{1}{5!} = \frac{1}{120},$$

$$\text{Sixth order:} \sum b_i'' c_i^2 = \frac{1}{360}, \qquad \text{Seventh order:} \sum b_i'' c_i^3 = \frac{1}{840}, \sum b_i'' c_j \overline{\overline{\overline{\overline{a_{\imath\jmath}}}}} = \frac{1}{5040}$$

$$\text{Eighth order: } \sum b_i'' c_i^4 = \frac{1}{1680}, \sum b_i'' c_j \overline{\overline{\overline{a_{\imath\jmath}}}} = \frac{1}{40320}, \sum b_i'' c_i \ \overline{\overline{\overline{a_{\imath\jmath}}}} = \frac{1}{10080}, \sum b_i'' \overline{\overline{a_{\imath\jmath}}} = \frac{1}{40320}$$

$$\text{Ninth Order: } \sum b_i'' c_i^5 = \frac{1}{3024} \qquad [36\text{-}45]$$

The order terms for v''' are:

$$\text{Third Order:} \sum b_i''' = \frac{1}{3!} = \frac{1}{6}, \qquad \text{Fourth order:} \sum b_i''' c_i = \frac{1}{4!} = \frac{1}{24}$$

$$\text{Fifth order:} \sum b_i''' c_i^2 = \frac{1}{60}, \qquad \text{Sixth order:} \sum b_i''' c_i^3 = \frac{1}{120}, \sum b_i''' \overline{\overline{\overline{a_{\imath\jmath}}}} = \frac{1}{720}$$

$$\text{Seventh order:} \sum b_i''' c_i^4 = \frac{1}{210}, \sum b_i''' c_j \overline{\overline{\overline{a_{\imath\jmath}}}} = \frac{1}{5040} \sum b_i''' c_i \ \overline{\overline{\overline{a_{\imath\jmath}}}} = \frac{1}{1260}, \sum b_i''' \overline{\overline{a_{\imath\jmath}}} = \frac{1}{5040}$$

$$\text{Eighth Order: } \sum b_i''' c_i^5 = \frac{1}{336}, \sum b_i''' c_j^2 \overline{\overline{\overline{a_{\imath\jmath}}}} = \frac{1}{20160}, \sum b_i''' c_i^2 \overline{\overline{\overline{a_{\imath\jmath}}}} = \frac{1}{2016}, \sum b_i''' c_i c_j \ \overline{\overline{\overline{a_{\imath\jmath}}}} = \frac{1}{8064},$$

$$\sum b_i''' c_i \overline{\overline{a_{\imath\jmath}}} = \frac{1}{8064}, \sum b_i''' c_j \overline{\overline{a_{\imath\jmath}}} = \frac{1}{40320}, \sum b_i''' \overline{a_{\imath\jmath}} = \frac{1}{40320}$$

$$\text{Ninth Order: } \sum b_i''' c_i^6 = \frac{1}{504} \qquad [46\text{-}62]$$

The order terms for v^{iv} are:

$$\text{Second Order:} \sum b_i^{iv} = \frac{1}{2}, \qquad \text{Third order:} \sum b_i^{iv} c_i = \frac{1}{3!} = \frac{1}{6},$$

Fourth order: $\sum b_i^{iv} c_i^2 = \frac{1}{12},$ Fifth order: $\sum b_i^{iv} c_i^3 = \frac{1}{20}, \sum b_i^{iv} \overline{\overline{\overline{a_{ij}}}} = \frac{1}{120}$

Sixth order: $\sum b_i^{iv} c_i^4 = \frac{1}{30}, \sum b_i^{iv} c_i \overline{\overline{\overline{a_{ij}}}} = \frac{1}{180}, \sum b_i^{iv} c_j \overline{\overline{\overline{a_{ij}}}} = \frac{1}{720}, \sum b_i^{iv} \overline{\overline{a_{ij}}} = \frac{1}{720}$

Seventh order: $\sum b_i^{iv} c_i^5 = \frac{1}{42}, \sum b_i^{iv} c_j^2 \overline{\overline{\overline{a_{ij}}}} = \frac{1}{2520}, \sum b_i^{iv} c_i^2 \overline{\overline{\overline{a_{ij}}}} = \frac{1}{252}, \sum b_i^{iv} c_i\ c_j \overline{\overline{\overline{a_{ij}}}} = \frac{1}{1008}$

$$\sum b_i^{iv} c_j\ \overline{\overline{a_{ij}}} = \frac{1}{5040}, \sum b_i^{iv} c_i\ \overline{\overline{a_{ij}}} = \frac{1}{1008}, \sum b_i^{iv} \overline{a_{ij}} = \frac{1}{5040}$$

Eighth order: $\sum b_i^{iv} c_i^6 = \frac{1}{56}, \sum b_i^{iv} c_j^3 \overline{\overline{\overline{a_{ij}}}} = \frac{1}{6720}, \sum b_i^{iv} c_i^3 \overline{\overline{\overline{a_{ij}}}} = \frac{1}{336}, \sum b_i^{iv} c_i^2 c_j\ \overline{\overline{\overline{a_{ij}}}} = \frac{1}{1344},$

$$\sum b_i^{iv} c_i\ c_j^2 \overline{\overline{\overline{a_{ij}}}} = \frac{1}{6720}, \sum b_i^{iv} c_j\ \overline{a_{ij}} = \frac{1}{40320}, \sum b_i^{iv} c_i\ \overline{a_{ij}} = \frac{1}{6720}, \sum b_i^{iv} a_{ij} = \frac{1}{40320}, \sum b_i^{iv} c_j^2 \overline{\overline{a_{ij}}} = \frac{1}{20160},$$

$\sum b_i^{iv} c_i^2 \overline{\overline{a_{ij}}} = \frac{1}{1344}, \sum b_i^{iv} c_i\ c_j\ \overline{\overline{a_{ij}}} = \frac{1}{6720},$ Ninth Order: $\sum b_i^{iv} c_i^7 = \frac{1}{72}$ [63-90]

The order terms for v^v are:

First Order: $\sum b_i^v = 1,$ Second order: $\sum b_i^v c_i = \frac{1}{2},$

Third order: $\sum b_i^v c_i^2 = \frac{1}{3},$ Fourth order: $\sum b_i^v c_i^3 = \frac{1}{4}, \sum b_i^v \overline{\overline{\overline{a_{ij}}}} = \frac{1}{24}$

Fifth order: $\sum b_i^v c_i^4 = \frac{1}{5}, \sum b_i^v \overline{\overline{a_{ij}}} = \frac{1}{120}, \sum b_i^v c_i\ \overline{\overline{\overline{a_{ij}}}} = \frac{1}{30}, \sum b_i^v c_j\ \overline{\overline{\overline{a_{ij}}}} = \frac{1}{120}$

Sixth order: $\sum b_i^v c_i^5 = \frac{1}{6}, \sum b_i^v c_j^2 \overline{\overline{\overline{a_{ij}}}} = \frac{1}{360}, \sum b_i^v c_i^2 \overline{\overline{\overline{a_{ij}}}} = \frac{1}{36}, \sum b_i^v c_i\ c_j\ \overline{\overline{\overline{a_{ij}}}} = \frac{1}{144},$

$$\sum b_i^v c_j\ \overline{\overline{a_{ij}}} = \frac{1}{720}, \sum b_i^v c_i\ \overline{\overline{a_{ij}}} = \frac{1}{144}, \sum b_i^v \overline{a_{ij}} = \frac{1}{720}$$

Seventh order: $\sum b_i^v c_i^6 = \frac{1}{7}, \sum b_i^v c_j^3 \overline{\overline{\overline{a_{ij}}}} = \frac{1}{840}, \sum b_i^v c_i^3 \overline{\overline{\overline{a_{ij}}}} = \frac{1}{42}, \sum b_i^v c_i^2 c_j\ \overline{\overline{\overline{a_{ij}}}} = \frac{1}{168}, \sum b_i^v c_i\ c_j^2 \overline{\overline{\overline{a_{ij}}}} = \frac{1}{840}$

$$\sum b_i^v c_j^2 \overline{\overline{a_{ij}}} = \frac{1}{2520}, \sum b_i^v c_i^2 \overline{\overline{a_{ij}}} = \frac{1}{168}, \sum b_i^v c_i\ c_j\ \overline{\overline{a_{ij}}} = \frac{1}{840}, \sum b_i^v c_j\ \overline{a_{ij}} = \frac{1}{5040}$$

$$\sum b_i^v c_i\ \overline{a_{ij}} = \frac{1}{840}, \sum b_i^v a_{ij} = \frac{1}{5040}$$

Eighth order: $\sum b_i^v c_i^7 = \frac{1}{8}, \sum b_i^v c_j^4 \overline{\overline{\overline{a_{ij}}}} = \frac{1}{1680}, \sum b_i^v c_i^4 \overline{\overline{\overline{a_{ij}}}} = \frac{1}{48}, \sum b_i^v c_i^3 c_j \overline{\overline{\overline{a_{ij}}}} = \frac{1}{192},$

$$\sum b_i^v c_i^2 c_j^2 \overline{\overline{\overline{a_{ij}}}} = \frac{1}{960}, \sum b_i^v c_i\ c_j^3 \overline{\overline{\overline{a_{ij}}}} = \frac{1}{5760}, \sum b_i^v c_j^3 \overline{\overline{a_{ij}}} = \frac{1}{6720}, \sum b_i^v c_i^3 \overline{\overline{a_{ij}}} = \frac{1}{192},$$

$$\sum b_i^v c_i^2 c_j\ \overline{\overline{a_{ij}}} = \frac{1}{960}, \sum b_i^v c_i\ c_j^2 \overline{\overline{a_{ij}}} = \frac{1}{5760}, \sum b_i^v c_j^2 \overline{a_{ij}} = \frac{1}{20160},$$

$$\sum b_i^v c_i^2 \overline{a_{ij}} = \frac{1}{960}, \sum b_i^v c_i\ c_j\ \overline{a_{ij}} = \frac{1}{5760},$$

$$\sum b_i^v c_j\ a_{ij} = \frac{1}{40320}, \sum b_i^v c_i\ a_{ij} = \frac{1}{5760}$$

Ninth Order: $\sum b_i^v c_i^8 = \frac{1}{9}$ [91-133]

2.3 Construction of Three-Stage Eighth Order RKSD Methods

The solution of equations [27-133] using three-stage eighth order RKSD8 methods the finding related to values of $c_i, b_i, b_i', b_i'', b_i''', b_i^{iv}, b_i^v$ for $i = 1,2,3$ are as:

$$c_2 = \frac{-3+4c_3}{-4+6c_3},$$
$$b_3 = \frac{1-4c_2}{20160c_3(c_3-c_2)},$$
$$b_3' = \frac{18-63c_2}{45360c_3(c_3-c_2)},$$
$$b_3'' = \frac{-3c_2+1}{360c_3(c_3-c_2)},$$
$$b_3''' = \frac{-5c_2+2}{120c_3(c_3-c_2)},$$

$$b_1 = \frac{28c_2c_3-4(c_2+c_3)+1}{20160c_2c_3},$$
$$b_1' = \frac{378c_2c_3-63(c_2+c_3)+18}{45360c_2c_3},$$
$$b_1'' = \frac{15c_2c_3-3(c_2+c_3)+1}{360c_3(c_3-c_2)},$$
$$b_1''' = \frac{20c_2c_3-5(c_2+c_3)+2}{120c_2c_3},$$
$$b_1^{iv} = \frac{6c_2c_3-2(c_2+c_3)+1}{12c_2c_3},$$

$$b_2 = \frac{4c_3-1}{20160c_2(c_3-c_2)},$$
$$b_2' = \frac{63c_3-18}{45360c_2(c_3-c_2)},$$
$$b_2'' = \frac{3c_3-1}{360c_2(c_3-c_2)},$$
$$b_2''' = \frac{5c_3-2}{120c_2(c_3-c_2)},$$
$$b_2^{iv} = \frac{2c_3-1}{12c_2(c_3-c_2)}$$

DOI:https//doi.org/10.22452/mjs.vol42no2.5

$$b_3^{iv} = \frac{1-2c_2}{12c_3(c_3-c_2)}, \qquad b_1^{v} = \frac{6c_2c_3-3(c_3+c_2)+2}{6c_2c_3}, \qquad b_2^{v} = \frac{3c_3-2}{6c_2(c_3-c_2)},$$

$$b_3^{v} = \frac{2-3c_2}{6c_3(c_3-c_2)}, \qquad c_2 = \frac{-3+4c_3}{-4+6c_3},$$

For evaluating minimal value to error norms for eighth order we need to calculate parameters which are free in nature i.e $c_3, b_i, b_i', b_i'', b_i''', b_i^{iv}, b_i^{v}$ for $i = 1,2,3$. Hence the result values of error norms are $\left\|\tau^{(8)}\right\|_2 = 787717 \times 10^{-16}$,$\left\|\tau'^{(8)}\right\|_2 = -417247 \times 10^{-9}$,$\left\|\tau''^{(8)}\right\|_2 = 200905 \times 10^{-9}$, $\left\|\tau'''^{(8)}\right\|_2 = -41094 \times 10^{-9}$, $\left\|\tau^{iv(8)}\right\|_2 = 14671286 \times 10^{-9}$ and $\left\|\tau^{v(8)}\right\|_2 = 1047605 \times 10^{-9}$and $\left\|\tau_g^{(8)}\right\|_2 = 150863684 \times 10^{-9}$.

2.4 Construction of Four-Stage Ninth Order RKSD Methods

The solution of equations [27-133] using four-stage ninth order RKSD9 methods the finding related to values of $c_i, b_i, b_i', b_i'', b_i''', b_i^{iv}, b_i^{v}\ for\ i = 1,2,3,4$ are as:

$$b_1 = \frac{1}{720} - b_2 - b_3 - b_4, \qquad b_2 = \frac{\left(\frac{c_3}{4}+\frac{c_4}{4}-c_3c_4-\frac{1}{12}\right)}{5040c_2(c_2-c_3)(c_4-c_2)}, \qquad b_3 = \frac{3(c_4+c_2)-1-12c_4c_2}{60480c_3(c_2-c_3)(c_3-c_4)},$$

$$b_4 = \frac{-(1-3(c_2+c_3)+12c_2c_3)}{60480c_4(c_3-c_4)(c_4-c_2)}, \qquad b_1' = \frac{1}{120} - b_2' - b_3' - b_4', \qquad b_2' = -\frac{[28c_3c_4-8(c_4+c_3)+3}{20160c_2(c_2-c_3)(c_4-c_2)},$$

$$b_3' = \frac{[-28c_2c_4+8(c_4+c_3)-3]}{20160c_3(c_2-c_3)(c_3-c_4)}, \qquad b_4{}' = \frac{-[28c_2c_3-8(c_2+c_3)-3]}{20160c_4(c_3-c_4)(c_4-c_2)}, \qquad b_1'' = \frac{1}{24} - b_2'' - b_3'' - b_4{}'',$$

$$b_2{}'' = \frac{-[21c_4c_3-7(c_4+c_3)+3]}{2520c_2(c_2-c_3)(c_4-c_2)}, \qquad b_3{}'' = \frac{[-21c_4c_2+7(c_4+c_3)-3]}{2520c_3(c_2-c_3)(c_3-c_4)}, \qquad b_4{}'' = \frac{-[21c_3c_2-7(c_2+c_3)+3]}{2520c_4(c_3-c_4)(c_4-c_2)},$$

$$b_1''' = \frac{1}{6} - b_2''' - b_3''' - b_4''', \qquad b_2{}''' = \frac{-[5c_3c_4-2(c_4+c_3)+1]}{120c_2(c_2-c_3)(c_4-c_2)}, \qquad b_3{}''' = \frac{-[5c_2c_4+2(c_4+c_2)-1]}{120c_3(c_2-c_3)(c_3-c_4)},$$

$$b_4{}''' = \frac{-[5c_2c_3-2(c_3+c_2)+1]}{120c_4(c_3-c_4)(c_4-c_2)}, \qquad b_1^{iv} = \frac{1}{2} - b_2^{iv} - b_3^{iv} - b_4^{iv}, \qquad b_2^{iv} = \frac{-[10c_3c_4-5(c_4+c_3)+3]}{60c_2(c_2-c_3)(c_4-c_2)},$$

$$b_3^{iv} = \frac{[-10c_2c_4+5(c_4+c_2)-3]}{60c_3(c_2-c_3)(c_3-c_4)}, \qquad b_4^{iv} = \frac{-[10c_2c_3-5(c_3+c_2)+3]}{60c_4(c_3-c_4)(c_4-c_2)}, \qquad b_1^{v} = 1 - b_2^{v} - b_3^{v} - b_4^{v},$$

$$b_2^{v} = \frac{-[6c_4c_3-4(c_4+c_3)+3]}{12c_2(c_2-c_3)(c_4-c_2)}, \qquad b_3^{v} = \frac{[-6c_2c_4+4(c_4+c_2)-3]}{60c_3(c_2-c_3)(c_3-c_4)}, \qquad b_4^{v} = \frac{[6c_2c_3-4(c_3+c_2)+3]}{12c_4(c_3-c_4)(c_4-c_2)},$$

$$c_2 = \frac{(5-24c_3)}{24-90c_3},$$

For evaluating minimal value to error norms for ninth order we need to calculate parameters which are free in nature i.e $c_3, b_i, b_i', b_i'', b_i''', b_i^{iv}, b_i^{v}$ for $i = 1,2,3,4$. Hence the result values of error norms are $\left\|\tau^{(8)}\right\|_2 = 3.3726644 \times 10^{-16}$,$\left\|\tau'^{(8)}\right\|_2 = -1.5319 \times 10^{-9}$,$\left\|\tau''^{(8)}\right\|_2 = -7.65574 \times 10^{-9}$, $\left\|\tau'''^{(8)}\right\|_2 = -2.37144 \times 10^{-9}$,$\left\|\tau^{iv(8)}\right\|_2 = 2.61167 \times 10^{-9}$ and $\left\|\tau^{v(8)}\right\|_2 = 1.35281 \times 10^{-9}$and $\left\|\tau_g^{(8)}\right\|_2 = 3.213598 \times 10^{-9}$.

3. Numerical Result and Conclusion

The efficiency of the discussed RKSD8 and RKSD9 method been well examined with the help of numerical problem.

Problem 1: The homogeneous differential equation given as: $v^{(6)} - 8v^{(3)} = 0$ with initial conditions $v(0) = 0, v'(0) = 1, v''(0) = 1, v'''(0) = 0, v^{iv}(0) = 1, v^{v}(0) = 2$

Solution: The exact solution:

$$v(u) = \frac{1}{24}\left(e^{2u} + 3u(7+3u) - e^{-u}\cos\left(\sqrt{3u}\right)\right)$$

The problem 1 with figure 1 proves the objective of proving the three stage RKSD8 been best as compared to four stage RKSD9 and direct method by computing the maximum global error (Max Error) w.r.t value step function. In other words, the proposed research work will serve as a tool for solving similar form of ODEs $v^{vi} = f(u, v, v'\ v'', v''')$ by taking into account the stability and error analysis of proposed methods as compared to traditional methods. Also from numerical results, the best outcome been received about less number of function evaluations for both RKSD8 and RKSD9 methods as compared to other existing RK methods.

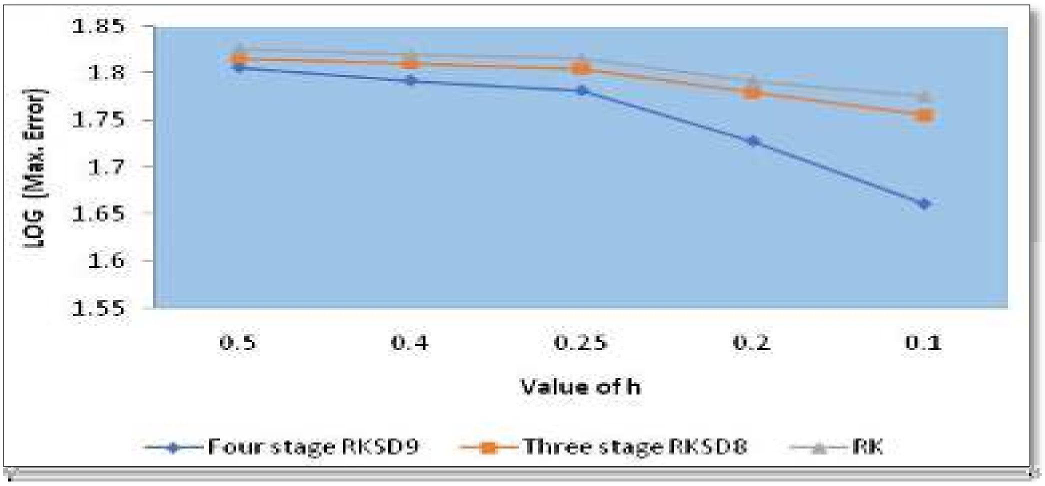

Figure 1: The efficiency curves of three stage RKSD8, four stage RKSD9 and RK method

4. References

Abbas F., Abbas Al. Sh. (2017). Solving initial value problem using Runge-Kutta 6th order method, ARPN Journal of Engineering and Applied Sciences, vol. 12(13): 3953-3961.

Abdi A., Hojjati G., Izzo G., Jackiewicz Z. (2022). Global error estimation for explicit general linear methods, Numerical Algorithms, vol. 89: 1075-1093

Dormand J.R., El-Mikkawy M.E.A., Prince P.J. (1987). Families of runge-kutta-nystrom formulae, Institute of

Mathematics and its Applications Journal of Numerical Analysis, vol. 7: 235-250.

Demba M. A., Ramos H., Kumam P., Watthayu W. (2021). An optimized sixth order explicit RKN method to solve oscillating systems," Proceedings of the XXVI Congreso de Ecuaciones Diferenciales y Aplicaciones XVI Congreso de Matematica Aplicada, Gij on (Asturias), Spain, June 14- 18: 15-22.

Ghawadri N., Senu N., Fawzi F., Ismail F., Ibrahim Z. (2018). Diagonally implicit Runge-Kutta type method for directly solving special fourth order ordinary differential equations with Ill-Posed problem of a beam on elastic foundation, Algorithms, vol. 12: 1-10.

Hatun M., Vatansever F. (2016). Differential equation solver simulator for Runge-Kutta methods, Uludag University Journal of the Faculty of Engineering, vol. 21(1): 145-162.

Huang B., Xiao A., Zhang G. (2021). Implicit-explicit runge-kutta-rosenbrock methods with error analysis for nonlinear stiff differential equations, Journal of Computational Mathematics, vol. 39(4): 569–590.

Islam M. (2015). A Comparative Study on numerical solutions of initial value problems (IVP) for ordinary differential equations (ODE) with Euler and Runge-Kutta methods, American Journal of Computational Mathematics, vol. 5: 393-404.

Khalid M., Sultana M., Zaidi F. (2014). Numerical solution of sixth-order differential equations arising in astrophysics by neural network, International Journal of Computer Applications, vol. 107(6):1-6.

Mohamed T., Senu N., Ibrahim Z., Long N. (2018). Efficient two-derivative Runge-Kutta-Nystrom methods for solving general second-order ordinary differential equations y ′ (x) = f(x, y, y′), Discrete Dynamics in Nature and Society, vol. 2018: 1-10.

Pandey P. (2018). Solving numerically a sixth order differential equation as coupled finite difference equations approach, MedCrave, vol. 2(6): 1-11.

Sohaib M., Haq S., Mukhtar S., Khan I. (2018). Numerical solution of sixth order boundary-value problems using Legendre wavelet collocation method, Results in Physics, vol. 8: 1204-1208.

Turaci M., OzisT. (2015). A note on explicit three-derivative Runge-Kutta methods (ThDRK), Bulletin of the International Mathematical Virtual Institute, vol. 5: 65-72.

Verma K., Bhardwaj S., Arya R., Ul Islam M.S., Bhushan M., Kumar A., Samant P. (2019). Latest tools for data mining and machine learning, International Journal of

Innovative Technology and Exploring Engineering, vol. 8(9): 18-23.

Shukla P.K., Sandhu J.K., Ahirwar A., Ghai D., Maheshwary P., Shukla P.K. (2021). Multi objective genetic algorithm and convolutional neural network based covid-19 identification in chest x-ray images, Mathematical Problems in Engineering, vol. 2021: 1-9

Malhotra R. (2022). Reliability and availability analysis of a standby system with activation time and varied demand, Engineering Reliability and Risk Assessment, vol. 2022: 35-51.

Kaur I., Arora S., BalaI. (2023). An improvised technique of quintic hermite splines to discretize generalized burgers-huxley type equations, Iranian Journal of Numerical Analysis and Optimization, vol. 13(1): 59-79.

Turaci M.O. (2021). Two-derivative Runge-Kutta type method with FSAL property, Journal of Modern Technology and Engineering, vol. 6(1): 47-52.

MALAYSIAN JOURNAL OF SCIENCE
MJS
ISSN 1394-3065

Regular Issue

Malaysian Journal of Science 42 (2): 41-46 (June 2023) https://mjs.um.edu.my

EVALUATION OF Zr, Ni-Cr, And Au-Ag APPLIED MATERIALS USING FEM ON PROSTHETIC CROWNS

P Vicky Kumar[1a]*, Anil Kumar Birru[2a] , Nelson Muthu[3b]

Abstract: The crown is a steady prosthesis designed to restore the functionality of a damaged tooth along, with its shape and size. They are also used to reinforce the tooth that poses long-term risk due to wide cavities and accidental injuries. The crowns are fixed using dental cement made of different materials such as porcelain cement, ceramics, etc. The present work aims to assess the mechanical properties – stiffness and strength, of the single molar crown prosthetic tooth materials to determine the efficacy of each material under typical masticatory load observed in clinical settings. To this end, the finite element method (FEM) is used to analyze the mechanical behavior of the molar crowns made of Zirconium (Zr), Nickel Chromium (Ni-Cr), and Gold alloy (Au-Ag). The crown models were created in Solidworks and exported to the ANSYS FE package. The exported three-dimensional models were subjected to varying loading conditions – vertical and oblique forces to the tooth axis under suitable displacement boundary conditions. Due to a relatively high elastic modulus, the Zr and Ni-Cr alloy exhibited a higher stress concentration and lower deformation on the crown's intaglio surface compared to the Au-Ag alloy.

Keywords: *Zirconia, nickel-chromium alloy, gold alloy, von-mises, molar crown, finite element method, masticatory load*

1. Introduction

There are many reasons for tooth damage resulting in temporary/permanent loss of tooth functionality. The tooth damage is primarily attributed to caries and non-caries effects. Caries is a disease caused by bacteria in the mouth that break down carbohydrates into sugars and release acids that attack the teeth. On the other hand, non-caries effects include ageing, another common cause of tooth loss. Some people may also develop tooth decay due to night-time clenching or rubbing (Salah et al., 2015; Tan et al., 2001). In all such cases, crowns are used to replace damaged teeth when a significant portion of the tooth functionality is lost owing to decay, wear or old filling errors. A crown is a dental restoration that replaces all or part of a tooth and is fixed to the tooth with cement to create a new outer coating. Patients may regain function, appropriate communication, and aesthetics with various crowns available in the market. It reinforces the damaged tooth while enhancing its appearance, shape, and alignment (Swain et al., 2011).

Prosthetic molar crowns have been manufactured from various metal alloys and are primarily intended to restore the masticatory function owing to the occlusal force generated in that region (Beata Dejak et al.,2012). This restoration functionality is achieved by high-grade alloy crowns such as gold-plated crowns, which were once considered the gold standard for molar prosthetic reconstruction. Long-term trials of such crowns confirm their effectiveness in clinical studies. In recent years, gold alloy crowns have become unpopular due to their esthetics and rising prices. Ceramic crowns made of stainless steel have replaced the gold-plate crowns and are commonly used today (Seong et al.,2007). Ni-based or Co-based pairs have been widely used in the base alloy group, with the recent addition of Ti alloys (Steinemann, 1998). Cr-based alloys are commonly used in Porcelain-fused-to-metal (PFM) pairs, and they facilitates the passage of material into the oral cavity and causes the formation of oxides which improves ceramic adhesion (Geurtsen, 2002; Hensten Pettersen, 2003). Glass-ceramic materials may work well in the frontal area, but the long-term performance of rear crowns is not very promising (Redemagni et al.,2002; Rousson.,2010). For the rear crown, sturdy and durable materials combinations are required, such as zirconia-based ceramics which have a high flexural strength of up to 1200 MPa and fracture toughness of 9 to 10 MPa m1/2 (Raigrodski et al.,2004; Guess et al.,2008).

Authors information:
[a]Department of Mechanical Engineering, National Institute of Technology Manipur, Imphal, INDIA. E-mail: papulappa@gmail.com[1]; birruresearch@gmail.com[2]
[c]Department of Mechanical Engineering, Indian Institute of Technology Guwahati, Guwahati, INDIA. E-mail: nelsonm@iitg.ac.in[3]
*Corresponding Author: papulappa@gmail.com

Received: March 14, 2022
Accepted: January 25, 2023
Published: June 30, 2023

DOI:https//doi.org/10.22452/mjs.vol42no2.6

Many factors contribute to the functioning of the crown. Fabricating a durable ceramic crown requires an accurate estimation of the stress distribution under various masticatory functions and fracture strength. By separating food using the enamel on the tooth tips, the crown's mechanical function is to start the initial digestion. Therefore, tooth enamel alternatives should have a hardness value equal to or lower than that of tooth enamel. Dentin substitutes must exhibit maximum stress, maximum strain, and modulus equal to or greater than that of dentin. A broken tooth's crown has been repaired using various materials to improve the tooth's appearance and functionality (Erkmen et al.,2012; Matacena et al.,2014). In recent research, virtual models of biomedical devices and analyses of stress distributions in important regions have been developed using parametric FEM and von-Mises analysis. Utilizing models made with engineering software and those recently published in the worldwide literature, current research is conducted (Cervino et al.,2015; Maiorana et al.,2008).

The FEM is one of the popular engineering tools available today for analyzing, modifying, and improving design (Zahedi et al. 2013a, b; Shamsi-Sarband et al. 2012). Currently, this technique is used in biomedical engineering for patient-specific design, reduction of redundant parts of various machinery and structure, visualization, geometric modelling, and performance analysis (Mohamed et al., 2015; Afolabi et al.,2018; Ladapo et al., 2015). To provide high-quality homogeneous dental goods with custom-made implants, a balance between the manufacturing process and lower production costs has motivated several researchers to utilize FEM in the design and development approach. Using the FE tool, the stress distribution of the zirconium coping designs under various loads was computed (Seung-Ryong et al., 2016; Jeong et al.,2013; Oladapo et al.,2015; Christianah et al.,2016). Therefore, FEM can be used as a suitable design technique for identifying the issues leading to dental restorative failure when crowns are used. The primary goal of the present study was to examine the mechanical characteristics of single crowned prosthodontic dental materials under various loading conditions that correspond to the clinical settings.

2. Materials and Methodology

2.1 Pre- Processing Finite Element Analysis (FEA)

The first step in developing a finite element model is to create a 3D geometry from the processed tooth crown. The DICOM (Digital Imaging and Communication in Medicine) data is included in a 3D slicer model structure (Figure 1). The software can separate tissue data from the DICOM files on all three standard geometric planes before rendering the selected data into a 3D digital model. The software works using a series of indicator function areas within a particular set, allowing for rapid separation of different tissue types such as bone and soft tissue. This procedure was used to separate the patient's bone using the automated threshold feature, designed to resolve bone tissue from the CT (Computed Tomography) scans ranging from 500 to 1000. The 3D model is further refined to include the enamel, as well as parts of the lower and upper jaws.

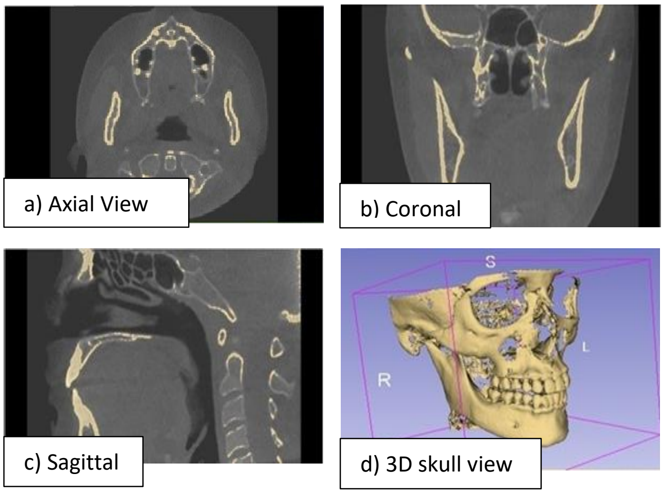

Figure1. (a, b, c) Anatomical MR slices of the head in the 2D slice at axial, coronal, sagittal view and (d) 3D model of the skull in 3D viewer.

As shown in (Figure 2), a single molar crown was extracted from the complete 3D tooth model using a scissors tool to separates the exported 3D mask in STL (stereolithography) file format, and further modifications were made using the AutoCAD 2020 package. The model was exported to the ANSYS FE package in iges format. The solid model was broken down into different parts before the analysis for meshing in the ANSYS workbench. The meshing was done using the four noded tetrahedral elements, as shown in (Figure 3). The meshed model had 2,54,676 nodes, whereas the element count was 1,72,523. The mesh parameters used were sufficient to produce good quality mesh. The materials utilized in the analysis and their mechanical properties are displayed in Table1. Each solid component has been assigned its respective material property in the FE model.

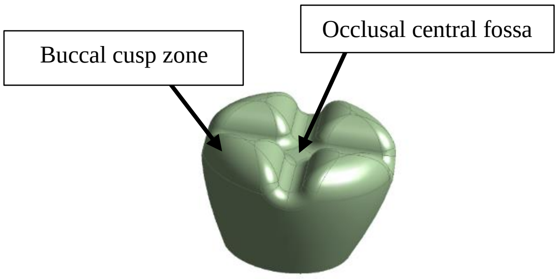

Figure 2. Isometric view of the molar crown

DOI:https//doi.org/10.22452/mjs.vol42no2.6

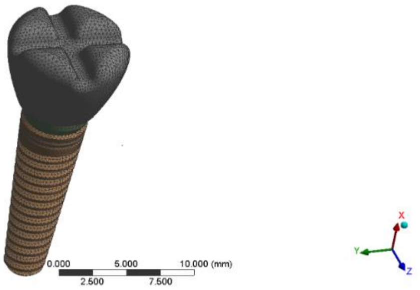

Figure 3. Tetrahedral meshing of a dental crown with abundant screw

2.1 Material and Load Conditions

All the building materials for the dental crown with the abundant screw were considered homogeneous, elastic, and isotropic. The displacement of the nodes corresponding to the surface of the abundant screw was fixed.

The buccal cusp zone and occlusal central fossa received a static load of 100 N. The FE models were subjected to two loading conditions: (1) vertical loading and (2) oblique loading from the buccal side, at 300 and 450 to the tooth axis. The von-Mises stress (Eq.1) and the total deformation parameters were considered for assessing the performance of various dental crowns.

$$\sigma_{vm} = \sqrt{\frac{(\sigma_1 - \sigma_2)^2 + (\sigma_2 - \sigma_3)^2 + (\sigma_3 - \sigma_1)^2}{2}} \qquad (1)$$

where σ_1, σ_2, and σ_3 are principal stresses and σ_{vm} is the von-Mises stress.

Table 1. Material Properties of Biocompatible materials involved in the study.

Material	Density(Kg/m3)	Poisson's Ratio	Young's Modulus (GPa)	Yield Strength (MPa)
Gold Alloy (Ag-Au)	8000	0.33	91	800
Ni-Cr	8400	0.325	245	2100
Zirconia	4560	0.26	97	810

3. Results and Discussions

The model was examined using the ANSYS workbench for the load applied vertically, at 300 and 450 to the tooth axis, and the resulting von-Mises stress and total deformation distribution were examined. The amount and direction of the applied masticatory force determine the multiaxial stress distribution of the treated tooth that has been repaired. The von-Mises stress under one applied load is depicted in (Figures 4 and 5) in terms of its values and patterns. Dark blue (the lowest stress) to red (the highest stress) colour banding is used to depict the stress profile. Following vertical contact with neighboring teeth, the stress progressively shifts away from the stress point and toward the remainder of the crown. However, the maximal load is confined to the crown and barely penetrates the underlying teeth. For each material, (Figures 6 and 7) illustrate the maximum von-Mises and the total deformation, respectively. According to the static analysis, the Au-Ag alloy had a maximum von-Mises stress of 20.01 MPa and a maximum displacement of 0.00143 mm when the axial load was applied. The maximum von-Mises stress for the Ni-Cr alloy material was 39.6 MPa and the material deformed by 0.00687 mm in response to an applied axial load. When the oblique load was applied, Zr was subjected to the maximum stress of 24.96 MPa and a maximum deformation of 0.00143 mm. For the Ni-Cr alloy model material, (Figure 6) displays the maximum equivalent stress profile observed.

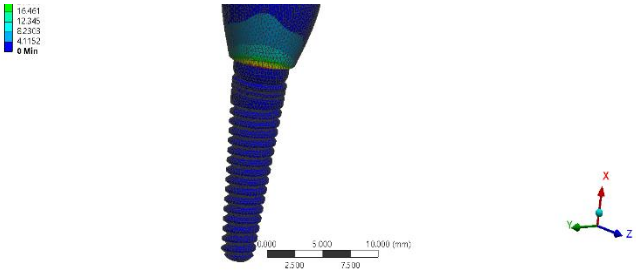

Figure 4. Equivalent Load at the axial condition for Zirconia

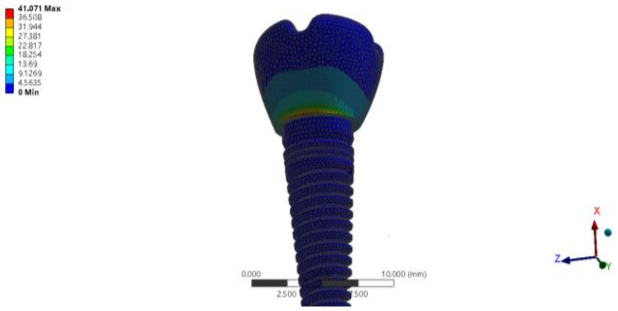

Figure 5. Equivalent Load at the axial condition for Nickel-Chromium alloy.

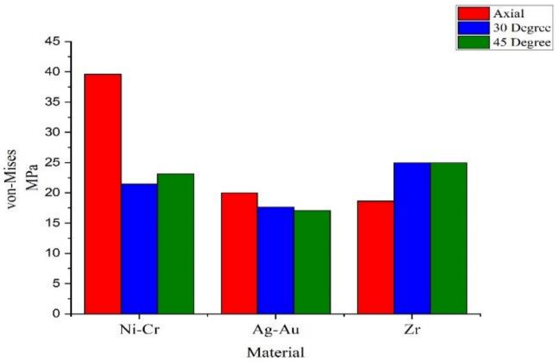

Figure 6. von-Mises stress at 100N load (axial, 30o, and 45o).

DOI:https//doi.org/10.22452/mjs.vol42no2.6

(Figures 8 and 9), demonstrate that the region immediately above the fixed basal region had the highest stress values because, when subjected to force, this region was unable to deform because all degrees of freedom for the base were locked. On the other hand, the crown curved around the base when oblique force (300 and 450) was applied. As a result, under the second load condition, the anterior region was compressed, while the posterior region was stretched, resulting in a high-stress zone around the base in both the front and back views shown in (Figure 5). For the following reasons, it was also shown in (Figure 4), that the entire anterior top portion of the crown was a zone of significant stress under vertical force. High irregularity, multiple uneven contours, and significant stress concentration factors were identified in this region of the crown. The issue of stress distribution and masticatory force, which affects the periodontium and replaces the tooth material such as veneer porcelain on zirconia, has received a lot of attention in recent research (Vaidyanathan et al.,2013; Granell-Ruiz et al.,2012).

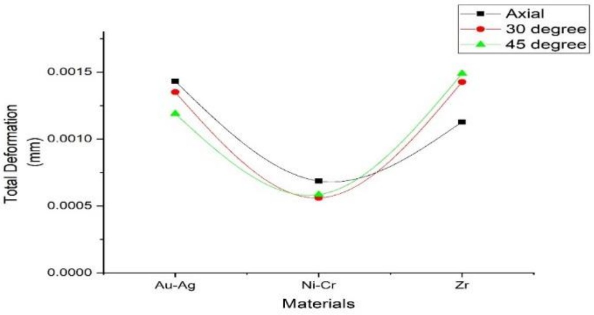

Figure 7. Total Deformation for masticatory load of 100 N (axial, 300, and 450).

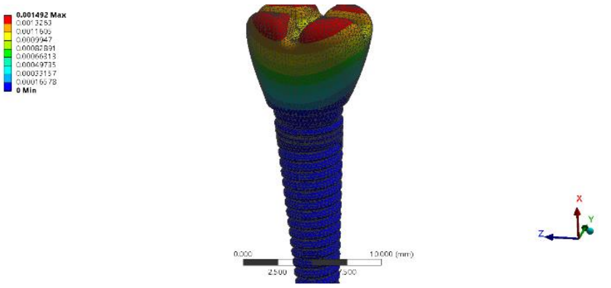

Figure 8. Total Deformation of Gold alloy (Au-Ag) at axial

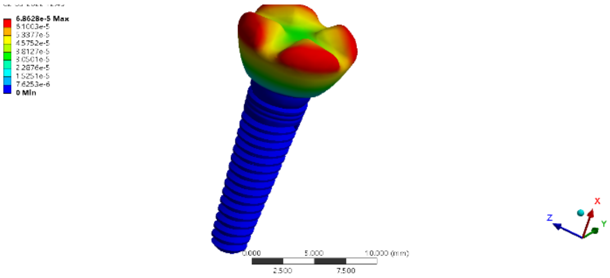

Figure 9. Total Deformation of Ni-Cr at axial load

The results of this study clearly supports the recent literature findings. There is no ideal material to replace the anatomical features of a natural tooth. For fixed prostheses, creating temporary restorations from dental resins is a necessary step. The pulp capping protection, position stability, occlusal function, cleanability, marginal accuracy, wear resistance, strength, and aesthetics standards must all be met by temporary resin crowns. They serve an essential role in providing a template for the final restoration after being evaluated in the oral cavity. However, these research findings indicate that dental resins have a low fracture resistance, and a high risk of destruction, and cannot be used for prolonged chewing cycles. Significant efforts have been made to strengthen the strength and dependability of dental ceramic systems in response to the patient’s aesthetic demand for a white metal-free, tooth-colored prosthesis. According to (Regish et al.,2011), restoring missing teeth has become one of the most critical requirements for patients visiting the clinic to restore aesthetics and function. There are numerous procedures that can replace a single lost crown. Each surgical procedure has distinct advantages and disadvantages that can be thought of as a predictable long-term treatment option.

The clinical results of using gold or Ni-Cr alloys are predictable and safe, and their use is well documented in contemporary research (Lauritano et al.,2016). The high degree of fracture, uniformity, and gradual consumption of gold alloys, when compared to the findings of recent investigations, suggest that they are more resilient to long-term stress distribution. The Ni-Cr alloy has an excellent tensile strength as well. With no fractures across numerous extended masticatory cycles, the von-Mises stress distribution demonstrated similar results for Au-Ag and Ni-Cr. From another perspective, recent research has focused on assessing the consistency and durability of metal-free prosthetic single crowns. These materials highlighted the fantastic results of the anterior teeth, but the posterior region, which was influenced by the strong masticatory force, resulted in crown fractures with no long-term benefits.

For front free-contact teeth, zirconia can be considered the best framework ceramic, but for posterior restorations using Ni-Cr alloys, the masticatory cycle is crucial to predicting long-term performance prior to clinical usage. The current model was validated and confirmed in accordance with the goal of the study using the static finite element analysis, according to earlier research published by (Tsouknida et al.,2013). A crucial criterion for model reliability is the application of realistic loads and boundary conditions since the predictive capacity of the simulation is linked to the interaction variables taken into account during the analysis. The created model is thought to offer a respectable level of reliability for qualitative risk assessment of procedural variables related to the masticatory cycle based on specified parameters. Each operative procedure can be assumed to be a long-term treatment option with pros and cons. And the final goal is to make technical suggestions related to virtual models, not clinical recommendations.

4. Conclusion

From the present investigations, three biocompatible materials, Au-Ag, Ni-Cr and Zr alloys, were chosen based on the patient functional requirements and other preferences such as location of the dental implants, duration of the treatment, and the cost. The position of the force greatly influenced the stress distribution pattern. However, the von Mises stress were found to be low to cause crown failures. Zirconia has the advantage of being aesthetically pleasing, but one has to take into account its low fracture toughness during the dental restoration procedure to avoid fractures during mastication especially in molar and posterior regions. The elastic modulus of the Ni-Cr alloy is higher among the three materials, and therefore the deformation will be low. In terms of durability, gold crowns are preferred, but they are costly. The presented model is a 3D virtual model; therefore, additional research is needed to ensure the durability and long-term clinical success of the materials used.

5. Acknowledgment

The authors would like to acknowledge the Department of Mechanical Engineering, NIT MANIPUR, Govt of India for Financial Support to carry out the numerical simulation.

6. References

Afolabi, Samuel O., Oladapo, Bankole I., Ijagbemi, Christianah O., Adeoye, Adeyinka O.M., Kayode, Joseph F. (2018). Design and finite element analysis of a fatigue life prediction for safe and economical machine shaft. J.Mater.Res.Technol.http://dx.doi.org/10.1016/j.jmrt.2017.10.007.

Alhasanyah, A., Vaidyanathan, T.K., Flinton, R.J. (2013). Effect of core thickness differences on post-fatigue indentation fracture resistance of veneered zirconia crowns. Journal of Prosthodontics, vol. 22, no. 5, pp. 383–390.

Augstin-Panadero, R., Fons-Font, A., Roman-Rodriguez, J.L., Granell-Ruiz, M., Rio-Highsmith, J., Sola-Ruiz, M.F. (2012) Zirconia versus metal: a preliminary comparative analysis of ceramic veneer behaviour. The International Journal of Prosthodontics, vol. 25, no. 3, pp. 294–300.

Bankole, I., ladapo, O., Stephen, Aban, Temitayo, Azeez M., Oluwole, AfolabiS. (2015). Computer aided drafting and construction of standard drafting table for college of engineering studio in a febabalola university. Int. J. Sci. Eng. Res. 6 (8).

Beata Dejak., Andrzej Mlotkowski., Ceary Langot. (2012). Three-dimensional finite element analysis of molars with thin-walled prosthetic crowns made of various materials. Dental Materials 28, 433-441

Cicciu, M., Beretta, M., Risitano, G., Maiorana, C. (2008). Cemented-retained vs screw-retained implant restorations: an investigation on 1939 dental implants. Minerva Stomatologica, vol. 57, no. 4, pp. 167–179.

Cicciu, M., Bramanti, E., Matacena, G., Guglielmino, E., Risitano, G. (2014). FEM evaluation of cemented-retained versus screw retained dental implant single-tooth crown prosthesis. International Journal of Clinical and Experimental Medicine, vol. 7, no.4, pp. 817–825.

Cicciu, M., Cervino, G., Bramanti, E. (2015). FEM analysis of mandibular prosthetic overdenture supported by dental implants: evaluation of different retention methods. Computational and Mathematical Methods in Medicine, vol. 2015, Article ID 943839.

Conrad, H., Seong, W.J., Pesun I. (2007). Current ceramic materials and systems with clinical recommendations: a systematic review. J Prosthet Dent 98:389–404.

Fradeani, M., Redemagni, M. (2002) An 11-year clinical evaluation of leucite-reinforced glass-ceramic crowns: a retrospective study. Quintessence Int 33,503–10.

Geng, J.P., Tan, K.B., Liu, G.R. (2001). Application of finite element analysis in implant dentistry: a review of the literature. J. Prosthet. Dent. 85 (6), 585–598.

Geurtsen, W. (2002). Biocompatibility of dental casting alloys. Crit Rev Oral Biol Med 13, p. 71.

Guess, P.C., Kulis, A., Witkowski, S. (2008). Shear bond strengths between different zirconia cores and veneering ceramics and their susceptibility to thermocycling. Dent Mater 24,1556-1567.

Ha, S.R., Kim, S.H., Han, J.S., Yoo, S.H., Jeong, S.C., Lee, J.B. (2013). The influence of various core designs on stress distribution in the veneered zirconia crown: a finite element analysis study. J. Adv. Prosthodont. 5, 187–197.

Heintze, S.D., Rousson, V. (2010) Fracture rates of IPS empress all-ceramic crowns – a systematic review. Int J Prosthodont 23,129–33.

Hensten-Pettersen, A. (2003). Disintegration of orthodontic appliances in Dental Materials in vivo:aging and related phenomena. Quintessence Publishing Co. Inc, p. 125.

Ijagbemi, Christianah O., Oladapo, Bankole I., Campbell, Harold M., Ijagbemi, Christopher O. (2016). Design and simulation of fatigue analysis for a vehicle suspension

DOI:https//doi.org/10.22452/mjs.vol42no2.6

system (VSS) and its effect on global warming. Proc. Eng. 159 (2016), 124–132. http://dx.doi.org/10.1016/j.proeng.2016.08.135.

Lauritano, F., Runci, M., Cervino, G. (2016). Three dimensional evaluation of different prosthesis retention systems using finite element analysis and the von-Mises stress test. Minerva Stomatologica. Vol. 65, 353-367.

Meric, G., Erkmen, E., Kurt, A., Eser, A., Ozden, A.U. (2012) Biomechanical comparison of two different collar structured implants supporting 3-unit fixed partial denture: a 3-D FEM study. Acta Odontologica Scandinavica, vol.70, no. 1, pp. 61–71.

Michailidis, N., Karabinas, G., Tsouknidas, A., Maliaris, G., Tsipas, D., Koidis, P. (2013). A FEM based endosteal implant simulation to determine the effect of peri-implant bone resorption on stress induced implant failure. Bio-Medical Materials and Engineering, vol. 23, no. 5, pp. 317–327.

Mohamed, I.E., Salah, A.Y., Tarek, A.S., Mahmoud, M.S., Wael, S.O. (2015). A finite element study on stress distribution of two different attachment designs under implant-supported overdenture. Sau. Dental J. 27, 201–207.

Oladapo, Bankole, I., Vincent, Balogun, A., Oke, Augustine, O., Agbor, Esoso A. (2015). Design and finite element analysis on car seat height screw adjuster using autodesk inventor. Int. J. Sci. Res. Eng. Stud. (IJSRES) 2 (8).

Raigrodski, A.J. (2004) Contemporary materials and technologies for all-ceramic fixed partial dentures: a review of the literature. J Prosthet Dent 92,557–62.

Regish, K.M., Sharma, D., and Prithviraj, D.R. (2011). Techniques of fabrication of provisional restoration: an overview. International Journal of Dentistry, vol. 2011, Article ID 134659.

Seung-Ryong, H., Sung-Hun, K., Jai-Bong, L., Jung-Suk, H., In-Sung, Y., Seung-Hyun, Y. (2016). Effects of coping designs on stress distributions in zirconia crowns: Finite element analysis. Ceram. Inter. 42, 4932–4940.

Steinemann, S.G. (1998). Titanium materials of choice. Periodontology 17, p. 7.

Shamsi Sarband, A., Zahedi, S.A., Bakhshi Jouybari, M., Hossinipour, S.J., Banabic, D. (2012). Optimization of the pressure path in sheet metal hydroforming. Proceed. Roman. Acad. 13, 351–359.

Thompson, M.C., Thompson, K.M., Swain, M. (2011). The all-ceramic, inlay-supported fixed partial denture. part 2. fixed partial denture design: a finite element analysis. Aust. Dent. J. 56, 302–311.

Zahedi, S.A., Demiral, M., Roy, A., Silberschmidt, V.V. (2013a). FE/SPH modelling of orthogonal micro-machining of fcc single crystal. Comput. Mater. Sci. 78, 104–109.

Zahedi, S.A., Roy, A., Silberschmidt, V.V. (2013b). Modeling of micro-machining single crystal fcc metals. Procedia CIRP 8, 346–350.

DOI:https//doi.org/10.22452/mjs.vol42no2.6

MALAYSIAN JOURNAL OF SCIENCE
MJS
ISSN 1394-3065

Regular Issue

Malaysian Journal of Science 42 (2): 47-55 (June 2023) https://mjs.um.edu.my

SPECTRAL AND STRUCTURAL ANALYSIS FOR SODIUM SILICATE-BASED AEROGEL VIA NORMAL DRYING PRESSURE

Wasan H. Al-husseny[1a], Israa F. Al-sharuee[2a] and Ban R. Ali[3a]

Abstract: Five types of silica aerogel were prepared at ambient pressure: sodium silicate, TEOS, and sodium silicate, with TEOS utilized as precursors. We investigated the effects of catalysis, mixing water or ethanol with the precursors, as well as the procedure of modification. Aqueous is a low-cost alternative, and many applications utilize it. A manufacturing colloidal silicic acid hydrosol was created from the ion exchange of an industrial water glass. The properties of physical, chemical, and hydrophobicity were examined via density, XRD, FTIR, and contact angle. BET, FESEM, and EDS analysis determined the structural properties. The silica hydrogel's pore liquid (H_20) was successively removed. The spectral properties confirmed the modification by the derived high contact angle of 152º, low transparency, and amorphous structure. The resulting aerogel monoliths have a well-developed mesoporous structure, a large specific surface area of 961 m2/g, and a low density of 0.04 g/cm3.

Keywords: *Ambient pressure, sodium silicate, aerogel, hydrophobicity, contact angle*

1. Introduction

Silica aerogel has a three-dimensional nanoporous structure. An aerogel is an ultra-porous substance with a strongly cross-linked network structure, 90% composed of pores (Dorcheh & Abbasi, 2008). These are made up of mesopore cells, which are semitransparent and heat-insulating materials (Huang et al., 2019). It has several unique features, including a good specific surface area and good porosity (Feng et al., 2018; He & Chen, 2017; Pan et al., 2017), optical transmission (99%), high porosity (98%), and low thermal conductivity (0.01 W/mK) (Al-Mothafer, Abdulmajeed, & Al-Sharuee, 2021). They have attracted great interest and demonstrated good market potential. This has the potential to be employed in a variety of fields, including adsorption (Israa F Al-sharuee & Mohammed, 2019; Mazrouei-Sebdani, Salimian, Khoddami, & Shams-Ghahfarokhi, 2019; Wingfield, Franzel, Bertino, & Leventis, 2011), thermal insulation (Israa F Al-sharuee, 2019; X.-D. Wang, Sun, Duan, & Hu, 2013), sensors and dielectrics (He et al., 2019), fusion targets (Daniel, Longo, Ricciardi, Reverchon, & Guerra, 2013; Wagh, Ingale, & Gupta, 2011), and catalysts (Zhang, Chen, Zhang, Ye, & Cui, 2021). The sol-gel technique was employed to produce silica, which comprised the reaction of water with the silica precursor in the presence of a solvent such as acetone or ethanol, as well as the use of a necessary catalyst and supercritical drying during the final stage (Aegerter, Leventis, & Koebel, 2011).

Two types of silicon precursors are used to make silica aerogels. Organ silanes can be tetraethoxysilane TMOS, methyl-hydro siloxane PMHS (Bhagat & Rao, 2006; Nguyen et al., 2010) or Na_2SiO_3 (Al-Mothafer & Abdulmajeed, 2021). TEOS may produce wet gels, although it has fractures and can break into small pieces under normal pressure. Wet gels composed from xerogels use a vapor passing technique or ion exchange procedures to make the water glass-based aerogels, which include eliminating the sodium from the water glass (Durães et al., 2012). Several studies have found that hexadecyltrimethoxysilane with tetraethoxysilane or dimethyl diethoxy silane with tetraethoxysilane was employed to make hydrophobic silica aerogels (Zhou, Shen, Wu, Wu, & Ni, 2007). Silica sol and tetraethoxysilane are examples of organic-inorganic materials (Li, Jiang, Xu, Hai, & Zheng, 2016). Researchers have paid close attention to cost-effective and efficient preparation methods for silica aerogel powders. In two hours, Wang et al. (2015) were able to obtain silica aerogel powders. However, they employed tetraethyl orthosilicate as a precursor, which is expensive and difficult to apply in large-scale industrial manufacturing (J. Wang, Zhang, Wei, & Zhang, 2015). Yajun Huang et al. (2012) investigated the production of water glass-based aerogel granules. Under ambient pressure drying, organic solvents can be saved. Within six hours, a unique method of preparing nano porous silica aerogel was reported under ambient pressure. The resulting silica aerogel has a homogeneous

Authors information:
[a]Department of Physics, College of Science, Mustansiriyah University, Baghdad, IRAQ. E-mail: wasanhassan@uomustansiriyah.edu.iq[1]; i81f54@uomustansiriyah.edu.iq[2;]
banrasheed2003@yahoo.com[3]
*Corresponding Author: i81f54@uomustansiriyah.edu.iq

Received: April 26, 2022
Accepted: September 7, 2022
Published: June 30, 2023

DOI:https//doi.org/10.22452/mjs.vol42no2.7

mesoporous structure and low thermal conductivity (0.0237–0.0245 W/mK at 1 atm), according to the results of the tests (Monshi, Foroughi, & Monshi). In this work, five types of silica aerogel were prepared at ambient pressure: sodium silicate, TEOS, and sodium silicate, with TEOS utilized as precursors. The effects of the catalysis, mixing water or ethanol with the precursors, and the procedure of modification, were investigated.

2. Experimental Part

2.1 Materials

Sodium silicate powder (Na_2SiO_3), M.W.212.14 g/mol, 99.9%), and Tetraethylorthosilicate Si ($OC_2H5)_4$ (TEOS, 98%) were obtained from Sigma-Aldrich, (Germany). Trimethylchlorosilane ($(CH_3)_3SiCl$ (TMCS > 98%) (TCI Japan) and n-Hexane (C_6H_{14} > 98 %) were obtained from Chemo-LAB (Belgium). Ethanol was obtained from Schariau (Spain) (99%). CDH provided hydrochloric acid (MW 36.45g/mol, 99.0%) and ammonium solution (NH_4OH M.W. 17.03 g/mol) (INDIA). Amberlite (IR-120 Na)

2.2 Sample preparation and characterization methods

Five samples were prepared for the production of hydrophobic silica aerogel. The flow chart illustrates the preparation steps undertaken. The completion of modification and the band vibration were prepared by FTIR spectroscopy (Bruker FTIR Spectrometer ALPHA II, USA). The crystallites were validated using XRD analysis (GaliPIX3D X-ray Detector | 2D Hybrid Pixel XRD Detector) (1.5406 A^{o}). The green size was calculated by the Scherrer Equation (Monshi et al., 2012):

$$L = \frac{K\lambda}{\beta \cos \theta} \qquad (1)$$

where K is constant, and is most commonly taken as 0.9, λ is the wavelength of the X-ray at 1.5406 A^{o} at full width and at half maximum of peak, and θ is the Braggs angle. The morphology and percentage of the elements involved FESEM and EDS analysis. Mass and volume measurements were used to calculate the bulk density of the aerogel. The volume was calculated using V= R^2h, where R is the radius and h is the height. The bulk density = m/V if "m" signifies its mass. Besides the specific surface area and average pour volume, they were determined via BET analysis (BELSORP-mini II) at varied partial pressures (0.01p/p_{01}). Contact angle measurements were used to evaluate the hydrophobicity (3µ). The volume of a water drop was placed on the top surface of a sample. The contact angle (θ) was determined using the equation (2), where h, w is the drop's height and width, respectively (Khedkar, Somvanshi, Humbe, & Jadhav, 2019; Zhao, Li, & Zhang, 2018).

$$\theta = 2\tan^{-1}\frac{2\,h}{w} \qquad (2)$$

Five different types of samples were produced: W1, W2, W3, W4, and W5. W1 and W2 are similar in preparation but differ in the washing process: after being converted to gel, W1 was soaked in (50% water+50% ethanol) for 24 hours twice, whereas W2 was soaked in (100% ethanol) for 24 hours twice. W3 was prepared from condensed silica only with (TEOS: Eth: HCl [0.1M]) with (2.17: 5: 0.23). W4 is similar to sample W1, but differs by not adding HCl before ion exchange. W5 was prepared from silicic acid only (the ratio of sodium silicate to distilled water was 1:4). All samples were converted to gel by adding 1N of NH4OH drop by drop, and the surface modification by TMCS and n-Hexane were preserved at a ratio of [1:6 M] at 60 ^{o}C for 24 hours. Then n-Hexane was added for 24 hrs, two times around the holder in a small perforated plastic lid before allowing it to dry at ambient pressure for 72 hrs. The samples were then placed under 120 ^{o}C every 10 ^{o}C to obtain the hydrophobic silica aerogel.

3. Results and Discussion

3.1. FTIR analysis

Tables 1 and 2 and Figure 1 illustrate the hydrophobicity properties and vibrational alterations as a result of FTIR spectra, where υ, stretching vibration; υ_s, symmetric stretching vibration; υ_{as}, antisymmetric stretching vibration; δ, deformation vibration; δ_s, symmetric deformation vibration (bending); and ν_β, in-plane stretching vibration (Shirtcliffe, McHale, Newton, & Perry, 2003). From FT-IR, Si-CH_3 at 3995 cm^{-1} indicates that a considerable fraction of the Si atoms on the surface was hydroxylated. The O-H stretching band of hydrogen 3995 cm^{-1} linked water molecules caused the broad absorption peak centered at cm^{-1} (H-O-H). Peaks at 2057 cm^{-1} and 1480 cm^{-1} correspond to OH and Si-OH, respectively, indicating that the silica surface remains unchanged (Bhagat et al., 2008; Cheng et al., 2016). Peaks at 842 cm^{-1} and 2995 cm^{-1} are attributed to Si-CH_3 bending at 1200 cm^{-1}. These peaks are the result of TMCS altering the surface of the silica aerogel. The hydrophilic (Si-OH) types were replaced by hydrophobic (Si-CH_3) collections when the gel surface was changed with Hexane-TMCS solution, as evidenced by the disappearance of a peak at 1131 cm^{-1}. The irregular stretching and bending vibrations, which correspond to Si-O-Si bonding, demonstrate a significant absorption peak at 1055 cm^{-1} and 1045 cm^{-1}, respectively (Sarawade, Kim, Hilonga, & Kim, 2010; Shi et al., 2017).

DOI:https//doi.org/10.22452/mjs.vol42no2.7

Table 1. The vibration of bands as a result of FTIR examination

Type of vibration Sample	Si-OH H-OH	υsC-H	υ_{as}C-H	δH-O-H	δ_sSi-CH	υ_{as}Si-O-Si	υ_{β}Si-OH	νSi-CH	ν_SSi-O-Si
W1	3650	2971	2177	1706	1262	1065	1138	842	488
W2	3745	2963	2366	2054	1250	1043	1177	841	450
W3	3746	2986	2346	1774	1266	1067	1126	844	468
W4	3753	2963	2362	2089	1255	1072	1137	841	442
W5	3760	2362	2961	1699	1257	1060	1130	845	439

Table 2. Percentage of intensity variation depended on Si-O-Si length

sample	length	Si-OH	Si-CH	CH	OH
W1	81.70	1.317	4.47	17.58	35.55
W2	94.07	2.64	3.12	15.73	35.79
W3	80.43	2.76	3.14	15.49	35.78
W4	79.82	1.93	2.65	14.55	37.15
W5	78.69	15.23	28.65	14.14	35.78

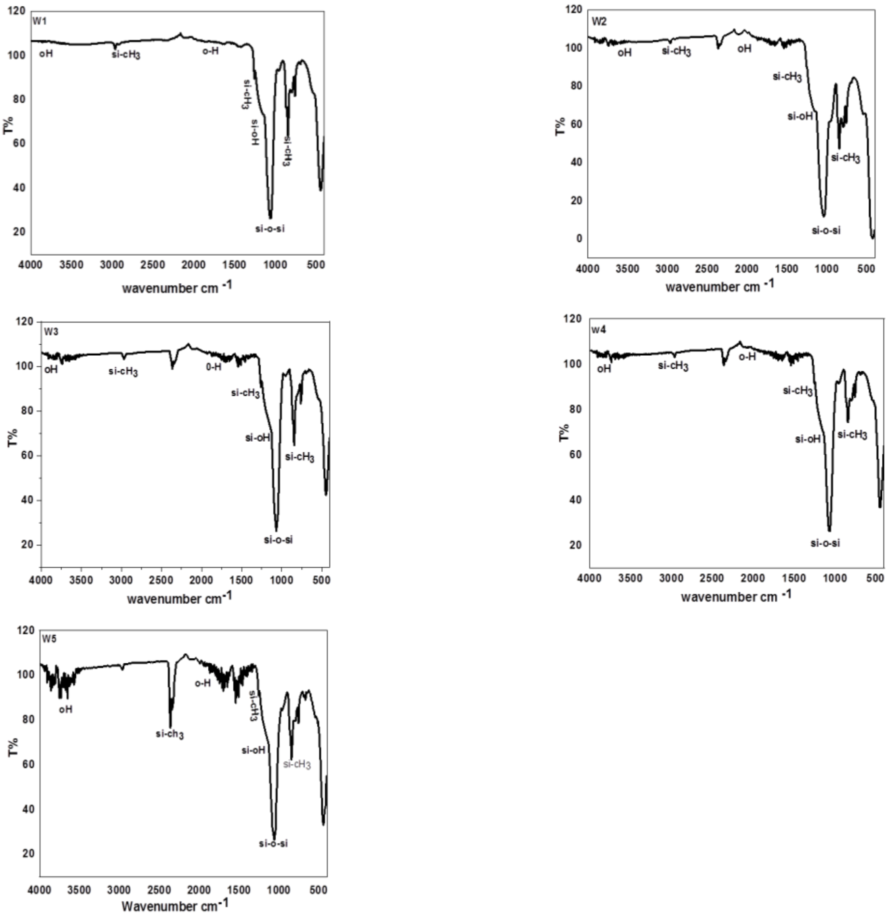

Figure 1. FTIR spectrum for W1, W2, W3, W4 and W5 samples

3.2. Contact angle measurements

The contact angle between a water drop supported on an external surface and the surface under investigation can be used to measure hydrophobicity (Khedkar et al., 2019). Figure 2 (a, b, c, d, and e) demonstrates the effect of environmental preparation on the contact angle and the variation in the contact angle of the aerogel samples for W1, W2, W3, W4, and W5. When adding HCl to resin W1 and W2, the contact angle increased, while the gel time took three times longer; this may help to complete the modification, resulting in a contact angle of 150.89° and a surface area of 961.1m^2/g. The contact angle for W2 was 147.89° and the surface area was 674.88m^2/g, as shown in Table 3. More transparency and a surface area of 790.49 m^2/g and a short gel time were found in the W3; because that particular sample was only TEOS. In terms of W4; without adding HCl to the resin, the contact angle was decreased. More overcast, small surface area, and lowest gel time were found in the W5 sample, as well as a light weight, despite a density of 0.04 g/cm^3 and a high contact angle of 152°. The reason is that sample was only sodium silicate containing sodium salts after it began to replace the hydroxide group attached to silicon with a chloride group, leading to a good modification process.

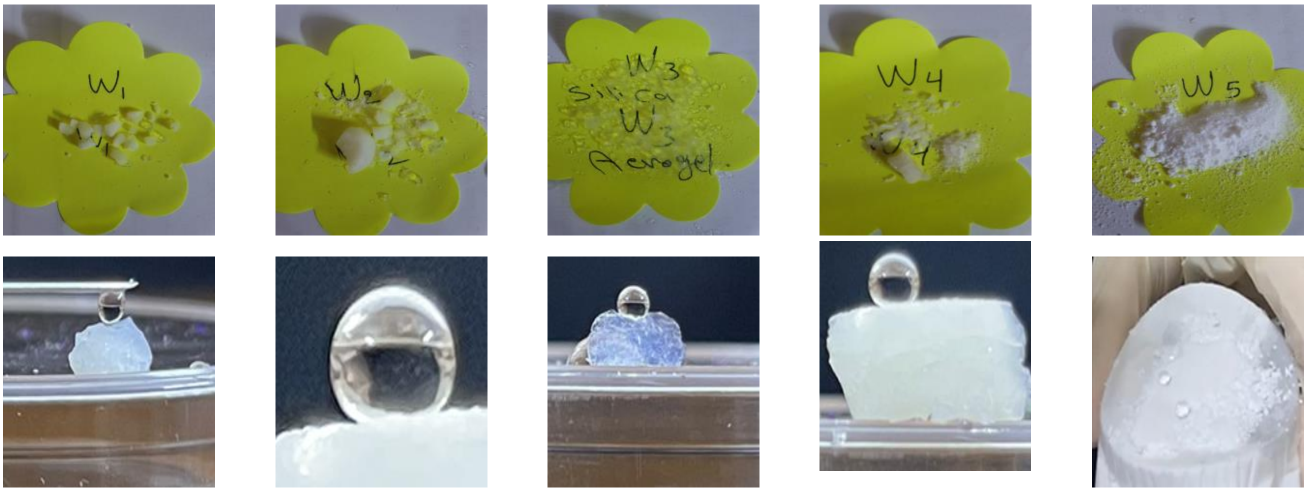

W1 W2 W3 W4 W5

Figure 2. The photographs of superhydrophobic aerogels for W1,W2 , W3, W4 and W5 samples

Table 3. Some of physical properties for silica aerogel prepared in different methods

Sample	Vm (cm^3/g)	Surface aera (m^2/g)	Total pore volume (cm^3/g)	Mean pore diameter (nm)	Average Particle size	Gel time min	Density g/cm^3	Contact angle
W1	158.78	961.1	2.23	12.941	38.618	120	0.156	150.89°
W2	155.06	674.88	2.2404	13.279	42.758	120	0.296	147.89°
W3	181.62	790.49	2.8498	14.42	43.23	15	0.096	138.70°
W4	159.1	692.47	1.67	9.6634	39.49	30	0.135	141.68°
W5	25.172	109.56	0.2962	10.815	53.648	10	0.04	152°

3.3. XRD analysis

Figure 3 depicts the X-Ray Ddiffraction of the samples (W1, W2, W3, W4, and W5). The size granule estimates for each sample are shown in Table 4. The difference between W1W2 and W4 is the addition of HCl to sodium silicate before it makes the ionic exchange and the difference between W1 and W2 in the way of washing. This means that the stimulation of cation resin plays an important role in making an amorphous sample similar to the silica aerogel from TEOS parcourse, as shown in samples W2 and W4, which indicate an amorphous structure with a broad band at 2θ between 22-34 degrees, and for W4 at 2θ between 18-28 degrees.

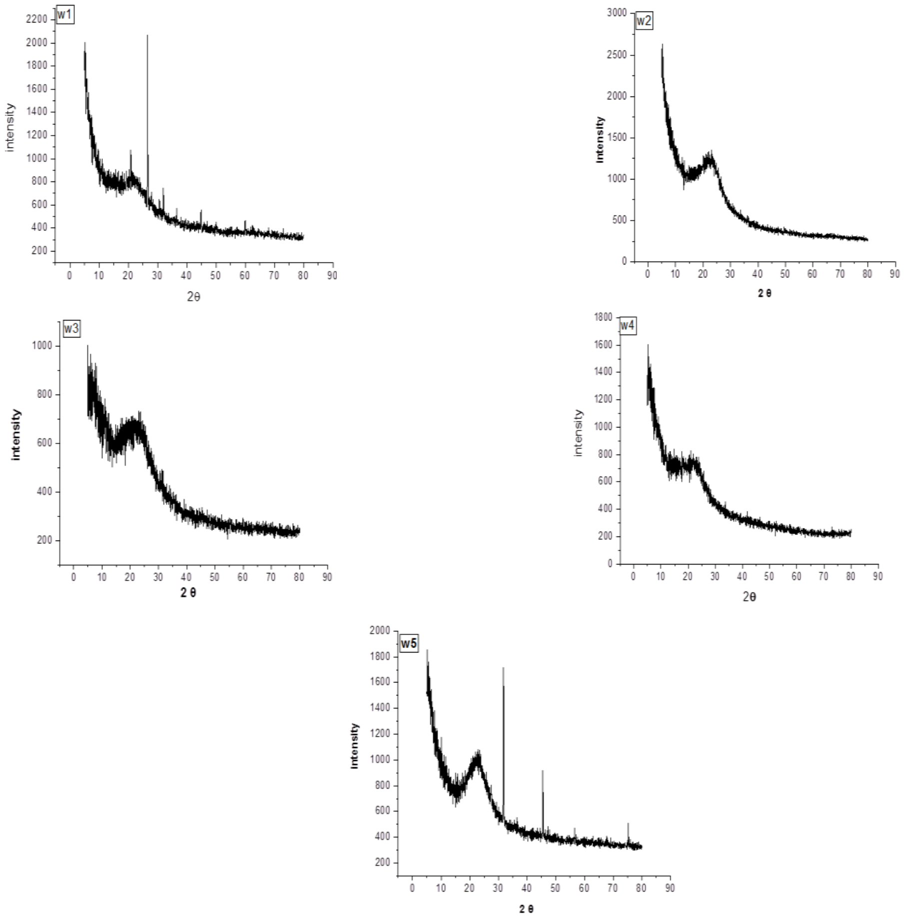

Figure 3. XRD diagram for W1, W2, W3, W4 and W5 silica aerogel prepared in different methods

Table 4. FWHM and grain size for W1, W2, W3, W4 and W5 silica aerogel

	2θ	Height	FWHM	Grain size
W1	20.82	196	0.06	23.49
	26.599	1195	0.11	12.95
	30.56	100	0.08	17.97
	31.97	221	0.08	18.08
	36.54	106	0.06	24.35
	39.50	40	0.1	14.72
	40.2	29	0.1	14.87
	42.5	29	0.2	7.435
	44.86	166	0.08	18.75
	45.95	46	0.1	15.06
	50.1	31	0.3	5.104
	59.96	99	0.11	14,55
W3	0.1767	8	111	229
	0.1769	8	56	23.0
	23	40	3	0.47
W5	27.32	56	0.05	28.87
	31.70	944	0.089	16.07
	45.48	471	0.143	10.51
	56.49	104	0.10	15.75
	75.27	171	0.09	19.46

DOI:https//doi.org/10.22452/mjs.vol42no2.7

3.4. BET analysis

Figure 4 depicts the linear N2 adsorption-desorption isotherm plots for aerogel samples prepared using various approaches. In most mesoporous to microporous materials, a hysteresis loop is present, which is linked to capillary condensation and evaporation in the mesopores. It was observed that the W1 and W2 samples have well-defined cylindrical pore channels of the H1 type. The surface area of silica aerogel appears to be enormous at 961.1 m^2/g based on the BET measurement of sample W1. It is likely that the observation is attributable to the sample's pore volume of 2.359 cm^3/g. W2 is 674.88 m^2/g because of the pore volume of 2.240 cm^3/g of the pores found in the taster (Israa F AL-Sharuee, 2021). Meanwhile, it seems that samples W3 and W4 may be categorized as H2 type disordered pores (pore blocking) percolation phenomena, which are related to the surface part of the silica aerogel. This appears that based on the BET analysis of sample W3. Sample W5 has a pore volume of 2.848 cm^3/g and a surface area of 790.4 m^2/g, and belongs to the H3 category, which consists of non-rigid aggregates of plate-like particles (slit-shaped pores). The silica aerogel looks to have a small surface area, since it is merely sodium silicate at 109.56 m^2/g. It is not as dense as other samples. It is possible that the observation is the result of increased pore volume and density (Pan et al., 2017; Shao, Luo, Cheng, & Zhang, 2013).

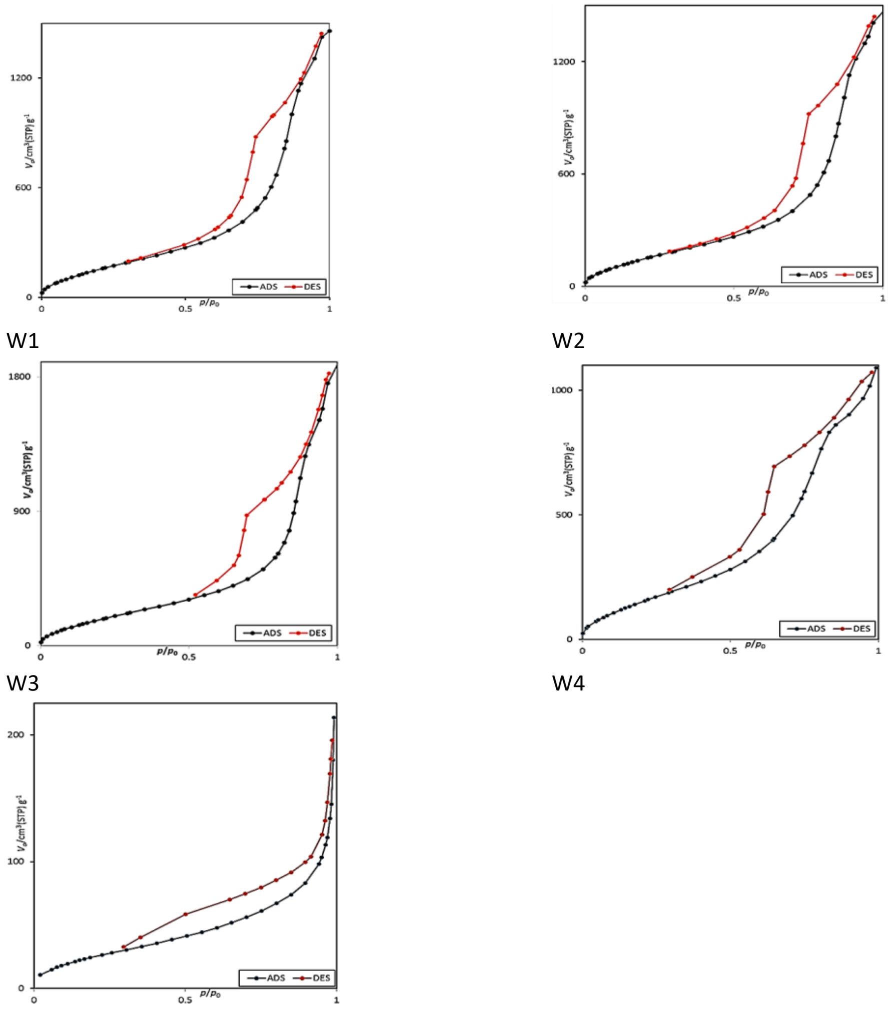

W1

W2

W3

W4

W5

Figure 4. N2 adsorption–desorption isotherms for W1, W2,W3,W4 and W5 samples

3.5. FE-Scanning Electron Microscopy and EDS images

Figure 5 depicts the FE-SEM and EDS images for the W1, W2, W3, W4 and W5 samples. In 200 nm of FE-SEM, the microstructure of sample W1 contains a continuous and extensively cross-linked network, resulting in an extremely open structure with individual particles that cannot be separated and an average particle size of 38.618 nm. The microstructure of W2 indicates that the particles are aggregations with a smooth surface form. The silica aerogel features a three-dimensional network and a small ball shape. Furthermore, microstructural homogeneity was observed, with the average particle count in sample W3 being 42.758nm. The microstructure of sample W3 appeared to be clusters of silica aerogel, and the particles were packed together with a smooth surface. There was also microstructural inhomogeneity, with the average particle size of the sample being 34.23 nm. At W4, the silica aerogel's fracture structure comprises highly branched clusters of smaller particles. The large pores can be seen rising from the fracture surface; there are no aggregations, and the surface is rough. In addition, the sample had no microstructural homogeneity, and the average particle count was 38.618 nm. Finally, the silica aerogel in sample W5 resembles tree blooms; the particles are also aggregations, and the surface was smooth. Furthermore, the sample had microstructural inhomogeneity because of sodium silicate, which is a minor part of its structure, with an average particle count of 53.648 nm.

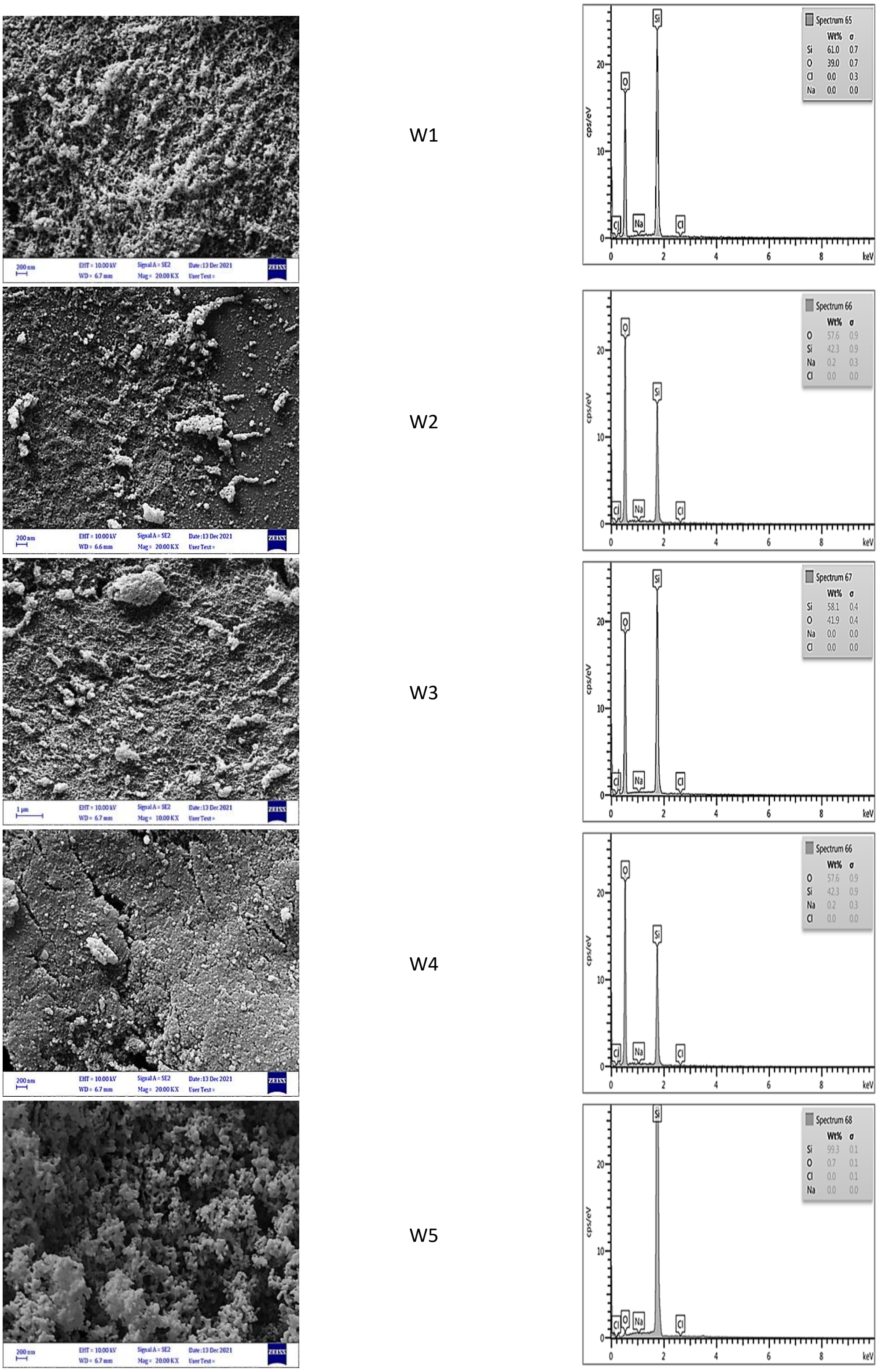

Figure 5. FESEM image for for W1, W2, W3, W4 and W5 samples

DOI:https//doi.org/10.22452/mjs.vol42no2.7

4. Conclusion

Numerous parameters influence silica aerogel properties. Precursors are crucial in the production of aerogel, and the low cost and safety are the primary reasons for using sodium silicate as a precursor in this work. The control of production procedures results in a superhydrophobic aerogel with a low surface area, microstructural integrity, low density, and low gel time. This leads to obtaining silica aerogel from sodium silicate with the best specifications at the lowest cost and time.

5. Acknowledgement

The authors would like to sincerely acknowledge, Mustansiriyah University. Also, many thanks to Ibin-Sina center of scientific examinations, Phi Nano-Science Center (PNSC), to help and supported.

6. References

Aegerter, M. A., Leventis, N., & Koebel, M. M. (2011). Aerogels handbook: Springer Science & Business Media.

Al-Mothafer, Z., & Abdulmajeed, I. (2021). Comparative study in use sodium silicate instead of NH 4 OH as an alkaline basic catalyst to gelation unmodified silica aerogel based on tetraethoxysilane (TEOS). Journal of Ovonic Research, 17(4).

Al-Mothafer, Z., Abdulmajeed, I., & Al-Sharuee, I. (2021). effect of oxalic acid as a catalyst and dry control chemical additive (dcca) for hydrophilic aerogel base sodium silicate by ambient pressure drying. Journal of Ovonic Research Vol, 17(2), 175-183.

Al-sharuee, I. F. (2019). Thermal Conductivity Performance of Silica Aerogel after Exposition on Different Heating under Ambient Pressure. Baghdad Science Journal, 16(3 (Suppl.)), 0770-0770.

AL-Sharuee, I. F. (2021). Specifications study of Hydrophobic Silica Aerogel Doped with Rhodamine 6G Prepared via Sub-Critical Drying Technique. Iraqi Journal of Science, 483-489.

Al-sharuee, I. F., & Mohammed, F. H. (2019). Investigation study the ability of superhydrophobic silica to adsorb the Iraqi crude oil leaked in water. Paper presented at the IOP Conference Series: Materials Science and Engineering.

Bhagat, S. D., Kim, Y.-H., Suh, K.-H., Ahn, Y.-S., Yeo, J.-G., & Han, J.-H. (2008). Superhydrophobic silica aerogel powders with simultaneous surface modification, solvent exchange and sodium ion removal from hydrogels. Microporous Mesoporous Materials, 112(1-3), 504-509.

Bhagat, S. D., & Rao, A. V. (2006). Surface chemical modification of TEOS based silica aerogels synthesized by two step (acid–base) sol–gel process. Applied Surface Science, 252(12), 4289-4297.

Cheng, Y., Xia, M., Luo, F., Li, N., Guo, C., & Wei, C. s. (2016). Effect of surface modification on physical properties of silica aerogels derived from fly ash acid sludge. Colloids Surfaces A: Physicochemical Engineerin Aspects, 490, 200-206.

Daniel, C., Longo, S., Ricciardi, R., Reverchon, E., & Guerra, G. (2013). Monolithic nanoporous crystalline aerogels. Macromolecular rapid communications, 34(15), 1194-1207.

Dorcheh, A. S., & Abbasi, M. (2008). Silica aerogel; synthesis, properties and characterization. Journal of materials processing technology, 199(1-3), 10-26.

Durães, L., Ochoa, M., Rocha, N., Patrício, R., Duarte, N., Redondo, V., & Portugal, A. (2012). Effect of the drying conditions on the microstructure of silica based xerogels and aerogels. Journal of nanoscience nanotechnology, 12(8), 6828-6834.

Feng, Q., Chen, K., Ma, D., Lin, H., Liu, Z., Qin, S., . . . Aspects, E. (2018). Synthesis of high specific surface area silica aerogel from rice husk ash via ambient pressure drying. Colloids Surfaces A: Physicochemical Engineering spects, 539, 399-406.

He, S., & Chen, X. (2017). Flexible silica aerogel based on methyltrimethoxysilane with improved mechanical property. Journal of Non-Crystalline Solids, 463, 6-11.

He, S., Huang, Y., Chen, G., Feng, M., Dai, H., Yuan, B., & Chen, X. (2019). Effect of heat treatment on hydrophobic silica aerogel. Journal of Hazardous materials, 362, 294-302.

Huang, Y., He, S., Feng, M., Dai, H., Pan, Y., & Cheng, X. (2019). Organic solvent-saving preparation of water glass based aerogel granules under ambient pressure drying. Journal of Non-Crystalline Solids, 521, 119507.

Khedkar, M. V., Somvanshi, S. B., Humbe, A. V., & Jadhav, K. (2019). Surface modified sodium silicate based superhydrophobic silica aerogels prepared via ambient pressure drying process. Journal of Non-Crystalline Solids, 511, 140-146.

DOI:https//doi.org/10.22452/mjs.vol42no2.7

Li, M., Jiang, H., Xu, D., Hai, O., & Zheng, W. J. J. o. N.-C. S. (2016). Low density and hydrophobic silica aerogels dried under ambient pressure using a new co-precursor method. 452, 187-193.

Mazrouei-Sebdani, Z., Salimian, S., Khoddami, A., & Shams-Ghahfarokhi, F. (2019). Sodium silicate based aerogel for absorbing oil from water: the impact of surface energy on the oil/water separation. Materials Research Express, 6(8), 085059.

Monshi, A., Foroughi, M. R., & Monshi, M. R. (2012). Modified Scherrer equation to estimate more accurately nano-crystallite size using XRD. World J Nano Sci Eng, , 2: 154, 160.

Nguyen, B. N., Meador, M. A. B., Medoro, A., Arendt, V., Randall, J., McCorkle, L., & Shonkwiler, B. (2010). Elastic behavior of methyltrimethoxysilane based aerogels reinforced with tri-isocyanate. ACS Applied Materials Interface, 2(5), 1430-1443.

Pan, Y., He, S., Cheng, X., Li, Z., Li, C., Huang, Y., & Gong, L. (2017). A fast synthesis of silica aerogel powders-based on water glass via ambient drying. Journal of Sol-Gel Science Technology, 82(2), 594-601.

Sarawade, P. B., Kim, J.-K., Hilonga, A., & Kim, H. T. (2010). Production of low-density sodium silicate-based hydrophobic silica aerogel beads by a novel fast gelation process and ambient pressure drying process. Solid State Sciences, 12(5), 911-918.

Shao, Z., Luo, F., Cheng, X., & Zhang, Y. (2013). Superhydrophobic sodium silicate based silica aerogel prepared by ambient pressure drying. Materials Chemistry, 141(1), 570-575.

Shi, M., Tang, C., Yang, X., Zhou, J., Jia, F., Han, Y., & Li, Z. (2017). Superhydrophobic silica aerogels reinforced with polyacrylonitrile fibers for adsorbing oil from water and oil mixtures. RSC advances, 7(7), 4039-4045.

Shirtcliffe, N., McHale, G., Newton, M., & Perry, C. (2003). Intrinsically superhydrophobic organosilica sol− gel foams. Langmuir, 19(14), 5626-5631.

Wagh, P., Ingale, S., & Gupta, S. C. (2011). New technology for rapid processing and moulding of silica aerogel materials in prescribed shapes and sizes and their characterization. Journal of sol-gel science technology, 58(2), 481-489.

Wang, J., Zhang, Y., Wei, Y., & Zhang, X. (2015). Fast and one-pot synthesis of silica aerogels via a quasi-solvent-exchange-free ambient pressure drying process. Microporous Mesoporous Materials, 218, 192-198.

Wang, X.-D., Sun, D., Duan, Y.-Y., & Hu, Z.-J. (2013). Radiative characteristics of opacifier-loaded silica aerogel composites. Journal of non-crystalline solids, 375, 31-39.

Wingfield, C., Franzel, L., Bertino, M. F., & Leventis, N. (2011). Fabrication of functionally graded aerogels, cellular aerogels and anisotropic ceramics. Journal of Materials Chemistry, 21(32), 11737-11741.

Zhang, X., Chen, Z., Zhang, J., Ye, X., & Cui, S. (2021). Hydrophobic silica aerogels prepared by microwave irradiation. Chemical Physics Letters, 762, 138127.

Zhao, Y., Li, Y., & Zhang, R. (2018). Silica aerogels having high flexibility and hydrophobicity prepared by sol-gel method. Ceramics International, 44(17), 21262-21268.

Zhou, B., Shen, J., Wu, Y., Wu, G., & Ni, X. (2007). Hydrophobic silica aerogels derived from polyethoxydisiloxane and perfluoroalkylsilane. Materials Science Engineering: C, 27(5-8), 1291-1294.

MALAYSIAN JOURNAL OF SCIENCE
MJS
ISSN 1394-3065

Regular Issue

Malaysian Journal of Science 42 (2): 56-61 (June 2023)
https://mjs.um.edu.my

ANNUAL EFFECTIVE DOSE ESTIMATION DUE TO THE NATURAL RADIOACTIVITY IN YAM TUBERS (*Dioscorea rotundata*) CULTIVATED IN NORTHCENTRAL NIGERIA

Matthew Tikpangi Kolo[1a]*, Oyeleke Ismail Olarinoye[2a], Simon Olonkwoh Salihu[3b], Hauwau Kulu Shuaibu[4c] and Funmilayo Ayedun[5d]

Abstract: Yam tubers (*Dioscorea rotundata*) and soil from commercially cultivated farmland in northcentral Nigeria were collected and investigated for their natural radioactivity content using a 3” × 3” NaI(Tl) gamma detector. Average activities of ^{238}U, ^{232}Th and ^{40}K in the investigated farm soil were 38.13±3.76 Bq kg^{-1}, 15.06±0.99 Bq kg^{-1} and 381.80±15.50 Bq kg^{-1}, respectively. The results agree with the world’s acceptable levels of safety. Activities measured in the yam tubers were in the range from BDL -76.68±9.73 Bq kg^{-1} for ^{238}U, BDL -19.77±1.30 Bq kg^{-1} for ^{232}Th and 312.50±20.73 - 627.94±38.37 Bq kg^{-1} for ^{40}K, with average values of 29.23±4.0, 13.10±0.72 and 445.10±27.20 Bq kg^{-1}, respectively. The total effective dose from radionuclide intake from yam ingestion fluctuated between 272.12 µSv y^{-1} and 935.97 µSv y^{-1}. Correlation analysis identified ^{238}U and ^{232}Th as the leading contributors to the total effective dose from ingesting yam tubers cultivated in northcentral Nigeria.

Keywords: *Natural radioactivity, yam tubers, NaI(Tl) detector, committed effective dose, northcentral Nigeria*

1. Introduction

The soil-plant-man ingestion route is a significant environmental pathway for human exposure to radiation. Radiological contamination of the human food chain can occur by radionuclide absorption through plant roots and uninterrupted intake of contaminated farm products, water and critter. Contamination can also occur when radionuclides are directly deposited on plant leaves (Gregory & Agbalagba, 2014; IAEA, 2010). Applying fertilisers for bountiful crop yield could also contaminate the food chain. According to Omoniyi et al. (2013), factors such as general agricultural practices, climatic conditions, soil characteristics, plant types and the physicochemical nature of the radioisotopes affect radionuclide uptake by the plant roots and subsequent deposition in the consumable plant parts. Naturally occurring radionuclides, 228Th and 238U, contribute to the radiation dose incurred from ingesting plants, animals, soil and water (Jwanbot et al., 2012). Ingested radionuclides from contaminated plants tend to enhance the total radiation dose deposited in various organs of the human body, posing radiological health challenge after a long period of exposure (Adesiji & Ademola, 2019; N. Jibiri et al., 2007). Therefore, it is important to maintain routine radiological investigations of agricultural products meant for human consumption to ensure their radiological safety and compliance with the ALARA principle.

Yam (Dioscorea rotundata) is an essential food crop that dominates the population diet in Nigeria. It is primarily cultivated in the northcentral part of Nigeria. Its capacity to be processed into different powder forms for human consumption and animal feeds has made it widespread among the Nigerian population. The Nigerian government has been giving considerable attention recently to the agricultural sector to diversify the national economy. The government aims to focus on yam production, processing and exportation for massive foreign exchange earnings. Hence, the need to comply with international safety protocols, especially from the radiation protection perspective regarding food crop export.

2. Materials and Methods

2.1 Sample Collection and Preparation

Northcentral Nigeria has been known as one of the regions with high potential for yam (*Dioscorea rotundata*) cultivation and production. The region does not just cultivate yam tubers for local consumption but also for exportation to boost the Nigerian economy. Eighteen (18) samples (YM 01 – YM 18) of cultivated yam tubers *(D. rotundata)* from a commercially cultivated yam farm were randomly collected for analysis. Also collected for

Authors information:
[a]Department of Physics, Federal University of Technology, Minna, Niger State, NIGERIA. Email: matthewkolo@futminna.edu.ng[1;] leke.olarinoye@futminna.edu.ng[2]
[b]Department of Chemistry, Federal University of Technology, Minna, Niger State, NIGERIA. Email: simon.salihu@futminna.edu.ng[3]
[c]Department of Physics, Nigerian Defence Academy, Kaduna, Kaduna State, NIGERIA. Email: drhks1618@gmail.com[4]
[d]Department of Physics, National Open University of Nigeria, Abuja, NIGERIA. Email: fayedun@noun.edu.ng[5]
*Corresponding Author: matthewkolo@futminna.edu.ng

Received: June 17, 2022
Accepted: January 25, 2023
Published: June 30, 2023

DOI:https//doi.org/10.22452/mjs.vol42no2.8

radiological analysis were the corresponding farm soil samples (SS 01 – SS 18), which were screened for all types of contamination at the collection site. Each collected yam and soil sample was carefully loaded into the sample bags and correctly designated for proper identification. The samples were then conveyed to the laboratory and further prepared for radiological analysis.

At the laboratory, yam samples were thoroughly cleaned with distilled water and dried under the sun for about 200 minutes to ensure the elimination of all surface moisture. Dried yam tubers were then peeled using a sharp kitchen knife. Portions meant for human consumption were cut into smaller sizes, rewashed with clean water, and sun-dried for 72 hours to remove all moisture from the samples. The samples were thoroughly powdered after drying and homogenized through a 2-mm sieve. Soil samples were also air-dried, pulverized, sieved and homogenized. Soil samples of 371.9±0.2 g each and yam samples of 180.8±0.1 g each were then packed into tightly closed designated containers and kept for about 32 days to ensure that long-lived parent radionuclides would reach radiological equilibrium with their decayed daughters (Asaduzzaman et al., 2014; UNSCEAR, 2000).

2.2 Sample Analysis

All the samples were analysed for their natural radioactivity by a 3″ × 3″ NaI(Tl) gamma-ray detector manufactured by Scintillation Technologies USA. A 6-cm thick lead house was used to shield the detector from any interference from external radiation. To effectively cancel out any spectral interference by unauthorized frequencies, the internal parts of the detector were coated with copper sheets. Gamma spectra from the detector were acquired and analysed using the ACCUSPEC computer program in the multichannel analyzer (MCA) attached to the detector. Standard calibration isotope sources (^{137}Cs and ^{60}Co) with an energy range of 200 keV-2.810 MeV were employed for energy and efficiency calibration of the detector before analysis. The surrounding radiation background was then determined by measuring an empty sample container with dimensions comparable to samples for 36000 seconds. Similarly, each sample (yam and farm soil) was measured for 36000 seconds. The activity concentration ^{214}Bi measured based on its γ-ray peak (1.760 MeV) was used to estimate ^{238}U in all the samples. Meanwhile, the ^{208}Tl activity concentration measured from its γ-ray peak (2.614 MeV) was used to evaluate ^{232}Th. The activity concentration of ^{40}K in all the samples was assessed based on the single characteristic gamma line measured at 1.460 MeV. The analysis was performed at Ladoke Akintola University of Science and Technology (LAUTECH), Ogbomosho, Nigeria.

The relative activities of ^{238}U, ^{232}Th and ^{40}K were calculated using the established formula (Khandaker *et al.*, 2012; Kolo *et al.*, 2015; Kolo *et al.*, 2020):

$$A(Bq\ kg^{-1}) = \frac{C}{\varepsilon_\gamma \times I_\gamma \times W} \qquad (1)$$

where A is the activity concentrations of radionuclides in the samples measured in Bq kg^{-1}, C is the net count rate measured as counts/sec, I_γ is the intensity of gamma-ray, ε_γ (E) is the detector photo-peak efficiency (%) and W is the weight of sample in kg.

Absorbed dose rate (D_R) in the air, which shows the degree of radiation risk for public exposure, was computed from the specific activities of ^{238}U, ^{232}Th and ^{40}K in the farm soils. D_R was computed using the relation formula (Ravisankar *et al.*, 2014; UNSCEAR, 2000):

$$D_R(nGy\ h^{-1}) = pA_U + qA_{Th} + rA_K \qquad (2)$$

where p is per unit dose rate of ^{238}U activity given for 4.27 × 10^{-10} Gy h^{-1}/Bq kg^{-1}, q is per unit dose rate of ^{232}Th activity given for 6.62 × 10^{-10} Gy h^{-1}/Bq kg^{-1}, and r is per unit dose rate of ^{40}K given for 0.43 × 10^{-10} Gy h^{-1}/Bq kg^{-1}. A_U, A_{Th}, and A_K express the activities of ^{238}U, ^{232}Th, and ^{40}K in Bq kg^{-1}, respectively. The dose rate in the air was converted to the effective dose, which represents the radiation vulnerability of an individual. This conversion was done using two conversion factors: (i) 0.7 Sv Gy^{-1}, which transforms Gy to Sv, to measure the biological effects of any given radiation dose to inflict damage in the human body tissue; (ii) the outdoor occupancy factor. Adejuwon (2002) reported that a typical Nigerian farmer spends 10 hours outdoors daily on average. Thus, an occupancy factor of 0.4 was adopted in this study for the computation of the effective dose rate.

2.3 Committed Effective Dose Rate from Ingesting Yam Tubers

The committed effective dose is a single parameter summarising the radiation dose of different radionuclides from various radioactive sources. The total dose of individual radionuclides residing in the organs of the human body gives a measure of radiological health incidences connected with ingesting the radioisotopes (Jibiri *et al.*, 2007). Radiation dose from ingestion is a product of specific activities (Bq kg^{-1}) in the ingested food and the mass of the food intake over a given period (kg/d or kg/y). Committed effective dose from ingestion can thus be computed by applying an appropriate transformation factor (Sv bq^{-1}). Ingested dose from the consumption of yam tubers was calculated using the following formula (Jibiri *et al.*, 2007; Till & Moore, 1988):

$$H_{T,r} = \left(U^{Bi}A_r^{Bi} + U^{Pf}A_r^{Pf} + U^{Mi}A_r^{Mi} + \cdots\right)g_{T,r} \qquad (3)$$

In summary, Eq (3) is written as

$$H_{T,r} = \sum\left(U^i A_r^i\right)g_{T,r} \qquad (4)$$

Where *i* indicates the food group, U^i is the rate of intake (Bq y^{-1}), A_r^i represents activity concentration of radionuclide r (Bq kg^{-1}) and $g_{T,r}$ is the dose constant for intake of radionuclide (r) in Sv Bq^{-1}. ICRP (1994, 1996) and RIFE (2005) give the g value of each radionuclide as 4.8 × 10^{-8} Sv Bq^{-1} (^{238}U), 2.3 × 10^{-7} Sv Bq^{-1} (^{232}Th) and 5.9 × 10^{-9} Sv Bq^{-1} (^{40}K). The annual ingestion rate of yam tubers in Nigeria is 75.15 kg y^{-1}, according to FOS (2006).

3. Results and Discussion

Activities of ^{238}U, ^{232}Th and ^{40}K in the cultivated farm soils and their computed total effective doses are presented in Table 1.

Table 1. Activities of ^{238}U, ^{232}Th, and ^{40}K in the cultivated farm soil and corresponding effective dose rates.

S. no	Sample ID	Activity concentrations (Bq kg^{-1})			Effective dose rate (µSv h^{-1})
		^{238}U	^{232}Th	^{40}K	
1	SS 01	14.26±1.74	20.25±1.20	383.75±12.29	0.010
2	SS 02	15.80±2.26	13.69±0.81	267.84±14.07	0.008
3	SS 03	70.55±4.70	16.98±0.53	436.93±22.92	0.017
4	SS 04	51.18±6.42	17.61±0.81	398.63±16.20	0.014
5	SS 05	32.50±4.08	18.51±1.10	395.79±19.72	0.012
6	SS 06	23.01±1.32	20.10±1.90	389.67±9.23	0.011
7	SS 07	47.40±5.88	9.89±0.59	331.24±17.36	0.011
8	SS 08	20.54±2.38	14.47±0.63	408.06±16.20	0.010
9	SS 09	49.04±6.15	11.73±0.70	422.83±22.20	0.013
10	SS 10	48.22±6.24	15.18±0.91	355.90±18.67	0.013
11	SS 11	44.81±4.41	21.69±1.25	398.16±5.10	0.014
12	SS 12	BDL	9.05±0.54	359.32±8.47	0.009
13	SS 13	88.73±1.83	10.39±0.50	360.00±18.85	0.017
14	SS 14	32.23±3.40	17.14±1.71	375.21±10.53	0.012
15	SS 15	8.39±1.27	16.79±0.99	387.38±20.26	0.009
16	SS 16	BDL	14.62±0.87	489.77±15.28	0.012
17	SS 17	33.24±4.20	9.78±0.58	388.86±20.45	0.010
18	SS 18	30.12±3.91	13.23±2.13	323.14±11.23	0.010
	Min	8.39±1.27	9.05±0.54	267.84±14.07	0.008
	Max	88.73±1.83	21.69±1.25	489.77±15.28	0.017
	Mean	38.13±3.76	15.06±0.99	381.80±15.50	

BDL, below detection unit

Activity concentration of ^{238}U fluctuated between 8.39±1.27 Bq kg^{-1} and 88.73±1.83 Bq kg$^{-1,}$ as seen in Table 1. Specific activities of ^{232}Th and ^{40}K ranged from 9.05±0.54 to 21.69±1.25 Bq kg^{-1} with an average of 15.06±0.99 Bq kg^{-1} and from 267.84±14.07 to 489.77±15.28 Bq kg^{-1} with a mean of 381.80±15.50 Bq kg^{-1}, respectively. These values are within the world's precautionary limits for safety, documented in the UNSCEAR (2000) report. Figure 1 shows ^{238}U, ^{232}Th and ^{40}K distribution in the cultivated soil expressed in %. Furthermore, the computed effective gamma dose rate varied from 0.008 to 0.017 µSv h^{-1}, which is lower than the global mean of 0.055 µSv h^{-1}, documented by the UNSCEAR (2000).

DOI:https//doi.org/10.22452/mjs.vol42no2.8

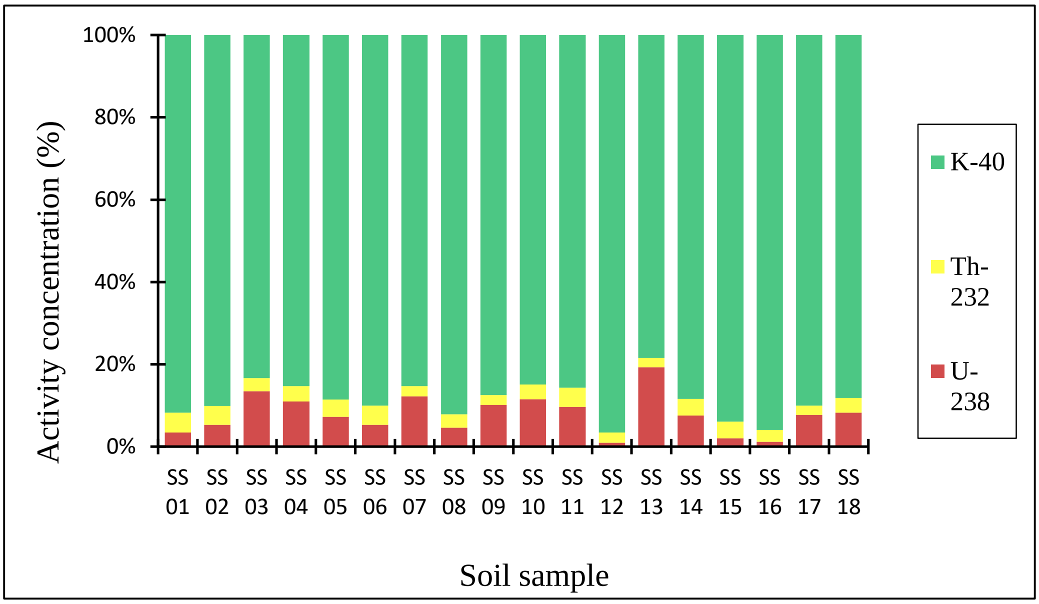

Figure 1. Percentage spread natural radionuclides in the cultivated farm soil.

Activities of ^{238}U, ^{232}Th and ^{40}K in the cultivated yam tubers *(D. rotundata)* are summarised in Table 2. Table 2 also shows the computed committed effective dose (CEDE) from the consumption of the cultivated yam tubers. Specific activities of ^{238}U in the cultivated yam tubers varied from BDL to 76.68±9.73 Bq kg^{-1}, while that of ^{232}Th was from BDL to 19.77±1.30 Bq kg^{-1}. The activity concentration values for ^{40}K ranged from 312.50±20.73 to 627.94±38.37 Bq kg^{-1}, with a mean value of 445.10±27.20 Bq kg^{-1}. Computed effective dose from radionuclides uptake from consuming cultivated yam tubers, shown in Table 2, ranged from 272.12 µSv y^{-1} to 935.97 µSv y^{-1}, with an average of 529.24 µSv y^{-1}. The calculated average is lower than the global safety threshold of 1.1 mSv y^{-1} (IARC, 2000) and natural exposure values of 2000 µSv y^{-1} reported by Jibiri *et al.* (2007). The discrepancies could be due to the various food processing and preparation methods. Nevertheless, the result agrees with the previously reported findings (Jibiri & Eke, 2021) for a study in the Niger Delta of Nigeria.

Table 2. Activities of ^{238}U, ^{232}Th and ^{40}K with the respective committed effective dose from consuming yam tubers.

S. no	Sample ID	Activity concentrations (Bq kg^{-1})			CEDE (µSv y^{-1})
		^{238}U	^{232}Th	^{40}K	
1	YM 01	11.77±1.64	7.73±0.46	438.31±38.37	370.41
2	YM 02	BDL	10.05±0.78	499.31±26.14	395.10
3	YM 03	72.24±8.49	14.06±0.84	627.94±32.77	782.02
4	YM 04	33.24±4.67	19.77±1.30	530.22±28.00	696.71
5	YM 05	12.75±1.74	14.31±0.85	484.54±30.41	508.17
6	YM 06	28.21±2.45	17.43±1.97	338.69±18.64	553.20
7	YM 07	37.19±4.82	8.13±0.49	460.56±23.99	478.88
8	YM 08	29.57±2.93	15.43±0.83	502.08±28.91	595.98
9	YM 09	25.92±3.73	BDL	502.49±26.35	316.30
10	YM 10	2.88±0.44	10.42±0.63	435.56±22.84	383.61
11	YM 11	BDL	13.02±0.78	312.50±26.83	363.60
12	YM 12	BDL	7.48±0.45	408.86±21.43	310.57
13	YM 13	15.66±5.41	22.04±4.23	370.03±22.10	601.50
14	YM 14	76.68±9.73	9.69±0.58	346.36±20.73	597.66
15	YM 15	BDL	BDL	446.36±28.50	BDL
16	YM 16	24.85±3.28	9.88±0.59	514.42±26.85	488.50

17	YM 17	15.14±2.08	13.64±0.81	494.88±25.87	509.80
18	YM 18	23.09±6.20	16.55±4.27	298.72±18.98	501.80
	Min	BDL	BDL	312.50±20.73	272.12
	Max	76.68±9.73	19.77±1.30	627.94±38.37	935.97
	Mean	29.23±4.0	13.10±0.72	445.10±27.20	529.24

BDL, below detection limit

Table 3 compares the results of this investigation with other findings from related investigations within Nigeria. The variations in these findings could be due to the use of chemical and organic fertilisers for bountiful crop yield by commercial farmers.

Table 3. Activities of ^{238}U, ^{232}Th and ^{40}K in cultivated yam tubers from different parts of Nigeria expressed as Bq kg^{-1}

Location	^{238}U	^{232}Th	^{40}K	Reference
Oguta, Niger-Delta	23.75 ±5.69	30.99 ±9.51	189.99 ±59.14	Jibiri & Eke (2021)
Plateau State	2.32 ± 0.62	3.24 ± 0.36	22.12 ± 2.34	Jwanbot *et al.* (2012)
Ondo State	4.67	3.07	81.87	Ibitola *et al.* (2018)
Osun State	1.72± 0.10	2.24 ± 0.21	37.84 ± 2.40	Nwankpa (2017)
Onne, Rivers State	6.3±1.8	8.4±2.6	227. ±27.3	Gregory & Agbalagba (2014)
Ogun State	9.60± 0.49	ND	490.67 ±43.35	Jibiri & Abiodun (2012)
Minna, North Central	29.23 ±4.0	13.10 ±0.72	445.10 ±27.20	Present study

Natural relationships and suggested interdependency likely to occur between radiation parameters in the cultivated yam tubers were assessed based on Pearson's correlation using a Statistical software package, Statistical Program for Social Science (SPSS 22.0). The computed correlation metrics are shown in Table 4.

Table 4. Correlation metrics between radiation contents of the yam samples

Variables	^{238}U	^{232}Th	^{40}K	CEDE
^{238}U	1.00			
^{232}Th	0.17	1.00		
^{40}K	0.23	-0.15	1.00	
CEDE	0.68	0.76	0.24	1.00

Table 4 shows a strong positive correlation between ^{238}U (r = 0.68) and ^{232}Th (r = 0.76) and the respective CEDE. Table 4 also shows a weak correlation (r = 0.24) between ^{40}K and CEDE. These findings suggest that ^{238}U and ^{232}Th are the main contributors to the total effective dose from ingesting yam tubers cultivated in the northcentral Nigeria.

4. Conclusion

This paper presents the radiological data of yam tubers grown commercially in the Northcentral of Nigeria. A 3" × 3" NaI(Tl) gamma-ray detector determined the primordial radionuclide composition of the yam tubers. The equivalent committed effective dose due to radionuclides incorporation into the human body from consuming the cultivated yam tubers was also computed. The average activity of ^{238}U was 29.23±4.0 Bq kg^{-1}; ^{232}Th recorded an average activity of 13.10±0.72 Bq kg^{-1}; for 40K was 445.10±27.20 Bq kg^{-1}. The results of this investigation agree with the findings from other related investigations in some regions of Nigeria. Although correlation studies showed that ^{238}U and ^{232}Th are the significant contributors to total ingestion dose, computed ingestion dose from consumption of the yam tubers was proved relatively low, resulting in significant radiation incidence among the consumers. Therefore, cultivated yam tubers from northcentral Nigeria are radiologically fit and safe for local consumption and export. However, it is recommended that commercially grown and cultivated food crops be checked and monitored continually to mitigate radiation-induced health incidences arising from continuous consumption and ensure strict compliance with the ALARA safety protocol.

5. Acknowledgement

The authors are highly indebted to the staff and management of Ladoke Akintola University of Science and Technology Ogbomosho (LAUTECH), Nigeria.

6. References

Adejuwon, C. (2002). Introduction to Crop Taxonomy, Anatomy and Physiology: Ibadan University Press, Nigeria.

Adesiji, N., & Ademola, J. (2019). Soil-to-maize Transfer Factor of Natural Radionuclides in a Tropical Ecosystem of Nigeria. *Nigeria Journal of Pure and Applied Physics, 9*(1), 6-10.

Asaduzzaman, K., Khandaker, M. U., Amin, Y. M., Bradley, D. A., Mahat, R. H., & Nor, R. M. (2014). Soil-to-root vegetable transfer factors for 226Ra, 232Th, 40K, and 88Y in Malaysia. *Journal of Environmental Radioactivity, 135*(0), 120-127.

FOS. (2006). Federal Office of Statistics, Nigeria. Compilation of FOS/FAO annual consumption data/food balance sheet of Nigeria. A publication of Federal Office of Statistics (FOS), Nigeria.

Gregory, A. O., & Agbalagba, E. (2014). Assessment of natural radioactivity, associated radiological health hazards indices and soil-to-crop transfer factors in cultivated area around a fertilizer factory in Onne, Nigeria. *Environmental earth sciences, 71*(4), 1541-1549.

IAEA. (2010). Handbook of parameter values for the prediction of radionuclide transfer in terrestrial and freshwater environments. International Atomic Energy Agency, Vienna.

IARC. (2000). (International Agency for Research on Cancer). IARC Monographs on the evaluation of carcinogenic risks to humans. Ionizing Radiation, Part 1: x- and γ-radiations and neutrons, 75.

Ibitola, A., Gilbert, A. O., Ilori, A. O., Aremu, R., & Omosebi, I. (2018). Measurement of (40 K, 238 U and 232 Th) and associated dose rates in soil and commonly consumed foods (vegetables and tubers) at Okitipupa, Ondo State, Southwestern Nigeria. *Asian Journal of Research and Reviews in Physics, 1*(1), 1-11.

ICRP. (1994). Dose co-efficient for the intakes of radionuclides by workers. Pergamon Press, Oxford, ICRP Pub. No. 68.

ICRP. (1996). Age-dependent Doses to Members of the Public from intakes of radionuclides: Part 5. Compilation of Ingestion andInhalation Dose Co-efficients. Pergamon Press, Oxford, ICRP Pub. No. 72.

Jibiri, N., Farai, I., & Alausa, S. (2007). Estimation of annual effective dose due to natural radioactive elements in ingestion of foodstuffs in tin mining area of Jos-Plateau, Nigeria. *Journal of Environmental Radioactivity, 94*(1), 31-40.

Jibiri, N. N., & Abiodun, T. H. (2012). Effects of food diet preparation techniques on radionuclide intake and its implications for individual ingestion effective dose in Abeokuta, Southwestern Nigeria.

Jibiri, N. N., & Eke, B. C. (2021). Radionuclide contents in yam samples and health risks assessment in Oguta oil producing locality Imo State Nigeria. *INTERNATIONAL JOURNAL, 2766*, 2748.

Jwanbot, D., Izam, M., & Nyam, G. (2012). Radioactivity in some food crops from high background radiation area on the Jos-Plateau, Nigeria. *Journal of Natural Sciences Research, 2*(6), 76-78.

Khandaker, M. U., Jojo, P., Kassim, H., & Amin, Y. (2012). Radiometric analysis of construction materials using HPGe gamma-ray spectrometry. *Radiation Protection Dosimetry, 152*(1-3), 33-37.

Kolo, M., Aziz, S., Khandaker, M., Asaduzzaman, K., & Amin, Y. (2015). Evaluation of radiological risks due to natural radioactivity around Lynas Advanced Material Plant environment, Kuantan, Pahang, Malaysia. *Environmental Science and Pollution Research, 22*(17), 13127-13136.

Kolo, M. T., Gomina, M., Awojoyogbe, B., & Olarinoye, O. (2020). Artisanal Gold Mining Activity in Northcentral Nigeria and Its Implications: Radiological Approach. *Journal of Nuclear Technology in Applied Science, 8*(1), 97-111.

Nwankpa, A. C. (2017). Determination of food crops contamination in Osun State, Nigeria due to radium-226, thorium-232 and potassium-40 concentrations in the environment. *European Journal of Sustainable Development, 6*(4), 169-169.

Omoniyi, I. M., Oludare, S., & Oluwaseyi, O. M. (2013). Determination of radionuclides and elemental composition of clay soils by gamma-and X-ray spectrometry. *Springerplus, 2*(1), 1-11.

Ravisankar, R., Vanasundari, K., Suganya, M., Raghu, Y., Rajalakshmi, A., Chandrasekaran, A., Sivakumar, S., Chandramohan, J., Vijayagopal, P., & Venkatraman, B. (2014). Multivariate statistical analysis of radiological data of building materials used in Tiruvannamalai, Tamilnadu, India. *Applied Radiation and Isotopes, 85*(0), 114-127.

RIFE. (2005). Radioactivity in Food and Environment. The Centre for Environment, Fisheries and Aquaculture Science (CEFAS). 2004 Report, RIFE-10

Till, J. E., & Moore, R. E. (1988). A pathway analysis approach for determining acceptable levels of contamination of radionuclides in soil. *Health Physics, 55*(3), 541-548.

UNSCEAR. (2000). Sources and Effects of Ionizing Radiation. Report to General Assembly, with Scientific Annexes. United Nations, New York.

DOI:https//doi.org/10.22452/mjs.vol42no2.8

MALAYSIAN JOURNAL OF SCIENCE
MJS
ISSN 1394-3065

Regular Issue

Malaysian Journal of Science 42 (2): 62-66 (June 2023) https://mjs.um.edu.my

THE STRUCTURE OF THERMOLUMINESCENCE TRAPS IN AQUEOUS GROWN KCl

Ruchi Pandey[1a], Rajendra Kumar[2a]*, Sumit Tiwari[3b], S. D. Pandey[4c]

Abstract: The results of TL studies in aqueous grown undoped KCl crystals are reported. A de-convolution of TL curve into five component peaks has been performed and trap depths have been obtained. The importance of bi-vacancy has been established as a fundamental trap and its anion vacancy end has also been proposed as a suitable trap for thermoluminescence in KCl crystals. The traps at anion vacancies linked to impurity vacancy I-V pairs have also been envisaged and the shift in the depths of traps is attributed to the electric field of I-V pairs in the lattice caused by inherent divalent ions. Some traps linked to hydroxyl groups have also been identified.

Keywords: *Traps, TL, bi-vacancy, I-V pair. stark effect, hydroxyl groups*

1. Introduction

A trap, in general, implies an imperfection in the regular spacing of atoms / ions that make up the solid. It can capture and immobilize an electron or hole and prevent its recombination with the carriers of opposite charge as electron- hole pair. Electrons and holes may break free traps quickly, or they may remain there for an extended period. The charge carriers can be released from traps by irradiating the solid with light or by heating it. Traps play a major role in photo conductance, luminescence and also operation of various electronic devices.

Thermoluminescence (TL) involves exciting electrons in traps to the conduction band on heating, and these finally drop to traps or recombination centers (Bos, 2006; Srivastava, 2008). Even if recombination occurs without the electron reaching the conduction band, the requirement of trap is quite necessary to observe the phenomenon of TL. Further, electrons must stay in the traps for sufficient time.

No study seems to be available to discuss the structure of traps even in an elementary system like KCl. In an earlier work TL is reported in pure and impurity doped KBr and NaCl crystals (Mehendru & Radhakrishna, 1969). So far KBr system is concerned, the peaks at 90°C and 150 °C are assigned to first and second type of F-centers respectively for pure as well as doped crystals. But the structure of such centers is not described. Further, TL studies are reported in suprapure RbBr (Sastry & Sapru, 1979). Two prominent peaks were observed by these workers but no explanation is provided about the structure of corresponding traps. Further, TL studies are available in a number of alkali halides (Deshmukh and Moharil, 1985) without any specific information about the structure of traps.

Other pioneers in the field (Jain and Mehendru, 1965) report two types of defects in pure KCl, giving TL peaks at 135°C and 190°C, but again structure of traps has not been elucidated. TL studies are further provided for Harshaw KCl crystals irradiated with gamma rays (Austin and Alvarez Rivas, 1972) and the role of F-centers as recombination centers is reported in annealing process. Optical and thermoluminescence properties of a NaCl crystal doped with cadmium and manganese ions and exposed to gamma rays are recently reported (Ortiz et.al, 2007). These workers have indicated the role of interstitial defects in creating thermoluminescence through recombination with vacancies. Some headway about the nature of defects for TL is however sought (Benia et. al, 2010; Wosinski, 1989) and TL traps seem to be situated near dislocation sites in the lattice.

Few workers of our group (Pandey et. al, 2017) have reported the importance of bi-vacancy traps in alkali halide crystals through a comparison of TL spectra in nominally pure KCl and that with large manganese content. A theoretical model has also been developed (Pandey et.al, 2021) to highlight the importance of bi vacancy traps in alkali halides.

In the present work, we have made fresh TL studies in undoped KCl crystals grown through aqueous technique. The importance of bi-vacancy is further established. The effect of impurity-vacancy (I-V) pairs in affecting the trap depths is put forth. Further, the role of hydroxyl groups in causing large trap depth centers is highlighted.

Authors information:
[a]Physics Department, Rama University, Mandhana, Kanpur-209217, INDIA. E-mail: ruchi.pande@gmail.com[1]; rajendrab25@gmail.com[2]
[b]Department of Physics, School of Physical and Decision Sciences, Babasaheb Bhimrao Ambedkar University, Lucknow-226025, INDIA. E-mail: contactsumit2409@gmail.com[3]
[c]P.P.N.P.G Center, Kanpur University, The Mall, Kanpur - 208001, INDIA. E-mail: sdpandey41@gmail.com[4]
*Corresponding Author: rajendrab25@gmail.com

Received: March 31, 2022
Accepted: November 1, 2022
Published: June 30, 2023

DOI:https//doi.org/10.22452/mjs.vol42no2.9

2. Role of Traps In Tl

2.1 Importance of bi-vacancy

The prominent point defects in alkali halides like KCl are of Schottky type i.e. cation and anion vacancies. These should be produced in equal numbers in a KCl crystal, and could further combine to form cation-anion vacancy pairs, also called a bi-vacancy and equilibrium would be maintained between Schottky pairs and bi-vacancies. When an alkali halide crystal is doped with divalent impurities, additional cation vacancies will be created for local charge neutrality. In KCl crystal doped with divalent cations an anion vacancy has two options, it could combine with a free cation vacancy to form a bi-vacancy or else link with cation vacancy end of I-V pair. The increase in concentration of I-V pairs due to doping would lead to more anion vacancies getting linked to I-V pairs through their cation vacancy end. The doping of divalent cations would thus decrease the relative concentration ofbarebi-vacancies in an alkali halide. Such a process would proceed effectively during growth of crystals from aqueous solution, wherein the growth takes place at a constant temperature. Such a situation may not be possible in melt grown crystals where growth takes place in a temperature gradient. The decrease in concentration of bivacancy in KCl crystals with appreciable manganese impurity content has actually been verified (Pandey et al., 2017).

A number of workers (Gourary and Adrian, 1957; Herman and Barnett, 1982) were involved in theoretical estimation of energy levels of electrons trapped at anion vacancy sites in alkali halide crystals e.g. NaCl, KCl. Rb Cland KBr etc. with face centered cubic structure. In such crystals positive cations and negative anions are alternately arranged in three dimensional pattern.Fig.1 shows such as arrangement in (001) plane of KCl lattice.

The energies of the levels 1s, 2p and 2s of electron trapped at anion vacancy have been theoretically calculated (Herman and Barnett, 1982). They found the energy of 2s level to be close to the conduction band as -0.277 eV in KCl. Earlier, other workers (Gourary and Adrian, 1957) estimated only two bound states for F-center. Recently, through DFT calculations in a different context it is reported that an s-state of F-center (anion vacancy) in KCl is close to the conduction band (Hoya et al., 2017).

A vacancy-pair as above is a suitable trap for electrons in KCl lattice and helps in forming a cation vacancy coupled F- center. The electrons of such F-centers would not be able to fall to the lower states as in a unique F-center (bare anion vacancy), because normal selection rules for electron transitions may not apply here. This breaking of selection rules is perhaps due to the fact that the field at the anion vacancy site of bi-vacancy is neither Columbic nor a constant spherical well type. So, a 2s level of such a TL center in KCl is likely to act as an ideal trap for electrons near the conduction band. The TL centers in such ideal traps will exist for a long time and participate in TL emission.

2.2 Role of I-V pairs

The I-V pairs could combine with anion vacancies to form an arrangement linking anion vacancy with ann (nearest neighbor) I-V pair or else with nnn (next nearest neighbor) I-V pair also termed as Z_1 center (Bushnell, 1964).

When a KCl crystal is irradiated with high energy radiation, electrons liberated could be trapped at free anion vacancy, anion vacancy end of bi-vacancy or at anion vacancy linked to I-V pair combination. The electron trapped at secluded anion vacancy is shown in Fig. 1(a) and that trapped at bi-vacancy is shown in Fig. 1(b). The Figs. 1(c) and 1(d) further describe the two arrangements of electron trapping at anions linked to differently placed I-V pairs.

In a divalent cation doped KCl, there would be plentiful I-V pairs in the lattice. Now if a doped KCl crystal is exposed to ionizing radiations to create F-centers, some of these F-centers would also be under the influence of the electric field of I-V pairs, whether nn or nnn type.

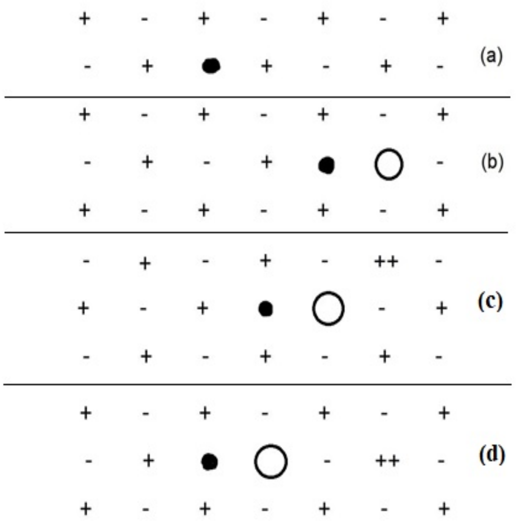

Figure 1. Arrangement of ions in (001) plane of KCl lattice. Alkali ions are shown as + and negative halide ions as -. The vacant sites are shown as circles. The electron occupying the defect is shown by a dot, possible defects being (a), (b), (c) and (d) viz. (a)secluded anion vacancy (b) bi-vacancy (c) anion vacancy linked to I-V pair at nn position and (d) anion vacancy linked to I-V pair in nnn position.

2.3 Increased depth of 2s level in bi-vacancy

A secluded anion vacancy cannot be a stable trap as the electron inside would decay via optical and phonon radiations. An anion-cation vacancy pair, also called bi-vacancy is however a suitable trap for electrons in KCl-like lattice which helps in forming a cation vacancy coupled anion vacancy F-center, as shown in Fig.1 (b). In our recent work (Pandey et. al.,2021), it has been theoretically estimated that if we consider a bi-vacancy instead of the single anion vacancy, the electrons in the trap are under the influence of a spheroidal well whose effective potential depth is reduced and simultaneously width is increased, as compared to that of a secluded anion vacancy. This change in the structure of defects is able to explain the observed TL trap depth values.

3. Effect of Internal Electric Field on Tl Center Levels

An impurity vacancy (I-V) dipole would exert an electric field at its neighborhood. In KCl containing divalent cations, there would be plentiful of I-V pairs. If I-V pairs are coupled to a TL center, its energy levels would be affected by the said internal electric field.

Assuming, electric field due to I-V pair to be uniform at the site of anion vacancy, its effect will be zero on the energy levels of electron at TL center, in first order perturbation theory. However, under second order perturbation theory quadratic field effects would be operative and non-zero correction to energy levels are expected (Davydov, 1965). Such a situation would arise for TL center perturbed by internal electric field of I-V pair as per Figs. 1(c) and 1(d).

Now, if an F- center were exactly hydrogen like, its 2s and 2p levels would be degenerate and this condition would lead to creation of three levels under electric field. However, the real situation is different. The site potential over a secluded anion vacancy center is not spherically symmetric but is octahedral due to the effect of charges in the neighborhood in an alkali halide lattice. Nevertheless earlier workers (Herman and Garnett, 1982) obtained certain conclusions about energy levels of F- center.

The 2s and 2p levels are not degenerate in a F- center and the effect of internal electric field (F) has to be considered. In second order perturbation theory (Davydov, 1965), the effect of relevant 2s level would be

$$\frac{< 2s|ezF|2p_o >< 2p_o|ezF|2s >}{E(2s) - E(2p_o)}$$

where the symbols have their usual meanings and $2p_o$ is the 2p level component for m=0 and does contribute to energy shift. The m = ±1, 2p levels do not contribute to all, due to selection rules. The hydrogen atom functions have been used for solving the involved integrals and the energy shift obtained is

$$\frac{4}{9}\frac{(< ezF >)^2}{\Delta E}$$

ΔE being the original energy separation between 2s and 2po levels. The 2p (±1) levels are unaffected by I-V field. , but 2po level is shifted downwards. Our present interest is however only on 2s levels, over which the electrons get trapped before TLemission.

4. Experimental

Earlier preliminary studies in KCl system (Pandey et. al., 2017) report two broad peaks in the TL spectrum. The higher temperature peak was completely eliminated on heavy doping. In the present work, experiments are repeated for undoped KCl and the TL curves obtained are de-convoluted and further analysis done. The KCl used was analar grade of Fischer Scientific Co., and contained stray 0.001% divalent cations Ba, Ca and Pb as impurities. All the samples were irradiated with 20 mA, 30kV X-rays at room temperature for production of color centers in them, the irradiation being done for about 900 seconds. For all samples as above, TL measurements were made with a home- built TL apparatus with a heating rate of 30°C /minute.

The TL output was enhanced by IP21photomultiplier tube and resulting signal in terms of charge collected was plotted in a recorder as a function of temperature. The heating rate was the same as in our (Pandey et al., 2017) earlier work and that adopted by other workers (Furetta et al., 1999), while investigating TL of OH^- doped aqueous grown alkali halide crystal and gave fine contours for TL plot. Large exposure time of 900 seconds was necessary, so that anion vacancies associated with small number of bi-vacancy I-V pair hybrids due to low impurity concentration could also acquire electrons for TL response.

Our samples were prepared through slow evaporation of saturated aqueous solution of KCl at a fixed temperature of 10°C. The number of defect types was small, reflected by fewer numbers of deconvoluted peaks. It may be mentioned that the recent results (Ortiz et al., 2007) of NaCl containing divalent cations in melt grown crystals exhibited complex TL pattern. These authors do expect the role of many more defects needing further explanation.

The TL results for undoped KCl with stray impurities show two broad peaks as given in Fig. 2, there been no TL response above 440 K. The duo of TL curve peak was deconvoluted using the first order Glow Fit software (Puchalaska and Bilski, 2005). This led to five component peaks with FOM of 1.3%. Fig 2 shows composite duo TL curve and five component peaks together in the same figure.

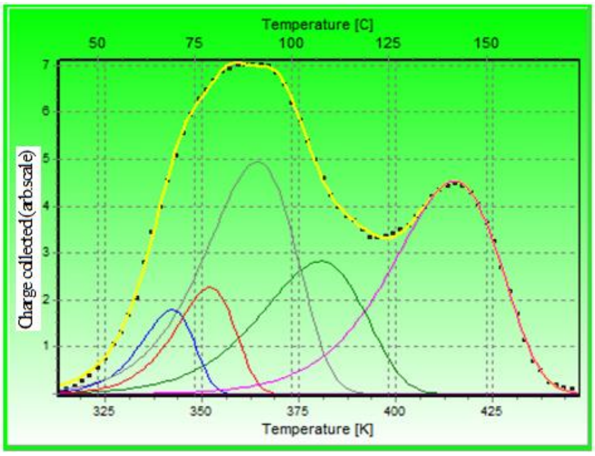

Figure 2. TL Glow curves for KCl systems with stray impurities and irradiated by X-rays. The de-convoluted peaks obtained by Glow Fit program are also seen.

5. Results

The temperatures of all the five component TL peaks and their trap depths are given in Table 1. Along with the TL data for melt grown KCl systems (Jain and Mehendru, 1965).

The peak at 415K is attributed to electrons trapped at an anion vacancy end of bi-vacancy. Such a peak was however, eliminated in samples with heavy doping of divalent cations (Pandey et. al.,

DOI:https//doi.org/10.22452/mjs.vol42no2.9

2017). The peaks involving linkage of anion vacancy with nnandnnn I-V pairs are also observed. We also attribute two other peaks to linkage of anion vacancy with OH^- ions, the corresponding details being given in the next Sec. 5.2. Such TL peaks cannot be observable in melt grown crystals.

Two TL peaks at 408 K and 463K are reported(Jain & Mehendru, 1965) in pure KCl. The corresponding trap depths are given in Table 1 for comparison.

5.1 Special features of trap assignments

(i) Bi-vacancy linked traps have a unique presence.
(ii) This bi-vacancy trap seems to be similar to the first stage F-center as discussed by earlier workers (Jain and Mahendru, 1965).
(iii) The OH^- linked defects are also found.

5.2 Role of hydroxyl ions in blocking the I-V pair formation

Ba^{2+},Sr^{2+} and Ca^{2+} ions have strong affinity for OH^- groups. Thus I-V pair anion vacancy link is probably eliminated for such ions through the formation of strong combination chain in the KCl lattice as:

anion vacancy--------H^+ --------O^{2-} -------AE^{2+}

AE^{2+} being an alkaline earth ionwhich perhaps prohibits linking of anion vacancy with AE^{2+} I-V pair due to its own affinity with hydroxyl group. In our work the trap depth observed for OH^- sites linked to anion vacancy are quite large. This probably supports earlier conclusions (Dharet. al., 1973) that OH^- ions act as deep traps and consequently have a quenching effect on TL peaks. Such peaks have much decreased intensity in TL spectra. Our work thus also supports the role of hydroxyl impurities in TL behavior of LiF (Stoebe et al., 1985).

6. Discussion

The depth of 2s level in a unique F-center (anion vacancy) with neighbourhood of six positive charges in KCl crystal is 0.277 eV. It however seems that, the absence of one cation from the immediate neighbourhood of anion vacancy as in Fig. 1(b) leads to the increase in the depth of 2s trap level in F-center to 1.05eV; of course if there be no I-V pairs around. This happens for bivacancy trap. The possible I-V pair link lifts the trap due to the effect of electric field as described in section 6.1.

If we compare the trap depths for F-center in KCl as per different workers, we find that 415K glow peak of present work is close to 408K glow peak in earlier work (Jain & Mehendru, 1965), the corresponding trap depths being quite close. In this work a peak was observed at 463K too. Its presence is probably due to the fact that their KCl crystals were grown through melt and are likely to include extra defects which lead to the creation of second stage F-centers with a trap depth of 1.15 eV.

6.1 Observed trap depth changes due to I-V field:

But for traps linked to HO^- (written knowingly) groups, depths of traps in our case are found in the range 1.05eV to 0.92eV. Figs. 1(c) and 1(d) show I-V pairs with nn and nnn arrangements respectively. The classical electric field expressions Fnn and F_{nnn} at the site of anion vacancies centers fornn and nnn I-V pair arrangements were derived by us based on point charge model as

$$F_{nn}= K\left((2\sqrt{5})/25 - 1\right) e/d^2$$
$$\text{and } F_{nnn}=K(-8/9)\ e/d^2$$

with $K= 1/(4\pi\varepsilon_0)$, 'e' as charge of electron and 'd' being the distance between K^+ and Cl^- ion, giving

$$F_{nn}^2 = 0.67K^2e^2/d^4$$
$$F_{nnn}^2 = 0.79K^2e^2/d^4$$

It may be realized here that for nnn disposition of cation vacancy, the anion vacancy is located at the end-on position of I-V dipoles as in Fig 1(d). But, for nn disposition, the situation is quite different as described in Fig 1(c).

However, as seen from Table 1, the effect of I-V field (as in Sec. 3), seems to support the trap depth changes from nn to nnn arrangement; the traps with nnn I- V pairs being shallower than those with nn pairs. The 0.96eV trap depth should thus correspond to nn configuration of I-V pair and 0.92eV trap depth to nnn configuration. The proposed configurations as in Table 1, seem to follow the above behavior due to stray ions as per quadratic Stark effect. It seems alkaline earth ions do not form I-V pairs due to the effect of hydroxyl ions and give TL peaks differently.

Table 1. Observed TL Peak Positions in KCl systems with depths of traps & their structures
(Heating rate being 30˚C/minute in present work)

Sr. No.	Status of Host	Peak Temperatures (⁰K) of sole or de-convoluted Peaks	Trap Depth (eV)	Anion Vacancy linked to
1.	Negligible I-V pairs	415	1.05	cation vacancy
2.	With I-V pairs of stray impurities	342 352 364 381	1.49 1.38 0.96 0.92	OH^- OH^- Pb^{2+}I-V pair(nn) Pb^{2+}I-V pair(nnn)
3.	With first type of F-centers	408	1.05*	
4.	With second type of F-centers	463	1.15*	

* (Jain & Mehendru , 1965)

7. Conclusions

The different configurations of TL traps obtained are as under Unique F-center (anion vacancy), which is probably not much stable.

(i) Bi-vacancy being the main trap configuration.
(ii) Two hybrid configurations of bi-vacancy and I-V pairs.
(iii) In aqueous grown crystals OH^- also seems to link anion vacancy with divalent cations and provide new trap.

A good dosimeter must have a large number of traps. In alkali halides the bi-vacancies are natural traps. The traps can be increased by doping alkali halides by divalent cations, when cation vacancy traps coupled to I-V pairs are created. For I-V pairs to exist, their aggregation should be avoided .This may be avoided by doping different kinds of ions at a time. The doping of trivalent ions could further be useful, as one such ion would hold two anion vacancies together. The present work thus also points towards developing good alkali halide dosimeters.

7. References

Ausin, V. & Rivas, J. A. (1972). Thermoluminescence and annealing of F-centres in KCl gamma irradiated at room temperature. *Journal of Physics C: Solid State Physics*, *5*(1), 82-96.

Benia, H. M., Myrach, P., Gonchar, A., Risse, T., Nilius, N., & Freund, H. J. (2010). Electron trapping in misfit dislocations of MgO thin films. *Physical Review B*, *81*(24), 241415.

Bos, A. J. J. (2006). Theory of thermoluminescence. *Radiation measurements*, *41*, 545-556.

Bushnell, J. C. (1964). *Electron-Nuclear Double Resonance Study of Z (1)-Centers in Potassium-Chloride* (Doctoral dissertation, University of Illinois at Urbana-Champaign).

Davydov, A. S. (1965). Quantum Mechanics, Pergamon, London.

Deshmukh, B. T., &Moharil, S. V. (1985). Thermoluminescence of alkali halides doped with alkaline earth impurities. *Bulletin of Materials Science*, *7*(5), 427-457.

Dhar, A., de Werd, L. A. and Stoebe, T.G., (1973**),** **"**Effects of Annhealing and coding processes onThermoluminiscence of LiF"Health Physics, 25, 427.

Furetta, C., Laudadio, M.T., Sanipoli, C., Scacco, A., Gomez-Ros, J. M. and Correcher, V. (1999), Thermoluminescence of OH^- doped rubidium halides, J. Phys. Chem. Solids 60, 957-963.

Gourary, B. S., & Adrian, F. J. (1957). Approximate wave functions for the F center and their application to the electron spin resonance problem. *Physical Review*, *105*(4), 1180.

Herman, Z. S., & Barnett, G. (1982). The Electronic Structure of F-Centres in Alkali Halide Crystals. *RevistaBrasileira de Fisica*, *12*(1), 73-91.

Hoya, J., Laborde, J. I., Richard, D.&Renteria, (2017)**,** M., Comp. Mat. Sc.,"Ab-initio study of F-centers in Alkali Halides", 138, 1-7.

Jain, S. C., &Mehendru, P. C. (1965). Evidence of Different Types of F Centers from Thermoluminescence Studies in X-Irradiated Alkali Halides. I. Highly Pure KCl Crystals. *Physical Review*, *140*(3A), A957.

Mehendru, P.C. and Radhakrishna, S. (1969), Thermoluminescence of pure and impurity doped KBr and NaCl crystals, J. Phys. C (Solid State), 2, 796-801.

Ortiz, A., Ramos – Bennal S., Negron – Mendoza A., Martinez, T. and Sanchez – Mejorada, G., Optical and thermoluminescence properties of a NaCl crystal doped with $Cd^{2+,}$ Mn^{2+} and exposed to gamma rays, J. RadioanalyticalNucl. Chem., 273, 573 – 575.

Puchalska, M and Bilski, P., **(**2005**)**. "TL glow curve analysis using glow fit, the new powerful tool for deconvolution" *Polish academy of sciences, Krakow, TCC Report No. 1968/d.*

Pandey, M., Mishra, A. K., Pant, N. &Pandey, S. D. (2017). Thermoluminescence of undoped and Mn2+ doped KCl. *ActaCiencia India*, *43P*, 255-260.

Pandey, Ruchi, Pandey, S D, Kumar, S. and Kumar, R., (2021**)**, Stability of bi-vacancy trap for TL emission in KCl, *Malaysian J. Sci., 40, 46-53*.

Sastry, S.B.S. &Sapru (1979), TL glow and emission studies on suprapureRbBr irradiated at room temperature, phys. stat. sol. 94, K149-154.

Srivastava, J. P. (2008). Solid State Physics. Prentice Hall, New Delhi, India.

Stoebe, T. G. and de Werd, L. A., (1985**),** *J.Appl. Phys.,* "Role of hydroxide impurity in the Thermoluminiscence behavior of LiF", 57, 2217.

Wosiński, T. (1989). Evidence for the electron traps at dislocations in GaAs crystals. *Journal of applied physics, 65(4), 1566-1570.*

DOI:https//doi.org/10.22452/mjs.vol42no2.9

MALAYSIAN JOURNAL OF SCIENCE
MJS
ISSN 1394-3065

Regular Issue

Malaysian Journal of Science 42 (2): 67-72 (June 2023)
https://mjs.um.edu.my

WHAT IS THE TRUE CARBON FRACTION VALUE OF MANGROVE BIOMASS?

Rahman[1a], Maryono[2b]*, Oktavia Nurmawaty Sigiro[3c]

Abstract: Carbon stock in mangrove stands is estimated through the biomass approach multiplied by the value of the mangrove carbon fraction which is generally set at 47% for all mangrove species to represent the actual carbon content value. This literature review analyzed relevant articles from Science Direct and Google Scholar using keywords: mangrove biomass, mangrove carbon stock, organic carbon of mangrove, carbon fraction of mangrove biomass, and chemical composition of mangrove biomass. The results showed that the carbon fraction value calculated based on organic carbon content was 46.4% which was lower than one calculated based on compounds making up mangrove biomass of 46.82% which consisted of 26.20% carbohydrates, 2.97% amino acids, 3.22% tannins, 3.38% lignins, 7.69% fatty acids, 3.17% triterpenoids, and 0.19% n-alkanes. The estimated homogeneous mangrove species carbon stock in a forest can be calculated based on the value of the carbon fraction of each mangrove species of 46.3% for B. gymnorrhiza, 45.9% for R. apiculata, and 47.1% for S. alba. Meanwhile, a carbon fraction value of 46.82% can be used for all true mangrove species to estimate the carbon stock in forests with heterogeneous mangrove species.

Keywords: *Carbohydrates, carbon fraction, carbon stock, mangrove, wood organic content.*

1. Introduction

Mangrove forests strongly contribute to the preventions of climate change for having the ability to absorb carbon dioxide (CO2) in the atmosphere through photosynthesis. The absorbed CO2 is then stored in the form of biomass in tree stands, fruit, roots, leaves, and other parts (Alongi 2008; Mandala et al., 2012; Alongi & Mukhopadhyay, 2015; Rahman et al., 2020b).

Mangroves also store huge amount of carbon in the substrate from the accumulation of residues from litters (Donato et al., 2012; Adame et al., 2015). Mangroves can absorb carbon three to four times better than other plants (Alongi 2008; Alongi 2014; Adame et al., 2015).

Carbon stock estimation in mangrove substrates can be made by analyzing the organic carbon content in sediments named total organic carbon (Komiyama et al., 2005). Meanwhile, carbon stock estimation in mangrove stands uses mangrove biomass value multiplied by mangrove carbon fraction value (Kauffman & Donato 2012).

Carbon fraction is the amount of carbon value of mangrove biomass. The mangrove carbon fraction values range between 46 – 51% (Kauffman & Donato 2012). Research on the carbon stocks estimation in mangrove stands have been carried out in different places in the world using destructive method in developing allometric equations to estimate the biomass in each mangrove species (Clough & Scott 1989; Fromard et al., 1998; Ong et al., 2004; Komiyama et al., 2005; Kusmana et al., 2018; Analuddin et al., 2020). After the biomass equation is obtained, the carbon stock value is calculated by multiplying the biomass value by the carbon fraction value. Most researchers used a mangrove carbon fraction value of 47% or 0.47 for all mangrove species despite the complete explanation of how the value was determined was unclear. In fact, mangrove biomass stock stored through photosynthesis is not only in the form of glucose ($C_6H_{12}O_6$), instead several chemical compounds such as carbohydrates, tannins, fats, proteins, and other chemical compounds are also found. Each chemical compound contains a certain percentage of carbon thereby carbon stock estimation should be based on the accumulation of carbon percentage from each component of the compound that makes up mangrove biomass. The accumulation can be measured using a mass ratio approach to weigh every element according to its number and atomic mass.

The use of the carbon fraction value in estimating the carbon stock of mangrove stands should be based on the actual value of the carbon content. The difference in the value of the carbon fraction of more than 0.1% will significantly affect the results because the mangrove carbon stock can reach 956 mg C ha-1. Thus, even 0.1% difference can either increase or decrease the estimated value by 0.956

Authors information:
[a]Marine Science Department, Fishery and Marine Science Faculty, Pattimura University, Maluku 97233, INDONESIA. E-mail: rahmanrajaali@gmail.com[1]
[b]Marine and Fisheries Agribusiness, Sambas State of Polytechnic, West Borneo 79400, INDONESIA. E-mail: maryonopoltesa@gmail.com[2]
[c]Food Agroindustry, Sambas State of Polytechnic West Borneo 79400, INDONESIA. E-mail: oktavia.nurmawati88@gmail.com[3]
*Corresponding Author: maryonopoltesa@gmail.com; maryono@poltesa.ac.id

Received: May 23, 2022
Accepted: July 25, 2022
Published: June 30, 2023

DOI:https//doi.org/10.22452/mjs.vol42no2.10

Mg C ha-1 or equivalent to 956 kg C ha -1. Regarding these concerns, the actual value of the carbon fraction needs to be calculated to obtain more accurate carbon stock estimation results of mangrove stands.

2. Methodology

2.1 Literature Search

Relevant scientific articles published up to 2022 were retrieved from Science Direct and Google Scholar based on several keywords: mangrove biomass, mangrove carbon stock, organic carbon of mangrove, carbon fraction of mangrove biomass, and chemical composition of mangrove biomass. The articles were then screened based on the titles and abstracts. Only articles with full-text available were included, and a number of articles with low relevancy were excluded. Research on mangrove biomass has been done from 1986 (Putz & Chan 1986) to 2022 (Hasidu et al., 2022). However, they did not provide overview of the actual carbon fraction value in estimating the mangrove biomass and carbon stock. There were 3 journal articles published between 2008 - 2011 that matched the inclusion criteria to provide relevant information regarding mangrove carbon fraction value.

3. Results and Discussions

3.1 Carbon Fraction Based on Organic Carbon Content

Carbon fraction value is expressed in a percentage calculated by comparing the mass of organic carbon to the total biomass value. The carbon fraction is also known as wood carbon content (Kauffman et al., 2011). The value of carbon fraction in each mangrove species differs due to different wood density value of each mangrove species. Kauffman et al., (2011) reported that the carbon fractions for *B. gymnorrhiza, R. apiculata*, and *S. alba* species were 46.3%, 45.9%, and 47.1%, respectively. Meanwhile, the average value of carbon fraction for all species has been set at 46.4% (Table 1). The carbon fraction is the fraction value estimated based on the total organic carbon content in mangrove biomass.

The values of the carbon fraction, especially in *B. gymnorrhiza* and *R. apiculata* species, are much lower than the 47% value that is often used by researchers in estimating mangrove carbon stocks. The value of 47% is closer to the species S. alba (47.1) with 0.1% difference that is known to affect the true estimated carbon stock value of mangrove stands.

Mangrove forests generally consist of variety mangrove species that form zoning based on the character of the substrate or salinity (Rahman et al., 2017; Rahman et al., 2020b). Therefore, Kauffman et al., (2011) stated that the estimated mangrove carbon stock should be calculated based on the carbon fraction value of every species or based on the average value of 46.4% of all mangrove species. The value of 46.4% is much lower than the value of the carbon fraction which is often used in estimating the carbon stock of mangrove stands of 47%. Based on these differences, the estimated results of the mangrove carbon stock experienced an excess of 0.6% or equivalent to 5,736 Mg C ha^{-1}.

Although Kauffman et al., (2011) have reported the value of the carbon fraction in several mangrove species, information on the composition of compounds that make up mangrove biomass containing the C element remain unavailable, thereby the value cannot describe the actual carbon fraction value. This value was calculated based on the weight of organic carbon content in mangrove biomass without decomposing the components of the constituent compounds of mangrove biomass.

Table 1. The carbon fraction values of different mangrove species

Species	Carbon Fraction (%)
Bruguiera gymnorrhiza	46.3
Rhizophora apiculata	45.9
Sonneratia alba	47.1
Average of all species	46.4

Source: Kauffman et. al., (2011)

DOI:https//doi.org/10.22452/mjs.vol42no2.10

3.2 Carbon Fraction Based on Compounds Composing Mangrove Biomass

The mangrove biomass stored in mangrove stands results from the photosynthesis process that occurs in the leaves and pneumatophore organs at the roots and the absorption of salts by root fibers through the xylem and phloem. Kristensen et al., (2008) found that mangrove biomass was composed of 65.5% carbohydrates, 9% protein, 6% tannins, 5.1% lignin, 10.68% fatty acids, 3.5% triterpenoids, and 0.22% n-alkane (Figure 1).

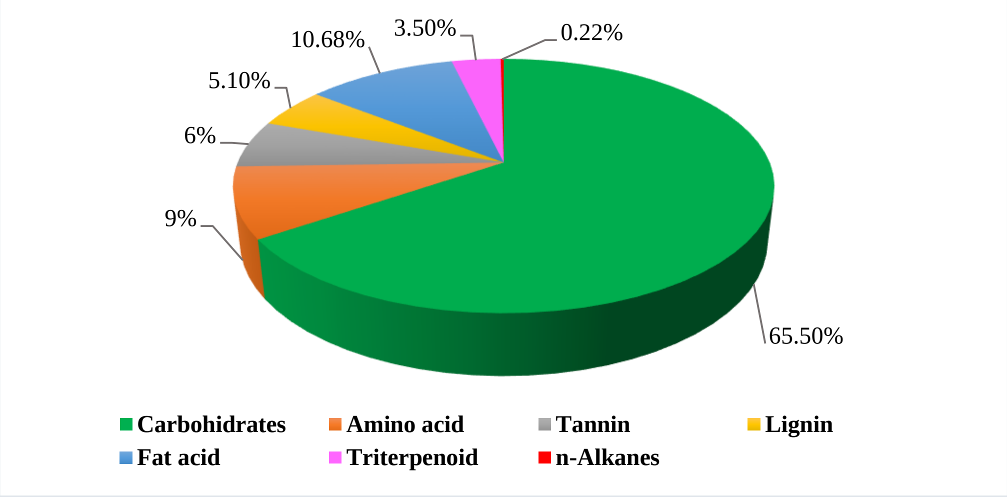

Figure 1. Chemical components of mangrove biomass

The components of biomass are relatively similar to *Bruguiera*, *Rhizophora*, and *Sonneratia* species, with slight difference only in the n-alkane of 26 – 31 n-alkanes (C_nH_{2n+2}, with n = 26 – 31). However, the percentage of n-alkanes in mangrove biomass is only around 0.22% thereby this different n-alkanes structure can be ignored.

3.2.1 Carbohydrate

Carbohydrates are the largest component of mangrove biomass found in mangrove tree stands, especially *Bruguiera, Rhizophora,* and *Sonneratia* species with 65.5% (Kristensen et al. 2008). Carbohydrates are compounds composed of glucose ($C_6H_{12}O_6$) and have the basic molecular formula ($C_6H_{12}O_6$)n. Based on the chemical formula, the molecular mass of the carbohydrate compound is 180 g mole^{-1} (Mr = (180)n g mole^{-1}). From a total of 180 g mole^{-1}, there are 72 g mole^{-1}, C atoms, or equivalent to 40% obtained from 6 C atoms with a relative atomic mass (Ar) of 12 g mole$^{-1.}$

Mangrove carbon fraction from carbohydrate compounds is calculated by multiplying the percentage of carbohydrates in mangrove biomass (65.5%) by the total mass of carbon in carbohydrates (40%), resulting in 26.20% (Table 2).

3.2.2 Amino Acid

The amino acid content in mangrove biomass is 9% which is mostly found in mangrove leaves, especially in *Bruguiera, Rhizophora,* and *Sonneratia* (Hernes et al., 2001). Amino acids are the smallest structures of protein compounds with the basic molecular formula of ($C_2H_3O_2N$)n. Based on the chemical formula, the molecular mass of the amino acid compound is 73 g mole^{-1} (Mr = (73)n g mole^{-1}). From a total of 73 g mole^{-1}, there are 24 g mole^{-1} C atoms or equivalent to 33% obtained from 2 C atoms with a relative atomic mass (Ar) of 12 g mole^{-1}.

Mangrove carbon fraction of amino acid compounds was calculated by multiplying the percentage of amino acids in mangrove biomass (9%) by the total mass of carbon in amino acids (33%), resulting in carbon contribution of amino acids in mangrove biomass of 2.97% (Table 2).

3.2.3 Tannin

The tannin content in the mangrove biomass is 6%. These levels are mostly found in mangrove leaves, especially from the *Bruguiera* species (Hernes et al., 2001). Tannins are compounds composed of polysaccharides with the molecular formula ($C_{38}H_{26}O_{23}$)n. The molecular mass of the tannin compound is 850 g mole^{-1} (Mr = (850)n g mole^{-1}). Out of 850 g mole^{-1}, there are 456 g mole^{-1} C atoms or equivalent to 53.65% obtained from 38 C atoms with a relative atomic mass (Ar) of 12 g mole^{-1}.

The mangrove carbon fraction from tannin compounds was calculated by multiplying the percentage of tannins in mangrove biomass (6%) by the total mass of carbon in tannins (53.65%) resulting in total carbon contribution of tannins in mangrove biomass of 3.22% (Table 2).

3.2.4 Lignin

Mangrove biomass contains 5.1% lignin found in the leaves and stands of mangrove trees, especially from true mangrove species such as Rhizophora, Avicennia, and Sonneratia (Marchand et al., 2005). Lignin is a co-polymer compound with free nitrogen that contains variety of phenylprophenyl alcohols. The molecular formula of lignin is $C_9H_{10}O_2(OCH_3)$n. The molecular mass of the lignin compound is 150 + (31)n g mole^{-1} (Mr = 150(31)n g mole^{-1}). From a total of 150 + (31)n g mole^{-1} there are 108 + (12)n g mole^{-1} C atoms or equivalent to 66.3% obtained from 9 C atoms + n C atoms with relative atomic masses (Ar) of 12 g mole^{-1}.

The mangrove carbon fraction from lignin compounds was calculated by multiplying the percentage of lignin in mangrove biomass (5.1%) by the total mass of carbon in lignin

(66.3%), resulting in total carbon contribution of lignin in mangrove biomass of 3.38% (Table 2).

3.2.5 Fatty Acids

Fatty acids are the second-largest compound found in mangrove biomass that reached 10.68% and are mostly found in mangrove leaves and fruit, especially from true mangrove species such as Rhizophora, Avicennia, and Sonneratia. Fatty acids have the molecular formula of $C_{11}H_{23}COOH$ with molecular mass of 200 g mole^{-1} (Mr = 200 g mole^{-1}). From a total of 200 g mole^{-1}, there are 144 g mole^{-1} C atoms, or the equivalent of 72% obtained from 10 C atoms with a relative atomic mass (Ar) of 12 g mole^{-1}.

Mangrove carbon fraction from fatty acid compounds is calculated by multiplying the percentage of fatty acids in mangrove biomass (10.68%) by the total mass of carbon in fatty acids (72%), resulting in a total carbon contribution of fatty acids in mangrove biomass of 7.69% (Table 2).

3.2.6 Triterpenoid

Triterpenoids are hydrocarbons composed of C and H atoms that reached 3.5% in mangrove biomass (Kristensen et al. 2008). These compounds are mostly found in mangrove leaves, especially from true mangrove species such as Rhizophora, Avicennia, and Sonneratia. Triterpenoids have the molecular formula of $C_{38}H_{48}$ with 504 g mole^{-1} molecular mass (Mr = 504 g mole^{-1}). There are approximately 456 g mole^{-1} C atoms or the equivalent of 90.47% obtained from 38 C atoms with a relative atomic mass (Ar) of 12 g mole^{-1}.

The mangrove carbon fraction of triterpenoid compounds was calculated by multiplying the percentage of triterpenoids in mangrove biomass (3.5%) by the total mass of carbon in fatty acid (90.47%), resulting in total carbon contribution of 3.17% in mangrove biomass (Table 2).

3.2.7 n-Alkanes

n-Alkanes are hydrocarbons composed of C and H atoms which carbon chain length ranges between 22 and 35. In general, the length of the carbon chain of n-alkanes found in mangroves is 31 carbon chains and n-alkanes content in mangrove biomass is 0.22%. The compound has the least proportion in mangrove biomass which is mostly found in mangrove leaves, especially from true mangrove species such as *Rhizophora, Avicennia,* and *Sonneratia* (Versteegh et al., 2004; Mead et al., 2005). n-Alkanes have the molecular formula of CnH2n+2 and molecular mass with chain length C=31 is 436 g mole^{-1} (Mr = 436 g mole^{-1}). There are 372 g mole^{-1} C atoms or equivalent to 85% obtained from 31 C atoms with a relative atomic mass (Ar) of 12 g mole^{-1}.

The mangrove carbon fraction of the n-alkanes compound is calculated by multiplying the percentage of n-alkanes in mangrove biomass (0.22%) by the total mass of carbon in n-alkanes (85%), resulting in 0.19 total carbon contribution of n-alkanes in mangrove biomass (Table 2).

The total value of the mangrove carbon fraction is 46.82% consisting of carbohydrates (26.20%), amino acids (2.97%), tannins (3.22%), lignins (3.38%), fatty acids (7.69%), triterpenoids (3.17 %), and n-alkanes (0.19%) (Table 2). The value of the carbon fraction can be used in evaluating the carbon stock of mangroves in heterogeneous forests. The value of the carbon fraction gained using organic carbon content approach is 46.4% (Kauffman et al., 2011) that is approximately 0.42% lower than the value of the carbon fraction calculated based on the components that make up mangrove biomass of 46.82%. The estimated mangrove carbon stocks from palm species such as *N. Fruticans* is 39% can be used (Rahman et al., 2017; Rahman et al., 2020a).

Table 2. The value of carbon fraction in mangrove biomass

Compounds*	% compounds in litter*	Basic molecular formula	Mr of compound	Ar of C	% C in compound	% C in litter
Carbohydrate	65.5	$(C_6H_{12}O_6)n$	(180)n	(72)n	40	26.20
Amino acid	9	$(C_2H_3O_2N)n$	(73)n	(24)n	33	2.97
Tannin	6	$(C_{38}H_{26}O_{23})n$	(850)n	(456)n	53.65	3.22
Lignin	5.1	$C_9H_{10}O_2(OCH_3)n$	150+(31)n	108(12)n	66.3	3.38
Fatty acid	10.68	$C_{11}H_{23}COOH$	200	144	72	7.69
Triterpenoid	3.5	$C_{38}H_{48}$	504	456	90.47	3.17
n-Alkane	0.22	C_nH_{2n+2}	$_{n=31}$, 436	372	85	0.19
Total						46. 82%

Notes: *Sources: Hernes et al., (2001); Versteegh et al., (2004); Marchand et al., (2005); Mead et al., (2005); Kristensen et al. (2008); Ar = relative mass of atom (C = 12, O = 16, H = 1, N = 14), Mr = relative mass of compounds

DOI:https//doi.org/10.22452/mjs.vol42no2.10

3.3 Chemical Elements of Mangrove Biomass

The chemical elements that makeup mangrove biomass consist of carbon (C), oxygen (O), hydrogen (H), and nitrogen (N). Elements C, O, and H obtained through photosynthesis – a process where CO_2 from the atmosphere is absorbed and stored in the mangrove biomass as carbohydrates, amino acids, tannins, lignin, fatty acids, triterpenoids, and n-alkanes. Meanwhile, the element N is calculated from the absorption of mineral salts by the xylem and phloem tissues in the roots. The N content is stored in the mangrove biomass as amino acids or proteins.

Based on the percentage of compounds, relative molecular mass, and relative atomic mass of compounds and elements that make up mangrove biomass, the value of the composition of C elements is 46.82%, O elements is 44.54%, H elements is 6.92%, and N elements is 1,72% (Figure 2). The composition of these constituent elements further emphasizes that the actual value of the carbon fraction of mangrove biomass is 46.82%.

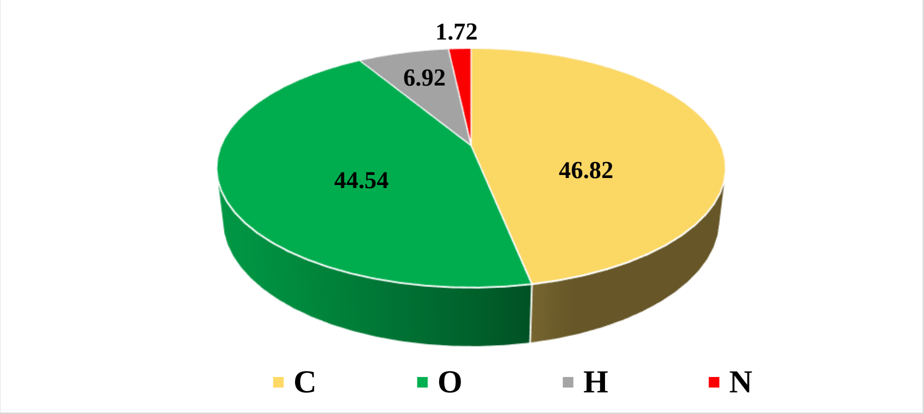

Figure 2. Composition of chemical elements that make up mangrove biomass

4. Conclusions

The value of the carbon fraction determined based on the organic carbon content is 46.4%, or about 0.42% lower than the value of the carbon fraction calculated based on the components of the compounds that make up mangrove biomass of 46.82%, which consists of carbohydrates (26.20%), amino acids (2.97%), tannin (3.22%), lignin (3.38%), fatty acid (7.69%), triterpenoids (3.17%), and n-alkanes (0.19%). The estimation of the carbon stock of mangrove trees in forests with homogeneous species can use the value of the carbon fraction of 46.3% for B. gymnorrhiza, 45.9% for R. apiculata, and 47.1% for S. alba. Meanwhile, to estimate the carbon stock of mangrove trees in forests with heterogeneous mangrove species, a carbon fraction value of 46.82% can be used for all true mangrove species found in the forest. Whereas, the carbon fraction value of 39% applies in the estimation of mangrove carbon stock from palm species such as N. fruticans.

5. References

Adame, M.F., Santini, N.S., Tovilla, C., Lule, A.V., Castro. L., Guevara, M. 2015. Carbon stock and soil sequestration rates of tropical riverine wetlands. Biogeosci. **12**(12): 3805−3818. doi: 10.5194/bg-12-3805-2015.

Alongi, D.M. 2008. Mangrove forests: resilience, protection from tsunamis, and responses to global climate change. Estuar. Coast. Shelf Sci. **76**(1): 1−13. doi: 10.1016/j.ecss.2007.08.024.

Alongi, D.M. 2014. Carbon cycling and storage in mangrove forests. Annual. Rev. Mar. Sci. **6**: 195−219. doi: 10.1146/annurev-marine-010213-135020.

Alongi, D.M., and Mukhopadhyay, S.K. 2015. Contribution of mangrove to coastal carbon cycling in low latitude seas. Agricul. For. Meteorol. **213**: 266−272. doi: 10.1016/j.agrformet.2014.10.005.

Analuddin, K., Kadidae, L., Haya, L.M.Y., Septiana, A., Sahidin, I., et al. 2020. Aboveground biomass, productivity, and carbon sequestration in *Rhizophora stylosa* mangrove forest of Southeast Sulawesi, Indonesia. Biodiversitas. **21**(3): 1316−1325. doi: 10.13057/biodiv/d210407.

Clough, B.F., and Scott, K. 1989. Allometric relationships for estimating above-ground biomass in six mangrove species. For. Ecol. Manage. **27**: 117−127. doi: 10.1016/0378-1127(89)90034-0.

Donato, D.C., Kauffman, J.B., Mackenzie, R.A., Ainsworth, A., Pfleeger, A.Z. 2012. Whole-island carbon stock in tropical pacific: Implications for mangrove conservation and upland restoration. J. Environ. Manage. **97**:89−96. doi: 10.1016/j.jenvman.2011.12.004.

Fromard, F., Puig, H., Mougin, E., Betoulle, J.L., Cadamuro, L. 1998. Structure, above-ground biomass and dynamics of mangrove ecosystems: new data from French Guiana. Oecologia. **23**(1/2): 39−53.

Hasidu, L.O.A.F., Prasetya, A., Maharani, Syaiful, M., Analuddin, K. 2022. Allometric model, aboveground biomass, and carbon sequestration of natural regeneration of *Avicennia lanata* (Ridley) at the in-active pond of Muna Regency, Southeast Sulawesi. Hayati J. of Scie. **29**(3): 399–408. doi: 10.4308/hjb.29.3.399-408.

Hernes, P.J., Benner, R., Cowie, G.L., Goni, M.A., Bergamaschi, B.A., Hedges, J.I. 2001. Tannin diagenesis in mangrove leaves from a tropical estuary: A novel molecular approach. Geochim. Cosmochim. Acta. **65**(18): 3109–3122. doi: 10.1016/S0016-7037(01)00641-X.

Kauffman, J.B., Heider, C., Cole, T., Dwire, K.A., Donato, D.C. 2011 Ecosystem C pools of Micronesian mangrove forests. Wetlands. **31**(2):343–352. doi: 10.1007/s13157-011-0148-9.

Kauffman, J.B., and Donato, D.C. 2012. Protocols for the measurement, monitoring, and reporting of structure, biomass, and carbon stocks in mangrove forests. Working paper. CIFOR. 50p.

Komiyama, A., Poungparn, S., Kato, S. 2005. Common allometric equation for estimating the tree weight of mangroves. J. Trop. Ecol. **21**(4): 471–477. doi: 10.1017/S0266467405002476.

Kristensen, E., Bouillon, S., Dittmar, T., Marchand, C. 2008. Organic carbon dynamics in mangrove ecosystems: A review. Aqua. Bot. **89**(2): 201–219. doi: 10.1016/j.aquabot.2007.12.005.

Kusmana, C., Hidayat, T., Tiryana, T., Rusdiana, O., Istomo. 2018. Allometric models for above – and below-ground biomass of *Sonneratia* spp. Glob. Ecol. Conserv. **15**:e00417. doi: 10.1016/j.gecco.2018.e00417.

Mandala, S., Rayb, S., Ghosh, P.B. 2012. Comparative study of mangrove litter nitrogen cycling to the adjacent estuary through modeling in pristine and reclaimed islands of Sundarban mangrove ecosystem, India. Environ. Sci. **13**: 340–362. doi: 10.1016/j.proenv.2012.01.033.

Marchand, C., Disnar, J.-R., Lallier-Verges, E., Lottier, N. 2005. Early diagenesis of carbohydrates and lignin in mangrove sediments subject to variable redox conditions (French Guiana). Geochim. Cosmochim. Acta. **69**(1): 131–142. doi: 10.1016/j.gca.2004.06.016.

Mead, R., Xu, Y., Chong, J., Jaffe´, R. 2005. Sediment and soil organic matter source assessment as revealed by the molecular distribution and carbon composition of n-alkanes. Org. Geochem. **36**(3): 363–370. doi: 10.1016/j.orggeochem.2004.10.003.

Putz, F.E., and Chan, H.T. 1986. Tree growth, dynamics, and productivity in a mature mangrove forest in Malaysia. Forest Ecology and Management. **17**(2-3): 211–230. doi: 10.1016/0378-1127(86)90113-1.

Rahman., Efendi, H., Rusmana, I. 2017. Stock estimation and carbon absorption of mangrove in Tallo River, Makassar. J. For. Sci. **11**(1): 19–28. doi: 10.22146/jik.24867.

Rahman, Wardiatno, Y., Yulianda, F., Rusmana, I., Ali, M. 2020a. Metode pengukuran dan model pendugaan biomassa *Nypa fruticans* di Sungai Tallo, Makassar – Indonesia. *Jurnal Grouper*. **11**(1): 25–30. doi: 10.30736/grouper.v11i1.65.

Rahman, Wardiatno, Y., Yulianda, F., Rusmana, I., Bengen, D.G. 2020b. Metode dan Analisis Studi Ekosistem Mangrove. IPB Press. Bogor. 124pp.

Versteegh, G.J.M., Schefuß, E., Dupont, L., Marret, F., Sinninghe-Damst'e, J.S., Jansen, J.H.F. 2004. Taraxerol and Rhizophora pollen as proxies for tracking pas mangrove ecosystem. Geochim. Cosmochim. Acta. **68**(3): 411–422. doi: 10.1016/S0016-7037(03)00456-3.